INTENSE HEAVY NEGATIVE-ION BEAM PRODUCTION

AND

NEGATIVE ION BEAM DEPOSITION

YASUHIKO TAKEIRI

1987

INTENSE HEAVY NEGATIVE-ION BEAM PRODUCTION

AND

NEGATIVE ION BEAM DEPOSITION

YASUHIKO TAKEIRI

1987

Recent progress of "Ion Engineering" has been closely correlated with development of various types of ion sources. A large number of ion sources have been developed extensively and intensively --- a high-brightness ion source, a multiply-charged ion source and a negative ion source for an accelerator, a several to several tens mA-metal ion source for an ion implanter and an ion-beam modification, a fine-focused ion source for a submicron process of material, a reliable and compact ion source for a surface analysis, and a high current ion source for a neutral beam injection heating system in a nuclear fusion device. Ion source development, however, has depended largely on requirement of producing a specific ion beam to be utilized in each individual field. Thus, it is important that ion source development should enhance the intended application field during the ion engineering. In this thesis, the author develops an intense heavy negative-ion source and applies the negative ion beam to a material science field, from the point of view of the ion source development leading to creation of a new application field in the ion engineering.

Negative ion sources have been developed intensively for a Tandem accelerator and a neutral beam injection heating system in a nuclear fusion device. In these field, however, only the kinetic energy of the negative ion beams is utilized. Considering that the basic concept of the ion engineering is utilization of the kinetic energy and the ionic charge of the

ion, the new application field utilizing effect of the ionic charge of the negative ion should be created by developing an intense heavy negative-ion source.

In this research, in order to apply the heavy negative-ion beam to the material science, the intense heavy negative-ion source and the negative-ion-beam deposition system are newly developed and, then, a carbon film is formed by negative ion beam deposition. The emphasis is placed on the operational characteristics and analyses of the developed ion sources and deposition system. The deposited film property is also investigated in detail with regard to the deposition energy. The author hopes that with this research ion source development will lead to the creation of new application fields, as well as contribute to the further progress of ion engineering.

May 1987

Yasuhiko TAKEIRI

ACKNOWLEDGMENT

CONTENTS

Chapter 3   NEUTRAL- AND IONIZED-ALKALINE-METAL BOMBARDMENT-TYPE HEAVY NEGATIVE-ION SOURCE (NIABNIS)

Chapter 4   MASS-SEPARATED NEGATIVE-ION-BEAM DEPOSITION SYSTEM

INTRODUCTION

1.1 Research Objectives

A negative ion beam has different properties from a positive ion beam[1]. Its unique physical structure and chemical activities have been utilized in Tandem accelerators[1-4], controlled thermonuclear research programs[5,6], as analytical tools for surface research[7,8], and so on. In these application fields the negative ion beam plays a dominant role in itself, that is, its inherent properties are essential to the operational principles of the devices employed. However, applications of the negative ion beam are still restricted to several fields, mainly because yields of the negative ion beam are not enough to utilize the negative ion beam in various fields where the positive ion beam is widely available. Therefore, it is required that an intense negative ion source should be developed and that new application fields utilizing the negative ion beam should be investigated.

It is a challenging goal to apply the negative ion beam to material science where the positive ion beam already plays an important role[9], and also to investigate distinctive properties of the negative ion beam in material science. There are two attractive points in utilizing the negative ion beam in the

material science field. First, although this is a practical aspect, the negative ion beam offers greater advantage for particle transportation and utilization of kinetic energy than does the positive ion beam if the negative ion yields are more than positive ion yields. For some species this situation is prospective because production mechanisms of the negative ions are quite different from those of the positive ions and high current negative ion sources are now intensively being developed. Second, inherent properties of the negative ion beam are expected to be effective for film deposition, synthesis of compound material, or material modification. Charge state and chemical activity of the negative ions, which are quite different from those of the positive ions, have a significant influence on the interaction with solids, especially in the low beam energy range.

However, no application of the negative ion beam to material science field has been reported, because intense heavy negative-ion sources, which can produce a large amount of negative ion beam of especially III, IV, and V elements, has not yet been developed. Thus, development of a high current heavy negative-ion source is necessary to apply the negative ion beam to the material science field.

Research objectives in this thesis are summarized as follows:

(a) Development of an intense heavy negative-ion source where the amount of negative ion obtained is enough to apply the negative ion beam to material science.

(b) Thin film formation by mass-separated negative-ion-beam deposition to demonstrate the application of a negative ion

2

beam to material science.

1.2 Design Concept of Intense Heavy Negative-Ion Source

Development of negative ion sources was promoted by the
Tandem accelerator concept suggested by Bennett in 1937[1]. For
the practical realization of this concept, a powerful negative-
ion source was developed by Weinman and Cameron in 1956 which
provided 25 μA of H$^-$ ions[10]. Since then, various types of
negative ion sources have been developed as an injector of the
Tandem accelerator. On the other hand, because of higher
neutralization efficiency of a hydrogen negative-ion beam in high
energy region than that of a hydrogen positive-ion beam, high
current H$^-$ (or D$^-$) ion sources have been intensively developed
for neutral beam injection into plasma fusion research devices
since the 1970s[5,6].

Various types of negative ion sources are classified in
Table 1.1, and several reviews of the negative ion sources are
presented in refs. 11) and 12) for the heavy negative-ion sources
and in refs. 13) and 14) for the hydrogen (or deuterium)
negative-ion sources.

A sputter-type heavy negative-ion source in the secondary
negative-ion emission group is prospective for the development of
an intense heavy negative-ion source, because almost all species
whose electron affinities are positive are obtained as negative
ions and the secondary negative-ion emission process has the
possibility of highly efficient negative ion production. The
sputter-type heavy negative-ion source was originally developed

Table 1.1   Classification of representative

negative ion sources.

Negative ion extraction from discharged plasma

    •PIG and its modifications
        PIG type
        Calutron
        SPIGS (sputter PIG source)

    •Duoplasmatron and its modifications
        Duoplasmatron (off axis)
        Duodehcatron
        Triplasmatron

    •Volume production
        Multi-cusp type

Secondary negative-ion emission

    •Reflection type
        HDD (hollow discharge duoplasmatron)
        Magnetron (or surface plasma source)
        Penning type
        Multi-cusp type
        Hollow cathode type

    •Sputter type
        ANIS (Aarhus negative ion source)
        UNIS (universal negative ion source)
        Versatile high intensity negative ion source
        NIABNIS (neutral- and ionized-alkaline-metal
                    bombardment-type negative ion source)

by Mueller and Hortig in 1969[15]. This fruitful result
stimulated the intense heavy negative-ion source development, and
two potential negative ion sources, UNIS (universal negative ion
source)[16] and ANIS (Aarhus negative ion source)[17] were
developed which produced as much as several tens μA of negative
ion beams for some species. In the sputter negative-ion source,
in order to increase the negative ion yields, it is required that
the current of incident primary positive ions which sputter the
target material to be negatively ionized should be large and that
the work function of the target surface should be kept as low as
possible[11,12]. The work function of the target surface is
reduced by covering the surface with a half to mono-layer of
alkaline metal atoms[18,19], the condition of which can be
maintained by additional supply of neutral alkaline atoms to the
target surface and/or by temperature control of the target
surface. Neither the UNIS nor the ANIS always satisfies these
requirements. In this research a sputter-type intense heavy
negative-ion source was developed which satisfied simultaneously
the above-mentioned requirements. Design concept of this intense
heavy negative-ion source, which is called neutral- and ionized-
alkaline-metal bombardment-type heavy negative-ion source
(NIABNIS), is summarized as follows:
(a) The NIABNIS consists of a primary alkaline-metal ion source,
    sputtering target region (negative ion production region), and
    negative ion extraction region.
(b) The primary alkaline-metal ion source is used for supplying
    both ionized alkaline particles with a high energy for the
    sputtering of the target material and neutral alkaline

particles with a thermal energy for the coverage of the target
surface which results in a low work function of the target
surface.

(c) The temperature of the sputtering target is controllable so
as to keep the low work function of the target surface.

(d) The negative ions are efficiently extracted with charge
neutralization by the primary positive ions.

(e) The construction of the NIABNIS is simple and compact.

A high current and simply designed alkaline-metal ion source
which can also provide the neutral alkaline particles should be
developed in order to realize the above-mentioned concept of the
intense heavy negative-ion source, NIABNIS.

1.3 Application of Negative Ion Beam to Film Formation

In the past several years, extensive studies on an ion-based
technique for film formation have been carried out[20]. The
principle behind this technique is that the principal
characteristics of thin films, such as electrical, optical,
mechanical, chemical, and crystallographic properties, can be
controlled by the kinetic energy and the ionic charge of an
accelerated ion beam, rather than by the thermal energy of a
substrate. By the use of conventional ion-beam deposition
systems, in which partially and positively ionized atoms,
molecules, or clusters without mass separation are utilized, some
qualitative mechanisms of the ion-based film formation have been
understood[21-24]. To understand these mechanisms quantitatively,
accurate control of the kinetic energy and the charge state is

required. The effects of the kinetic energy should be investigated in detail by utilizing mass-separated ion beams with a very low mono-energy of several eV to several hundreds eV, and the influence of the charge state can be clarified by comparing negative-ion-beam-deposited films with positive-ion-beam-deposited films.

The negative-ion-beam deposition system can also be used as a new advanced technique for film formation. A positive ion is in the highly excited energy state; the energy state is higher by its ionization energy than that of a neutral particle, which is in the ground state. A negative ion is in the lowest energy state; the energy state is lower by its electron affinity than that of a neutral particle. Therefore, in the beam-solid surface interactions some differences exist between the negative- and positive-ion beams, especially in the low kinetic energy range. They will also appear as differences in deposited film properties.

A few examples of the film formation by the mass-separated positive-ion-beam deposition were reported: Ag^+ ion deposition with 25 to 50 eV on Si substrate[25], Pb^+ or Mn^+ with 24 to 200 eV on C or NaCl[26,27], Ge^+ or Si^+ with 100 to 300 eV on Ge or Si[28], and C^+ with 300 and 600 eV on Si[29]. These films show interesting features such as low temperature epitaxial growth, and have a dependence of film properties on the kinetic energy of the deposited ions.

The mass-separated ion-beam deposition system requires an ion-beam deceleration electrode arrangement, because the mass-separated ion beam has a high energy of several tens keV. For

7

the film formation by the ion beam deposition the ion beam must be decelerated to an energy below the critical energy where the self-sputtering ratio is unity. Table 1.2 shows the critical energies for some species for the film formation by ion beam deposition[30]. On the other hand, the energy spread of the decelerated ion beam, which ranges from several eV to several tens eV, must be considered in the extreme low energy range. The key issues in designing the ion-beam deceleration electrode system are summarized as follows:

(a) Convergent lens effect is required to suppress the divergence of the low-energy ion beam due to divergent lens effect in the deceleration gap and the space-charge repulsion force.

(b) The oppositely charged particles in the decelerated ion beam should be excluded, because they are accelerated in the deceleration electric field and are incident on the substrate.

(c) The high-energy neutral particles should be separated so as not to bombard the growing film.

(d) The deposition chamber should be kept in a quite high vacuum during deposition so that the residual gas atoms scarcely influence the growing film.

(e) It is desirable that the incident ion beam current on the substrate be monitored by suppressing the secondary electrons emitted from the substrate due to the low-energy ion bombardment.

J.H.Freeman et al. originally investigated the positive-ion-beam deceleration system in detail[31], and, since then, several positive-ion-beam deceleration systems have been equipped based on the Freeman's system. The negative-ion-beam deceleration

Table 1.2 Critical energy for film formation in
ion beam deposition[30].

Ion species	Critical energy (keV)
Fe^+	1.5 – 2.0
Co^+	1.0 – 1.5
Ni^+	0.8 – 1.0
Cu^+	0.3 – 0.4
Zn^+	0.3 – 0.4
Sn^+	0.45 – 0.5

system can be designed more simply than the positive-ion-beam deceleration system, because of a negligible amount of the oppositely charged particles, that is, positive ions. As a result, the loss of the negative ions during deceleration is less due to the simply designed electrode arrangement for deceleration. Moreover, since the negative ion source is a sputter source, no gas flows into the deposition chamber. Thus, the deposition chamber is always kept in a quite high vacuum.

The mass-separated negative-ion-beam deposition system, which includes the NIABNIS and the newly designed negative-ion-beam deceleration electrode system, was originally developed by the author and his co-workers. In this research, by use of this system carbon film was successfully deposited, and characteristic features of the deposited carbon film were investigated in detail.

1.4 Research Program

As described in the previous sections, this research is divided into two main parts; one is the development of the intense heavy negative-ion source and the other is the film formation by negative-ion-beam deposition. To achieve these purposes, first of all, an axial magnetic field extraction-type microwave ion source with a permanent magnet was developed which is used as a primary alkaline metal ion source of the intense heavy negative-ion source. This compact-designed microwave ion source is operated at high efficiency and produces a high-density ion beam. In chapter 2, construction and operational

```
┌─────────────────────────────┐
│ Development of microwave ion │
│   source (primary alkaline  │ ◄──┐        Chapter 2
│ metal ion source of NIABNIS)│    │
└─────────────────────────────┘    │
              │          ┌──────────────────────┐
              │          │  Concept of NIABNIS  │  ┐
              │          └──────────────────────┘  │
              ▼               │                     ├ Chapter 3
┌─────────────────────────┐   ▼                     │
│ Development of intense heavy│                      │
│ negative-ion source (NIABNIS)│                    ┘
└─────────────────────────┘
              │        ┌─────────────────────────┐
              │        │   Design of ion beam    │ ┐
              │        │ deceleration electrode  │ │
              │        │        system           │ │
              │        └─────────────────────────┘ ├ Chapter 4
              ▼               ▼                     │
┌─────────────────────────────────────────┐        │
│ Development of mass-separated negative-  │        ┘
│     ion-beam deposition system           │
└─────────────────────────────────────────┘
              │
              ▼
┌─────────────────────────────────────────┐
│ Formation of carbon film by negative-    │      Chapter 5
│     carbon-ion-beam deposition           │
└─────────────────────────────────────────┘
```
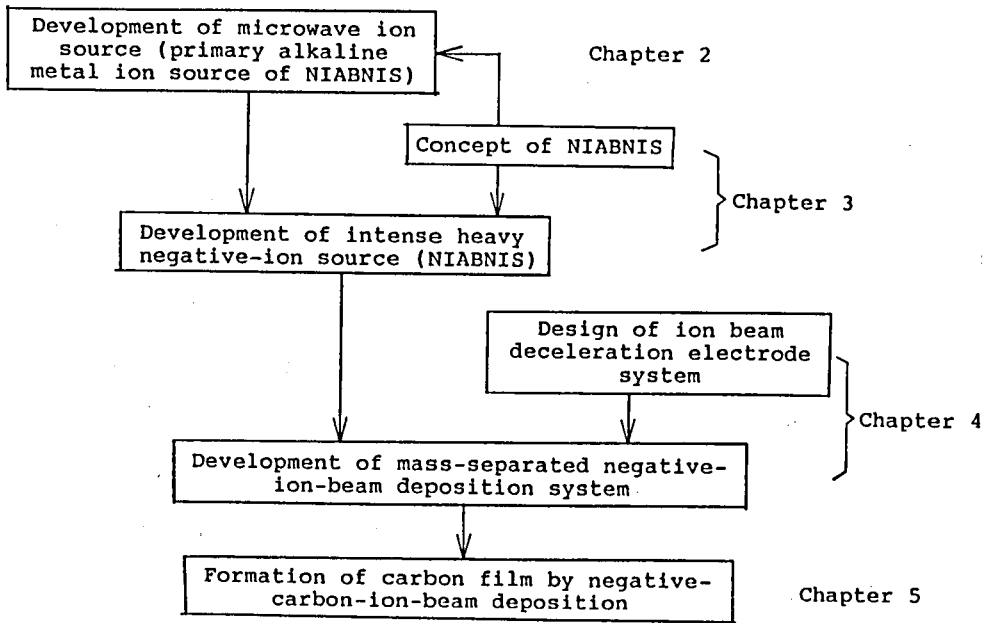
Fig. 1.1   Flow chart of research program and

content in each chapter.

characteristics of this microwave ion source are described in detail.

Next, the intense heavy negative-ion source called neutral- and ionized-alkaline-metal bombardment-type heavy negative-ion source, NIABNIS, was developed. The NIABNIS produces 0.74 mA of a C^- ion beam, the highest current in the world, which is enough to form a film by negative-ion-beam deposition. In chapter 3, after a brief outline of theoretical background on the mechanisms of negative ion production by sputtering, construction and operational characteristics of the NIABNIS are described in detail.

The mass-separated negative-ion-beam deposition system was developed for the film formation by depositing the negative ion beam produced by the NIABNIS. Difference of the construction between positive- and negative-ion-beam deceleration systems and a new concept of arrangement of the deceleration electrodes are shown in chapter 4.

Finally, carbon film was deposited by the mass-separated negative-ion-beam deposition. Various properties of the carbon films deposited by the C^- or C_2^- ion beam were investigated mainly with regard to the dependency on the deposited ion beam energy. The results are discussed in chapter 5.

The flow chart of this research is shown in Fig. 1.1.

References (Chapter 1)

1) H.S.W.Massey, Negative Ions, 3rd ed., (Cambridge Univ. Press, 1976).

2) K.H.Purser, R.B.Liebert, A.E.Litherland, R.P.Beukens, H.E.Gove, C.L.Bennett, M.R.Glover, and W.E.Sondheim, Rev. Phys. Appl. **12**, 1487 (1977).

3) T.S.Noggle, B.R.Appleton, J.M.Williams, and O.S.Oen, Proceedings of the Fourth Conference on Applications of Small Accelerators, 76CH 1175-9 NPS (1976), p.255.

4) Y.Qiu, J.E.Griffith, W.J.Meng, and T.A.Tombrello, Radiation Effects **70**, 231 (1983).

5) J.M.Dawson, H.P.Furth, and F.H.Tenney, Phys. Rev. Lett. **26**, 1156 (1971).

6) H.P.Furth and D.L.Jassby, Phys. Rev. Lett. **32**, 1176 (1974).

7) P.Williams and C.A.Evans, NBS Spec. Pub. **427**, 63 (1975).

8) C.A.Houser, I.S.Tsong, W.B.White, P.D.Miller, and C.D.Moak, Radiation Effects **64**, 103 (1982).

9) T.Takagi, Proceedings of the International Ion Engineering Congress, Kyoto (Institute of Electrical Engineers of Japan, Tokyo, 1983), p.785.

10) J.A.Weinman and J.R.Cameron, Rev. Sci. Instrum. **27**, 288 (1956).

11) G.D.Alton, Proceedings of the International Ion Engineering Congress, Kyoto (Institute of Electrical Engineers of Japan, Tokyo, 1983), p.85.

12) J.Ishikawa, Proceedings of the Eighth Symposium on Ion Sources and Ion-Assisted Technology, Tokyo (The Research Group

of Ion Engineering, Kyoto University, 1984), p.1.

13) K.Prelec, Proceedings of the International Ion Engineering Congress, Kyoto (Institute of Electrical Engineers of Japan, Tokyo, 1983), p.47.

14) K.W.Ehlers, Proceedings of the International Ion Engineering Congress, Kyoto (Institute of Electrical Engineers of Japan, Tokyo, 1983), p.59.

15) M.Mueller and G.Hortig, IEEE Trans. Nucl. Sci. **NS-16**, 38 (1969).

16) R.Middleton and C.T.Adams, Nucl. Instrum. Methods **118**, 329 (1974).

17) H.H.Andersen and P.Tykesson, IEEE Trans. Nucl. Sci. **NS-22(3)**, 1632 (1975).

18) J.R.Hiskes, A.Karo, and M.Gardner, J. Appl. Phys. **47**, 3888 (1976).

19) M.L.Yu, Phys. Rev. Lett. **40**, 574 (1978).

20) For example, See Proceedings of the International Ion Engineering Congress, Kyoto (Institute of Electrical Engineers of Japan, Tokyo, 1983).

21) T.Takagi, Thin Solid Films **92**, 1 (1982).

22) T.Takagi, J. Vac. Sci. Technol. **A2**, 382 (1984).

23) C.Weissmantel, J. Vac. Sci. Technol. **18**, 179 (1981).

24) J.M.E.Harper and J.J.Cuomo, J. Vac. Sci. Technol. **21**, 737 (1982).

25) G.E.Thomas and E.E.de Kluizenaar, Proceedings of 3rd International Congress on Surface Physics and Chemistry, Grenoble, 1977 (Société Française du Vide, Paris, 1977), p.136.

26) J.Amano, P.Bryce, and R.P.W.Lawson, J. Vac. Sci. Technol. **13**, 591 (1976).

27) J.Amano and R.P.W.Lawson, J. Vac. Sci. Technol. **15**, 113 (1978).

28) K.Miyake, K.Yagi and T.Tokuyama, Inst. Phys. Conf. Ser. No.38 (1978), p.78.

29) T.Miyazawa, S.Misawa, S.Yoshida, and S.Gonda, J. Appl. Phys. **55**, 188 (1984).

30) A.Fontell and E.Arminen, Can. J. Phys. **47**, 2405 (1969).

31) J.H.Freeman, W.Temple, D.Beanland, and G.A.Gard, Nucl. Instrum. Methods **135**, 1 (1976).

Chapter 2

AXIAL MAGNETIC FIELD EXTRACTION–TYPE MICROWAVE ION SOURCE
WITH A PERMANENT MAGNET

2.1 Introduction

A high current, high efficient and compact plasma ion source is required for the primary alkaline ion source of the intense sputter negative-ion source which utilizes neutral alkaline particle bombardment as described in chapter 1. Generally, a high-current ion source should have a plasma with a high ion density and a high-electron temperature because the ion saturation current from the plasma is proportional to the product of plasma ion density and square root of electron temperature. At the same time, the ion temperature should be low enough to obtain an ion beam with a low energy spread and low emittance.

One of the most effective methods to obtain a high density of ionizing electrons in the plasma is the electron-cyclotron resonance (ECR) process, in which a microwave with a frequency close to the electron-cyclotron frequency is introduced into a magnetized plasma. When the plasma electrons are selectively heated by means of the ECR process, only the electron temperature can be increased while the ion temperature is kept low. Therefore, the ECR process is quite suitable for production of high-density, singly charged ions[1,2]. This implies that the ECR

process is also effective for successive ionization of multiply charged ions under an appropriate condition[3,4].

The magnetic field of the ECR ion source is important both to plasma production and to ion extraction. As for plasma production, a dc magnetic field for electron-cyclotron resonance corresponding to the microwave frequency is required. The magnetic field is also utilized for preventing the generated plasma, especially hot electrons, from diffusing to the wall of the plasma production chamber[5]. On the other hand, low velocity ions generated in the plasma production chamber move easily along the magnetic force lines. Thus, these magnetic force lines should be perpendicular to the ion emitting surface formed on the extraction aperture, so that high-density ions are transported to the extraction aperture. One of the methods to obtain the above-mentioned magnetic field is utilization of a solenoid. However, since a kilogauss order of magnetic field is required for ECR, the size of the solenoid is large and the power consumption is high. If these magnetic force lines are formed by using a permanent magnet, a compact and low input power microwave ion source can be obtained.

A new type of microwave ion source was developed in which a permanent magnet generates the axially directed magnetic field needed for the electron-cyclotron resonance and the ion extraction. This compact microwave ion source is not only suitable for the primary ion source of the intense negative-ion source, but also useful for a wide range of applications such as accelerators, sputtering, etching and deposition. Therefore, detailed characteristics of this microwave ion source are

described in the followings.

2.2 Source Construction and Operating Principle

The illustration of the operating principle of the axial magnetic field extraction-type microwave ion source with a permanent magnet[6-8] is shown in Fig. 2.1. By the combination of the permanent magnet and ferromagnetic materials, a closed magnetic circuit is formed through the gap between the protrusion in the plasma production chamber and the ion-extraction electrode. This axial magnetic field is utilized both for the high-density plasma production by the ECR process and for the high efficient ion extraction by transporting the generated ions along the magnetic force lines. The structure of the ion source is shown in Fig. 2.2. The permanent magnet is doughnut shaped (50 mm in outer-diameter, 40 mm in inner-diameter, and 15 mm in height) and is made of Co-Sm. The residual magnetic flux density is 9.7 kG and its magnetized direction is axial. The magnetic strength begins to decrease over the temperature of 500 °C. The middle flange made of ferromagnetic materials is placed on the permanent magnet, and a part of this flange protrudes into the plasma production chamber. A part of the base flange under the permanent magnet is made of ferromagnetic materials for the magnetic route and the other part is made of nonferromagnetic materials. The ion-extraction electrode made of ferromagnetic materials is magnetically connected with the lower end of the permanent magnet, but is electrically insulated by ceramic. A sufficient ion-extraction voltage can be applied to the
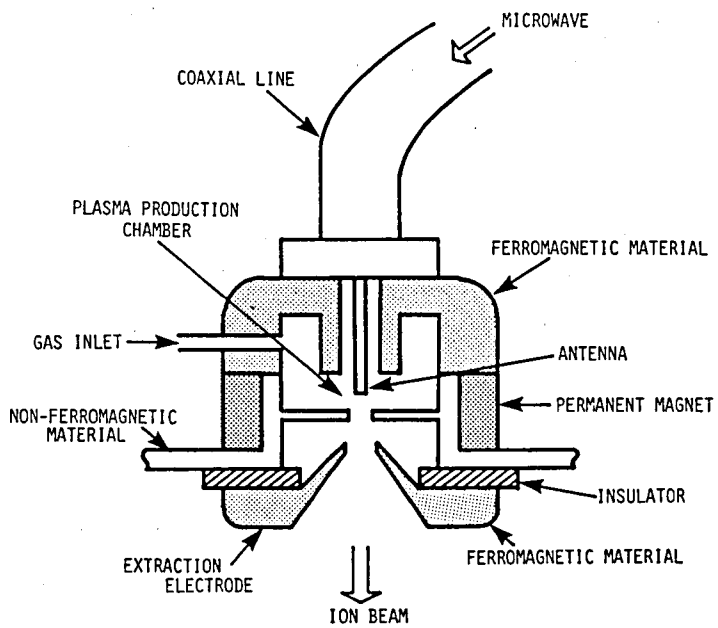
18

Fig. 2.1   Illustration of the operating principle
of the axial magnetic field extraction-type
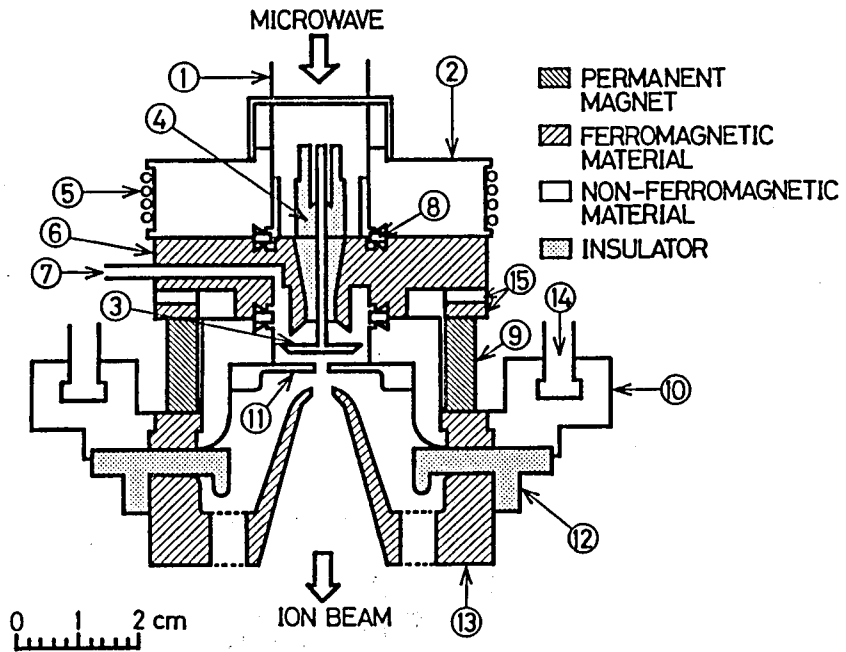microwave ion source with a permanent magnet.

Fig. 2.2   Structure of the axial magnetic field
extraction-type microwave ion source. (1) Sealed
coaxial connector, (2) top flange, (3) antenna,
(4) boron nitride, (5) sheath-heater, (6) middle
flange, (7) gas inlet, (8) copper gaskets, (9)
permanent magnet, (10) base flange, (11) plate
with an extraction aperture, (12) macor insulator,
(13) extraction electrode, (14) coolant, and (15)
ferromagnetic or nonferromagnetic spacers. By the
combination of doughnut-shaped permanent magnet
and ferromagnetic materials, a closed magnetic
circuit is generated with an axial magnetic
field.

20

extraction electrode. In this way, a closed magnetic circuit is formed passing through the ion-extraction electrode. The magnetic field strength of the gap between the protrusion in the plasma production chamber and the ion-extraction electrode is 850 to 1200 G. The plate with an ion-extraction aperture is made of nonferromagnetic materials. In the experiments the diameter of the ion-extraction aperture and the length of the ion-extraction gap are fixed at 2 mm and 3 mm, respectively, although they are changeable.

The strength of the magnetic field corresponding to the electron-cyclotron frequency of 2.45 GHz is 875 G. The input microwave power, therefore, is absorbed by the electron-cyclotron resonance process. The microwave is fed through a coaxial line and is supplied to an antenna through a sealed coaxial connector on the top flange. The antenna, which is inserted in the hole at the center of the protrusion, protrudes into the plasma production chamber. As a result, the microwave power is fed into the plasma production chamber. The antenna is T shaped as shown in Figs. 2.3 (a) and (b), and made of molybdenum or stainless-steel wire of 1.5 mm in diameter. By sharpening the edges of the horizontal part of the antenna, a high electric field of the microwave is concentrated on the gap between the edge and the wall of the plasma production chamber. Therefore, the microwave discharge is stably maintained even at a low gas pressure. The similar effect is expected for a spiral shaped antenna as shown in Fig. 2.3 (c), where a high electric field of the microwave can be applied between the spiral center and the spiral end by adjusting the spiral length. A boron nitride tube is packed near
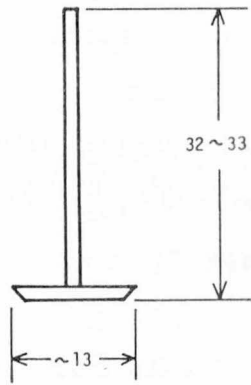
(a)
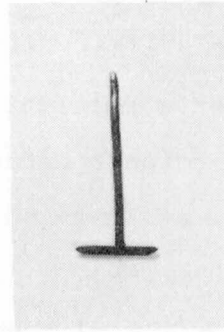
(b)
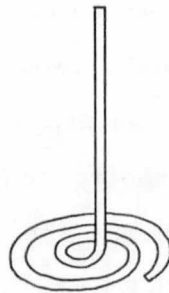
(c)

Fig. 2.3   Antennas protruding into the plasma
production chamber. The microwave power is
supplied into the plasma production chamber
through the antenna. (a) Drawing and (b)
photograph of a T shaped antenna. (c) Drawing
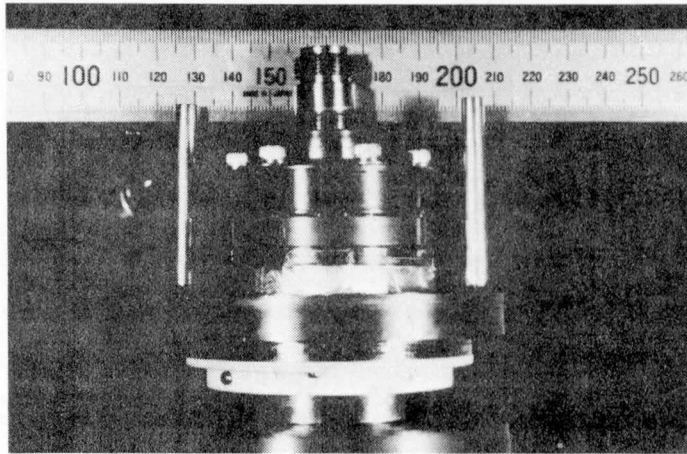of a spiral shaped antenna.

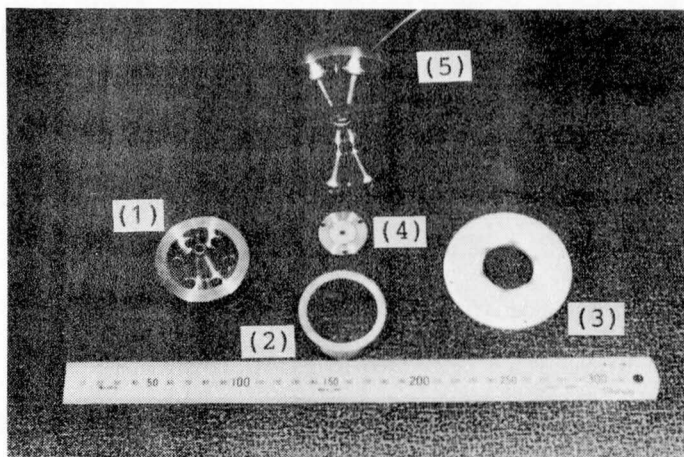Fig. 2.4   Photograph of the side view of the
microwave ion source.

Fig. 2.5   Photograph of the parts of the microwave
ion source. (1) Ion-extraction electrode, (2)
permanent magnet, (3) macor insulator, (4) plate
with an extraction aperture, and (5) base flange.

the antenna shank in order to prevent microwave discharge there. This also protects the coaxial connector. The plasma production chamber is 16 mm in diameter and 5 mm in effective height, and is not a resonant cavity structure.

Since the ion source is sealed by copper gaskets, its temperature can be raised up to 450 $^\circ$C. In order to raise the source temperature for obtaining metal ions such as cesium and rubidium, a sheath-heater line is wound around the ion source. Since the base flange is cooled by water, the temperature is low enough to use a Viton O ring. The gas or metal vapor to be ionized is fed through a stainless-steel pipe into the plasma production chamber. The size of this compact ion source is 50 mm in diameter and 65 mm in height. Figure 2.4 shows a photograph of the side view of the ion source, and a photograph of the parts of the ion source is shown in Fig. 2.5.

A microwave is generated by a magnetron and the microwave power can be varied by controlling the anode current of the magnetron. A continuous wave with a frequency of 2.45 GHz is used. Figure 2.6 shows the system supplying the microwave power to the ion source. The reflected microwave power is detected through the circulator. Thus, the net microwave power consumed in the ion source can be measured. In the experiments the difference between the supplied and reflected microwave powers to the ion source was taken as the input microwave power. The reflected microwave power, however, is small and less than 20 W without tuning since impedance of the parts of the microwave input system is all matched at 50 Ω. Therefore, the reflected microwave power need not always be isolated by the circulator.

COAXIAL
LINE   CIRCULATOR
ION SOURCE

P.S.

MAGNETRON

ATTENUATOR
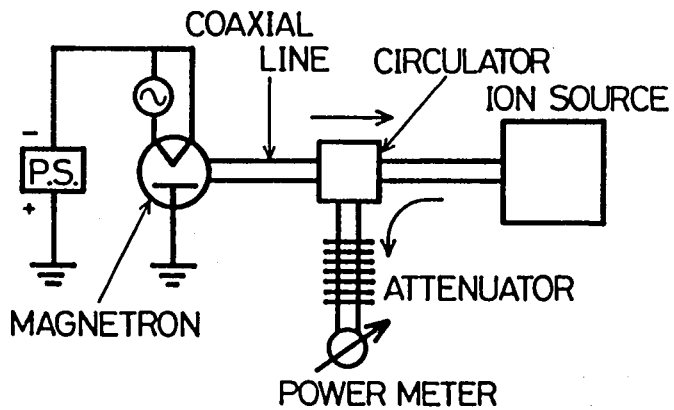
POWER METER

Fig. 2.6   Input system of the microwave to the ion

source.   The microwave power generated by

magnetron is transmitted through the coaxial line.

The reflected microwave power which is separated

by the circulator is detected by the power meter.
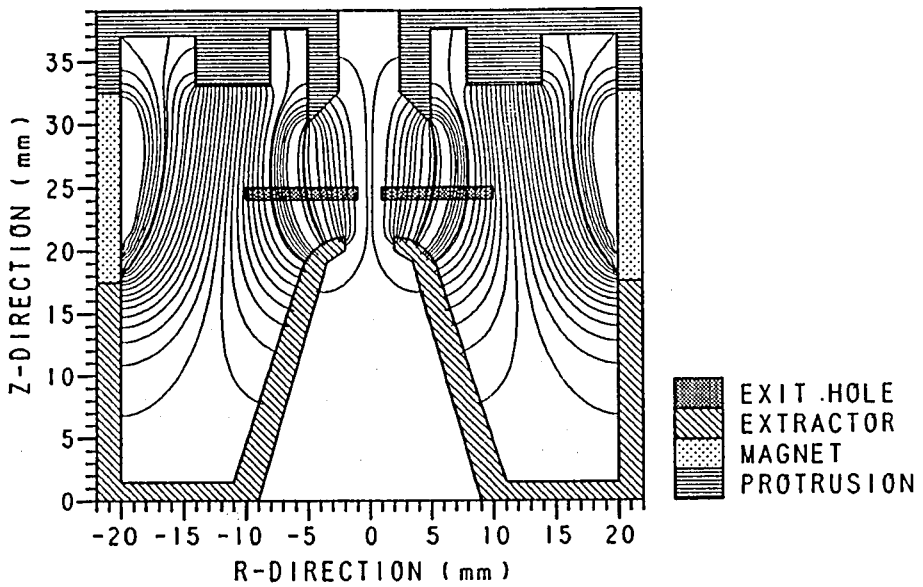
Fig. 2.7   Results of the calculations of magnetic
force lines in the wide range including the
permanent magnet.   Notice that the plate with the
ion-extraction aperture is placed at the middle of
both poles of the permanent magnet.

2.3 Magnetic Force Lines

The shape of the magnetic force lines near the ion-extraction aperture is important. These magnetic force lines can be calculated by a digital computer. The calculation method and the assumptions made in it are described in Appendix A together with the flow chart of the program. Figure 2.7 shows the results of a wide range of calculations including the permanent magnet. All the magnetic force lines from the ferromagnetic protrusion terminate at the ion-extraction electrode. The plate with the ion-extraction aperture is placed at the middle of both poles of the permanent magnet. The inner diameter of the permanent magnet is four times that of the protrusion. The magnetic force lines from the poles do not directly influence the magnetic field of the gap between the protrusion and the ion-extraction electrode.

The results of the calculations of the magnetic force lines in the restricted region from the plasma production chamber to the ion-extraction electrode are shown in Fig. 2.8. Since the dc electric field cannot penetrate the plasma, the motion of ions is determined by the magnetic field and the collisions among the particles in the plasma. The Larmor radius and the mean-free path[9] of the Ar^+ ion are, for instance, 5 and 27 mm, respectively, assuming that the ion temperature is 0.5 eV and the magnetic field strength is 1 kG. Then, the ions in the plasma are not always frozen by the magnetic force lines, but most of them will diffuse along the magnetic force lines. The ions generated near the center are concentratedly transported to the ion emission surface along the magnetic force lines, and are
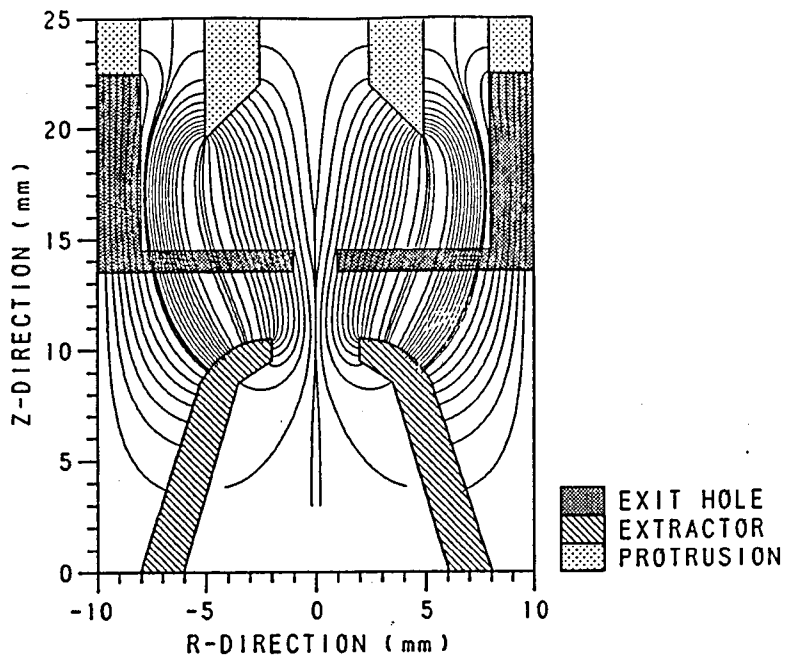
27

Fig. 2.8   Results of the calculations of magnetic

force lines in the restricted region from the

plasma production chamber to the ion-extraction
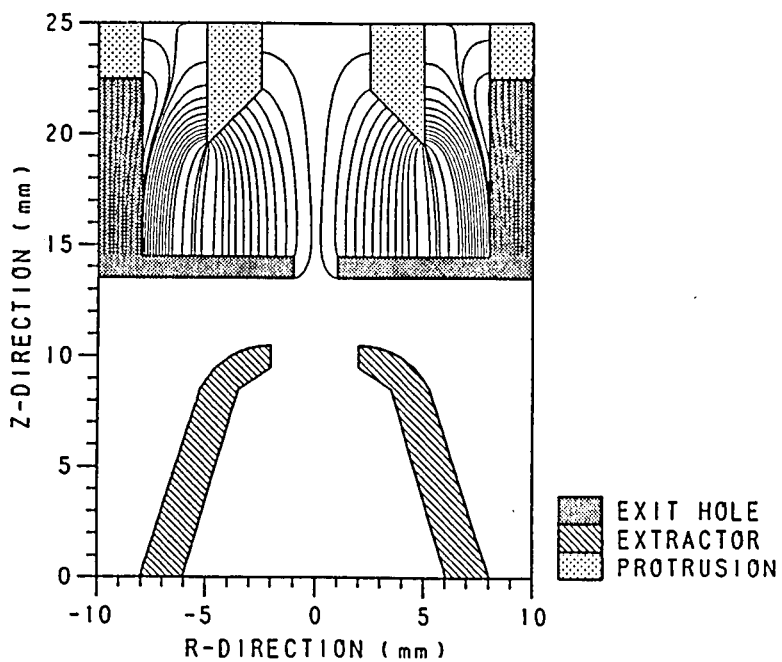
electrode.

Fig. 2.9 Results of the calculations of the
magnetic force lines when the ion-extraction
electrode is made of nonferromagnetic materials
and the plate with the extraction aperture is made
of ferromagnetic materials.

extracted by the electric field to the ion-extraction electrode. On the other hand, Fig. 2.9 shows the results of the calculations when the ion-extraction electrode is made of nonferromagnetic materials and the plate with the extraction aperture is made of ferromagnetic materials. All the magnetic force lines from the protrusion terminate at the plate with the extraction aperture. The direction of the magnetic force lines near the extraction aperture is almost perpendicular to the direction of the ion extraction. Therefore, it is difficult to extract a high-density ion current.

By the combination of the permanent magnet and ferromagnetic materials, the axial magnetic field is formed in the limited space from the protrusion to the ion-extraction electrode in this ion source. High-density ions, therefore, can be extracted. Moreover, it is possible to optimize the magnetic field by varying the configuration of the protrusion or the extraction electrode.

2.4 Ion Beam Trajectories

In order to examine the ion-extraction characteristics, ion beam trajectories are simulated by a digital computer. An ion beam with a high velocity has a mean free path of more than a few tens of centimeters even at an argon gas pressure of 10^{-4} Torr. Therefore, the ion beam trajectories in the extraction region can be calculated by a computer simulation program in which the collision effects are ignored. The basic idea and the method for the simulation of the ion beam trajectories including the self-
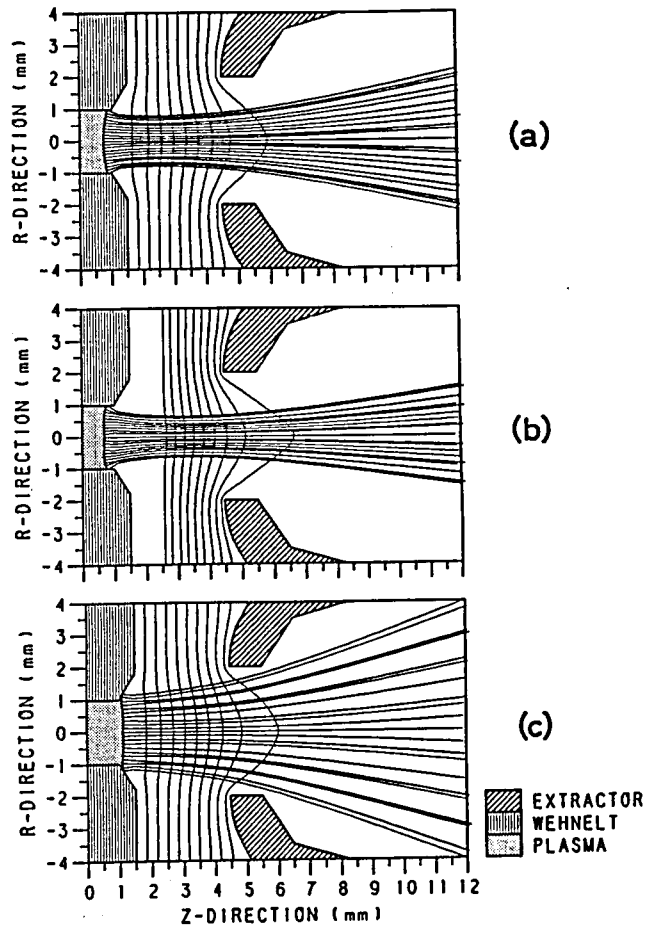
Fig. 2.10   Results of the simulation of Ar$^+$ ion
trajectories : (a) the ion-extraction voltage is
15 kV, the plasma density 2×10^{12} cm^{-3}, and the
plasma-electron temperature 5 eV, (b) the ion-
extraction voltage is 20 kV and the other
parameters are the same as those in (a), and (c)
the plasma density is 4×10^{12} cm^{-3} and the other
parameters are the same as those in (a).   The
equipotential lines are also drawn in the figures.

31

determination of the ion emitting surface (plasma boundary) are described in Appendix B. The flow chart of the program is also shown in the Appendix. Figure 2.10 (a) shows the results of the simulation of Ar^+ ion trajectories under the conditions where the ion-extraction voltage is 15 kV, the plasma density 2×10^{12} cm^{-3}, and the plasma electron temperature 5 eV. The ion emitting surface is concave, but the ion-extraction electrode system forms a divergent lens. Then, a slightly diverged ion beam is obtained. Figure 2.10 (b) shows the results of the simulation under the conditions where the ion-extraction voltage is 20 kV, and the other parameters are the same as those in Fig. 2.10 (a). As the ion-extraction voltage is increased, the plasma retreats, and the extracted ion beam is more converged. Figure 2.10 (c) shows the results of the simulation under the conditions where the plasma density is 4×10^{12} cm^{-3}, and the other parameters are the same as those in Fig. 2.10 (a). The extracted ion beam is diverged and turbulent.

Since the aspect ratio of the ion extraction system, which is defined as the ratio of the diameter of the ion-extraction aperture to the length of the ion-extraction gap, is high (2/3), the plasma density and the ion-extraction voltage have to be simultaneously adjusted in order to extract a well-converged ion beam with a small divergent angle.

2.5 Ion Beam Characteristics

2.5.1 Ion-extraction characteristics

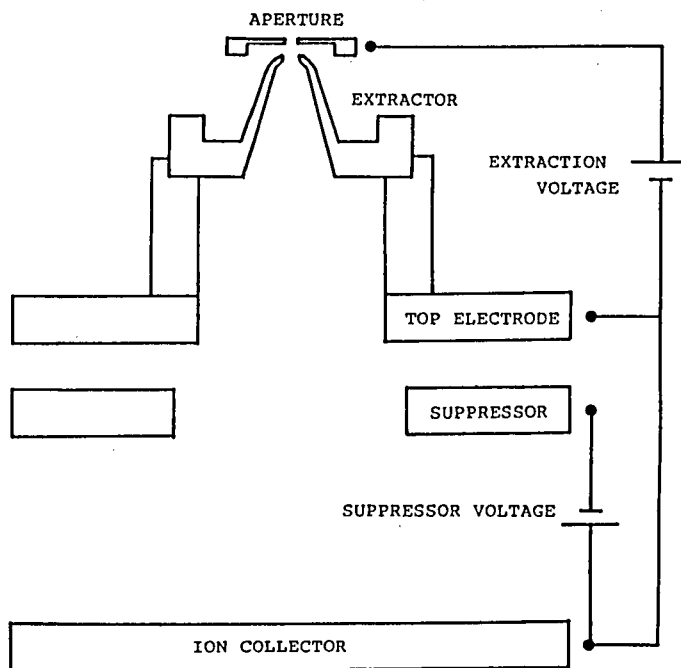The extracted ion current was measured by a Faraday cup,

32

Fig. 2.11   Structure of the Faraday cup, by which

the extracted ion current was measured.   The

suppressor was negatively biased by 150 V against

the ion collector.

which consisted of a top electrode, a secondary electron suppressor, and an ion collector, as shown in Fig. 2.11. The aperture of the top electrode and the secondary electron suppressor were 37 and 52 mm in diameter, respectively. The distance between the top electrode and the suppressor was 22 mm, and the distance between the suppressor and the ion collector 49 mm. The Faraday cup was placed below the ion-extraction aperture at a distance of about 60 mm. The suppressor was negatively biased by 150 V against the ion collector. The potentials of the top electrode and the ion collector were the same as the ion-extraction electrode. A continuous microwave was supplied for the plasma production, and the ion beams were extracted continuously in the experiments.

Figure 2.12 shows the extracted ion current as a function of the ion-extraction voltage with variation in Ar gas pressure in the plasma production chamber. The theoretical maximum current is indicated by the dotted line, which is the space-charge-limited current under the two parallel plate system having an aspect ratio of 2/3[10]. A few milliamperes of Ar^+ ion current was extracted at a relatively low gas pressure of 10^{-3} Torr order and a low input microwave power of 20 - 30 W. When the ion-extraction voltage was 15 kV, the extracted ion current reached 3.0 mA. The high-current density of 95.5 mA/cm^2 and the current density normalized by proton of 604 mA/cm^2 were obtained. It was found that the extracted ion current characteristics were divided into two regions: the space-charge-limited region and the plasma-density-limited region. These correspond to the space-charge-limited region and the temperature-limited region, respectively,

Fig. 2.12   Extracted ion current as a function of
the ion-extraction voltage with variation in Ar
gas pressure in the plasma production chamber.
The argon gas pressures (Torr) are : ▼ 6.0×10^{-4},
△ 1.2×10^{-3}, □ 2.4×10^{-3}, ▽ 4.2×10^{-3}, ○ 6.0×10^{-3},
and ■ 1.2×10^{-2}. The dotted line indicates the
theoretical extractable maximum current. The
input microwave power is 20 - 30 W.

Fig. 2.13   Extracted ion current as a function of

the ion-extraction voltage in the case of cesium

metal vapor.   The cesium oven temperature (°C) and

input microwave power (W) are ☐ 186 °C, 7 W :

△ 196 °C, 13 W : and ○ 202 °C, 19 W.   The dotted

line indicates the theoretical extractable maximum

current.

of an electron gun. The ion current was extracted according to the 3/2 power law and reached the ion saturation current, which corresponded to the space-charge-limited region. The extracted ion current hardly increased at a higher extraction voltage than the minimum voltage which was sufficient to extract the ion saturation current. This voltage region was the plasma-density-limited region. The generated plasma density, which contributed to the ion saturation current, varied with the gas pressure and the input microwave power. The ratio of the ion current detected by the Faraday cup to the drain current of the high-voltage power supply was about 85 % in the vicinity of the minimum voltage which was sufficient to extract the ion saturation current.

The extracted ion current as a function of the ion-extraction voltage in the case of cesium metal which has a low melting point and high vapor pressure is shown in Fig. 2.13. When using metal vapor, as well as usual gases, the extracted ion current characteristics were divided into those two regions. The plasma density could be controlled by the input microwave power and the oven temperature. At the ion extraction voltage of 13 kV the extracted ion current reached 1.75 mA. The current density of 55.7 mA/cm^2 and the current density normalized by proton of 642 mA/cm^2 then were obtained. Since the ionization potential of cesium 3.88 eV is very low, the input microwave power is less than 20 W. The extracted ion current as a function of the ion-extraction voltage when using the reactive oxygen gas is shown in Fig. 2.14. Since there was no hot electrode in the plasma production chamber, long-time operation was possible even when the reactive gas was used. After a few hours, the stainless-
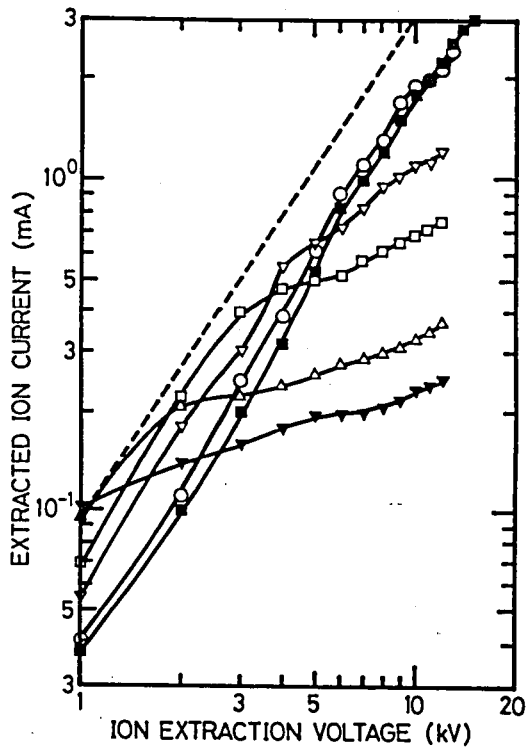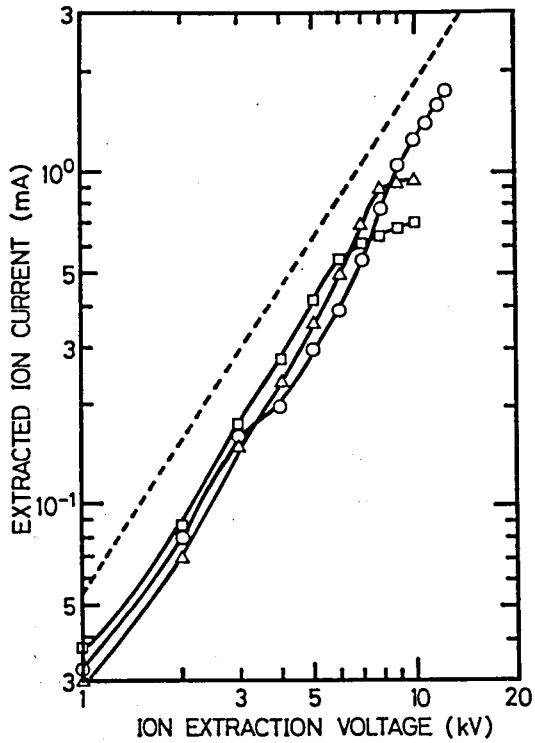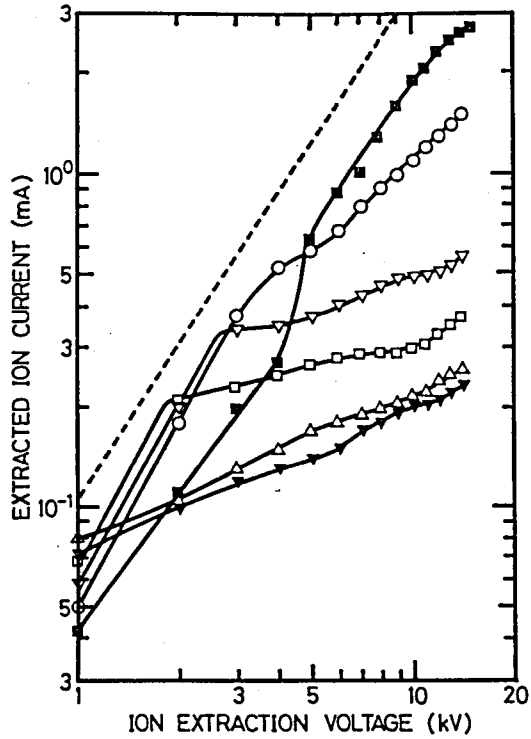
Fig. 2.14 Extracted ion current as a function of the ion-extraction voltage with variation in O_2 gas pressure in the plasma production chamber. The oxygen gas pressures (Torr) are : ▼ 9.0×10^{-4}, △ 1.8×10^{-3}, □ 3.6×10^{-3}, ▽ 6.3×10^{-3}, ○ 9.0×10^{-3}, and ■ 1.8×10^{-2}. The dotted line indicates the theoretical extractable maximum current. The input microwave power is 21 - 26 W.
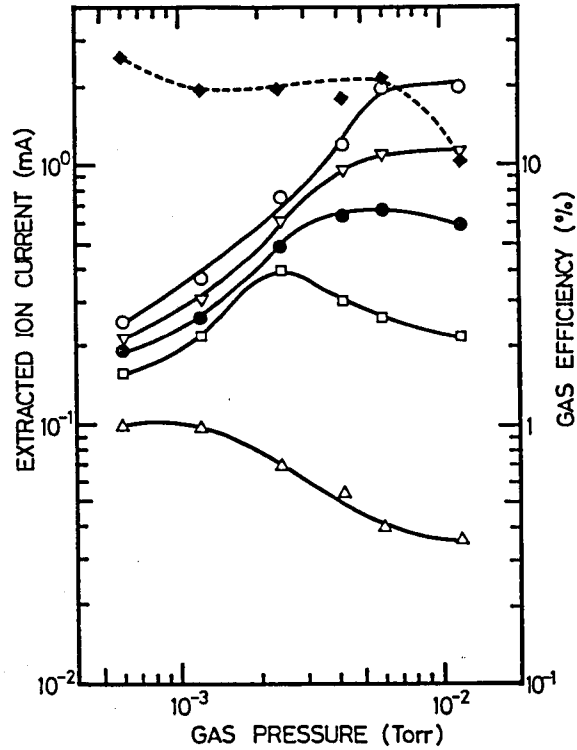
Fig. 2.15 Extracted ion current as a function of
the argon gas pressure in the plasma production
chamber. The parameter is the ion-extraction
voltage (△ 1.0 kV, □ 3.0 kV, ● 5.0kV, ▽ 8.0kV,
and ○ 12.0 kV). The dotted line indicates the gas
efficiency when the ion extraction voltage is 12.0
kV. The input microwave power is 17 - 19 W.

steel antenna was only slightly oxidized. The extracted ion current reached 2.7 mA at the ion-extraction voltage of 15 kV. The current density then was 85.9 mA/cm^2.

The extracted ion current as a function of the argon gas pressure in the plasma production chamber is shown in Fig. 2.15. The parameter is the ion-extraction voltage. The gas efficiency at the ion-extraction voltage of 12 kV is also shown. The microwave discharge was maintained even at a gas pressure of 10^{-4} Torr order. The gas efficiency was relatively high (20%), and it could be higher if the materials with lower ionization potentials were discharged. The gas efficiency did not vary in the gas pressure range of 10^{-3} Torr order. Hence, the plasma density can be controlled by the gas pressure. When the ion-extraction voltage was low, the ion current showed the peak at a certain gas pressure. It seems that the gas pressure, i.e., the plasma density, on this peak was the gas pressure having the optimal ion-extraction optics at this voltage. The extracted ion currents were also increased with an increase in the input microwave power. The increase in the extracted ion current, however, tended to saturate at higher input microwave powers. It is noted that the microwave discharge was maintained even at a few Watts of the input microwave power.

2.5.2 Mass spectrum

Mass spectrum measurements were made by injecting a part of the extracted ion beam to the sector magnet-type mass separator with a deflection angle of 90° and a radius of curvature of 500 mm. An example of the mass spectrum of the argon ion beam is

Fig. 2.16 An example of the mass spectrum of the argon ion beam under the conditions where the gas pressure is 2.1×10^{-3} Torr, the extraction voltage 7 kV, and the input microwave power 25 W.

shown in Fig. 2.16. The yield of singly charged ions was more than 95 %, while that of doubly charged ions was less than 5 %. Since the shape of the magnetic force lines was not for a plasma confinement structure, the yield of the singly charged ions was high. The yield of the doubly charged ions, however, tended to increase when the gas pressure of the plasma production chamber became lower and the input microwave power was increased. Figure 2.17 shows the mass spectrum of the nitrogen ion beam. The yield of molecular ions was higher than that of atomic ions. The yield of atomic ions was increased with a decrease in the gas pressure of the plasma production chamber and with an increase in the input microwave power. For the oxygen ion beam, the similar mass spectrum was obtained, although the ratio of the atomic ion beam was a little higher than that for the nitrogen ion beam. There was a negligible amount of impurity included in the extracted ion beam in these cases. Since there is no electrode to be damaged during operation, such as a filament, in the plasma production chamber, long-time operation is possible and the ion source lifetime is long even when using O_2 gas having a strong reactivity.

The mass spectrum of the cesium ion beam is shown in Fig. 2.18. The electron temperature of the cesium plasma was low because of the very low ionization potential of the cesium. Elements except for cesium were hardly ionized. Hence, the impurity included in the ion beam was nonexistent. This is the advantage of the microwave ion source, in which the ionization is not done by the high-energy electron beam from the cathode, but by the plasma electrons with a uniform low energy.

42

The figure contains the following labels:

N₂ GAS PRESSURE IN DISCHARGE CHAMBER : 4.6x10⁻³Torr
ION EXTRACTION VOLTAGE : 7.0kV
INPUT MICROWAVE POWER : 33Watt

With peaks labeled N^{2+}, N^+, N_2^+, traces labeled x10 and x2.5, and axis labeled MASS/CHARGE with marks at 0, 1, 5, 10, 20, 30, 40.
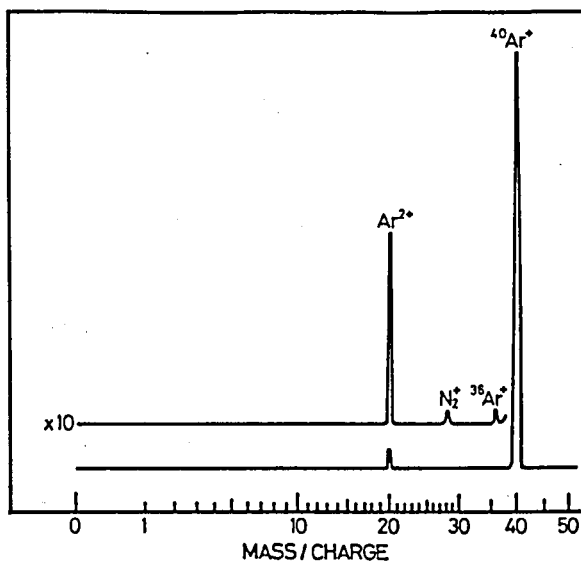
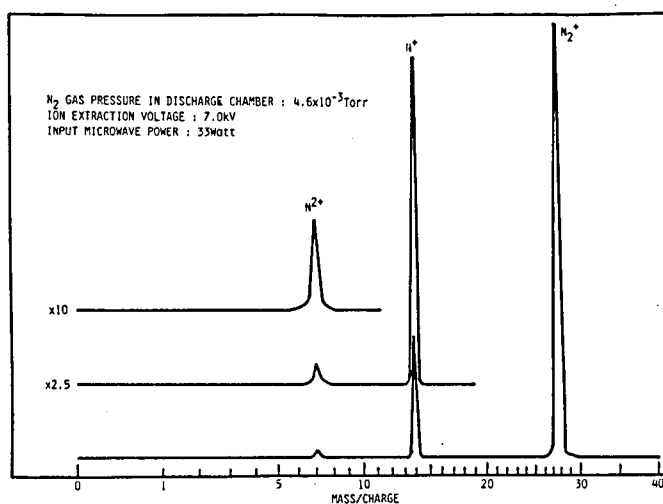Fig. 2.17   An example of the mass spectrum of the
nitrogen ion beam under the conditions where the
gas pressure is 4.6×10^{-3} Torr, the extraction
voltage 7 kV, and the input microwave power 33 W.
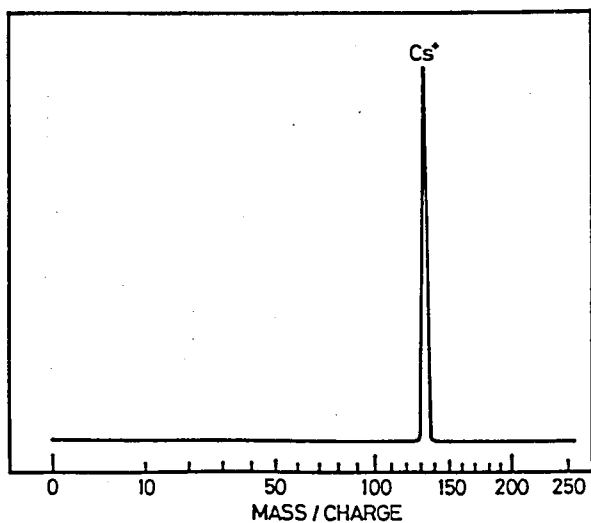
Fig. 2.18   An example of the mass spectrum of the
cesium ion beam under the conditions where the
oven temperature is 183 ^{O}C, the ion-extraction
voltage 10 kV, and the input microwave power 11 W.

44

2.5.3 Emittance

An emittance measurement was made in accordance with the known principle of the emittance determination[11]. Our emittance measurement system consisted of a plate with a series of holes of 0.5 mm in diameter and a movable wire detector of 25 μm in diameter. The distance between the plate and the wire detector was 165 mm. The emittance diagram of the extracted ion beam is shown in Fig. 2.19. The emittance contour line was drawn so that the ion current corresponding to the area enclosed by the contour line could be 86.5 % of the total ion beam current. This percentage was derived from the root-mean-square emittance[12]. The normalized emittance ϵ_{2n} was defined as

$$\epsilon_{2n} = (v/c)[1-(v/c)^2]^{-1/2}(A/\pi), \qquad (2.1)$$

where v is the velocity of the ion beam, c the light velocity, and A the area enclosed by the emittance contour line[13]. The normalized brightness B_n was defined as

$$B_n = 2I/(\pi\epsilon_{2n})^2, \qquad (2.2)$$

where I is the 86.5 % ion current[13]. From the diagram in Fig. 2.19 the normalized emittance was estimated to be 3.7×10^{-8} m·rad, and the normalized brightness was calculated at 1.8×10^{11} A·m^{-2}·rad^{-2}. The normalized emittance and the normalized brightness as a function of the input microwave power are shown in Fig. 2.20. The normalized emittance was 10^{-8} m·rad order and the normalized brightness was 10^{11} A·m^{-2}·rad^{-2} order. The experimental results show that this microwave ion source can deliver an ion beam with low emittance and high brightness. This is because the plasma electrons are selectively heated by the electron-cyclotron resonance, but the plasma ions are not. The dimensions of this
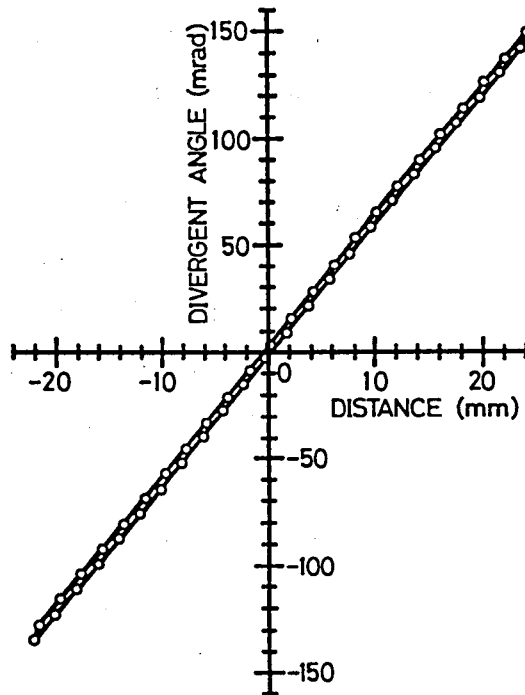
Fig. 2.19   Emittance diagram of the extracted argon
ion beam under the conditions where the ion-
extraction voltage is 10 kV, argon gas pressure
3.4×10^{-3} Torr, and the input microwave power 15 W.
In the emittance measurement, the diameter of the
extraction aperture was 3 mm.   The normalized
emittance is 3.7×10^{-8} m·rad and the normalized
brightness 1.8×10^{11} A·m^{-2}·rad^{-2}.

46
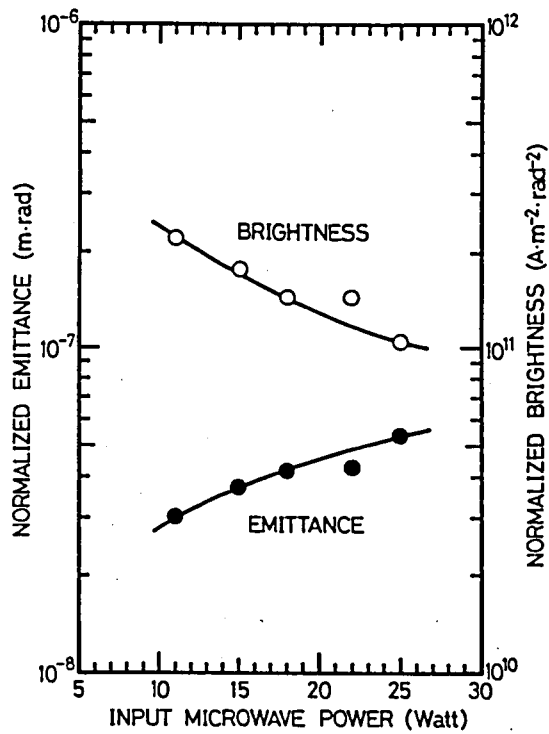
Fig. 2.20   Normalized emittance and the normalized
  brightness as a function of the input microwave
  power (● emittance and ○ brightness).   The
  experimental conditions: the gas pressure is
  3.4×10^{-3} Torr and the ion-extraction voltage 10
  kV.

ion source is not only structurally small, but also small for ion beam optics.

The ion beam divergence half-angle was also measured with the emittance measurement system, and it was estimated at about 5°. This value was relatively high since the ion-extraction system used was the two-electrode ion accelerator. With this ion-extraction system, the leakage of electrons back to the plasma production chamber through the ion accelerator will introduce space-charge forces to the ions in the beam so formed. In an ion beam with low emittance but high divergence, high virtual brightness [(current density)/(divergent angle)^2] is potentially possible but is not obtained in the present accelerator configuration. The large beam divergence and the 15 % difference between the power supply drain current and the measured ion current could be improved substantially if an accel-decel ion accelerator was to be used.

2.6 Discussion

From the ion saturation current I_{pi}(A), the plasma density n_i can be estimated at

$$n_i = I_{pi}(3.0 \times 10^{-13} \, a^2 \, M^{-1/2} \, T_e^{-1/2})^{-1} \quad (cm^{-3}), \qquad (2.3)$$

where a is the radius of the extraction aperture (cm), M the atomic mass number, and T_e the electron temperature (eV). From Fig. 2.12 the ion saturation current is about 3.0 mA. Assuming that the electron temperature is 5 eV[1], the plasma density is estimated at 2.8×10^{12} cm^{-3}. Table 2.1 shows the maximum ion current, the current density, the current density normalized by

Table 2.1   Maximum ion current, the current
density, the current density normalized by proton,
and the estimated plasma density for various gases
and metal vapors.

MATERIAL	MAX. ION CURRENT (mA) (EXTRACTION VOLTAGE) (kV)	CURRENT DENSITY (mA/cm^2)	CURRENT DENSITY NORMALIZED BY PROTON (mA/cm^2)	PLASMA DENSITY (cm^{-3})
Ar GAS	3.0 (15.0)	95.5	604	2.8×10^{12}
N_2 GAS	2.05 (15.0)	65.3	345	1.6×10^{12}
CO_2 GAS	2.4 (15.0)	76.4	506	1.9×10^{12}
Cs VAPOUR	1.75 (13.0)	55.7	642	3.0×10^{12}
Rb VAPOUR	2.0 (13.0)	63.7	589	2.8×10^{12}
O_2 GAS	2.7 (15.0)	85.9	486	2.3×10^{12}

proton, and the plasma density for various gases and metal vapors. High ion currents of 2-3 mA, high current densities of around 500 mA/cm^2, and plasma densities of 1-3x10^{12} cm^{-3} were obtained. It is considered that the magnetic field formed in the limited space in this ion source has a great influence on both the high efficient plasma production through the electron-cyclotron-resonance process and the optimized high-density ion extraction.

The plasma density of the ion source is extremely high. On the other hand, in general, microwave propagation is cutoff in a high-density plasma. The propagation of the microwave with the frequency of 2.45 GHz is cutoff in free space when the plasma density is more than 7.4x10^{10} cm^{-3}. In this ion source, however, high-density plasma of 10^{12} cm^{-3} order is produced by using the microwave with frequency of 2.45 GHz. Based on the simple theoretical model of the propagation of microwave in infinite, one dimensionally inhomogeneous and magnetized plasma, the right-hand circularly polarized wave (whistler wave) can propagate the magnetized plasma with the high magnetic field $\omega_{ce}/\omega > 1$, where ω_{ce} is the electron-cyclotron angular frequency and ω the microwave angular frequency[14]. The experimental results of this kind of wave absorption has been reported[15]. However, it is difficult to apply this theoretical model to this ion source, where the plasma production chamber is small. In this case, it is proper that one considers the skin effect of high-frequency wave on the plasma. The skin depth δ is expressed as follows[16]:

$$\delta = c/(\omega_p{}^2 - \omega^2)^{1/2}, \tag{2.4}$$

where c is the light velocity and ω_p the plasma angular frequency. When the plasma density and the microwave frequency are 1×10^{12} cm^{-3} and 2.45 GHz, respectively, ω_p and ω are equal to 5.65×10^{10} and 1.54×10^{10} rad/s, respectively. δ is calculated at 5.5 mm from Eq. (2.4). The microwave can be propagated through the plasma as far as the skin depth. The dimensions of the plasma production chamber are 16 mm in diameter and 5 mm in height. The microwave power can be absorbed and contributes to the high-density plasma production. The ion source was made extremely small and compact by using a permanent magnet, and this compactness enables one to produce a high-density plasma by the microwave with the frequency of 2.45 GHz.

The reflection ratio of microwave power was about 30 % when Ar, N_2, CO_2, and O_2 gases were used, and the reflection ratio was 35-40 % when Cs and Rb metal vapors were used. It seems that microwaves were reflected since the plasma production chamber was not a resonant structure. However, it is difficult to match a plasma with an input microwave in the all-operation range because the dielectric constant of the plasma varies with the plasma density. In this ion source, the microwave is utilized not to heat the plasma electron excessively but to produce the plasma with singly charged ions. Therefore, the neutral gas or the plasma in the plasma production chamber can be regarded as a load for the microwave. The microwave is well absorbed, even if the plasma production chamber with nonresonant cavity structure is used. The reflected microwave power was less than 20 W. The microwave reflection hardly influences the ion source operation. The reflected microwave need not always be isolated by the

circulator. The nonresonant cavity structure of the plasma production chamber and the input system of the microwave by the antenna made the dimensions of the plasma production chamber extremely small and compact. This compactness also enables one to produce a high-density plasma by a relatively low-input microwave power.

One of the characteristics of this ion source is that the operational gas pressure is relatively low. The high electric field is concentrated in the gap between the sharp edge of the horizontal part of the antenna and the wall of the plasma production chamber. The gap discharge of this region contributes to maintain the stability of the microwave discharge under the low gas pressure. In the conventional high-frequency ion sources, the operational gas pressure is relatively high and it is not easy to cause an initial discharge. In this ion source, however, by making the plasma production chamber small and alternating the shape of the antenna, a stable microwave discharge occurs and is maintained under the low gas pressure.

The magnetic field strength and configuration should be adjusted more carefully and set in optimum condition. In a preliminary experiment where the external magnetic field by a solenoid was applied parallel to the axial magnetic field of the microwave ion source, the extracted Ar^+ ion current was increased by about 30 % with an increase by 20 % in the central magnetic field strength. The resonance region of the ECR might be varied so that the plasma could be generated more efficiently, or the ion extraction characteristics might be improved by the change of the magnetic field configuration. The adjustment of the magnetic
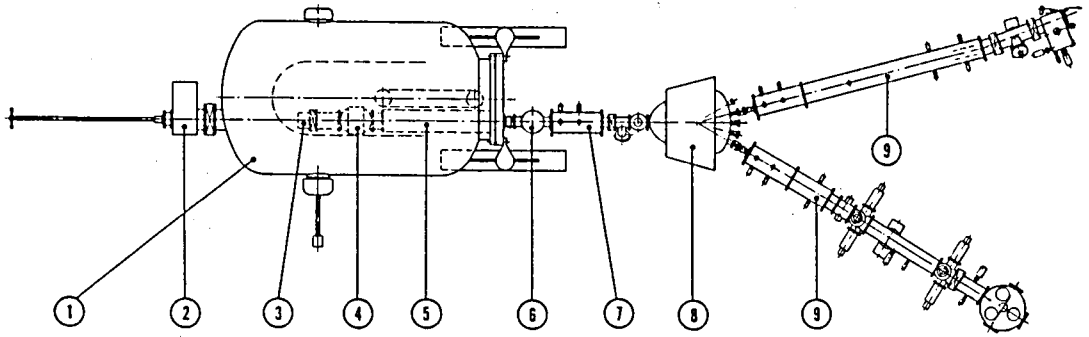
1. Pressure vessel
2. Ion source exchange system
3. Ion source
4. Wien filter
5. Accelerator tube
6. Vacuum pump
7. Quadrupole lens
8. Switching/Analyzing magnet
9. Beamline

(a)
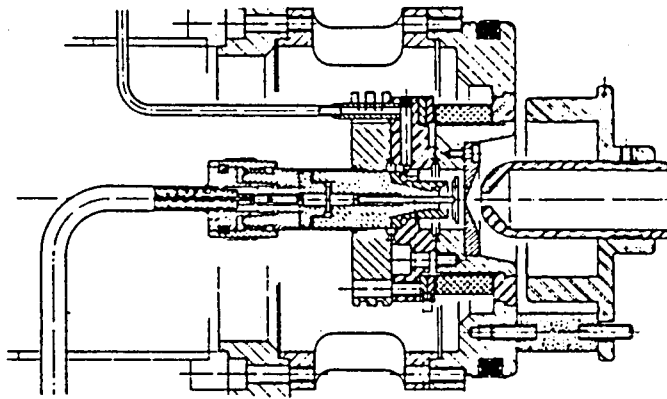
(b)

Fig. 2.21 (a) Megavolt implantation system based
on a Van de Graaff generator, and (b) microwave
ion source used in the system[18].

field strength and configuration is an important issue to be solved.

This compact microwave ion source is extremely useful for wide range of applications. For an example, this microwave ion source is used as an ion source in a megavolt implantation system based on a Van de Graaff generator[17]. The megavolt implantation system and the microwave ion source used in the system are shown in Figs. 2.21 (a) and (b), respectively[18]. The microwave ion source seems ideal for this megavolt implanter, because of its characteristics such as low power consumption, high current output, high brightness, long life-time, no filament and, most important in this case, simple and little maintenance and a simple and compact power supply. Another example is the simultaneous use of the microwave ion source for film formation with ionized cluster beam (ICB) deposition, vacuum deposition, and so on. Figure 2.22 shows the equipment for the simultaneous method using an ICB system and a microwave ion source[19]. In this method, dual beams consisting of a cluster beam and a gas ion beam are transported to form compound films such as oxide, nitride and carbide films. The microwave ion source is used for production of reactive ion beams, which works fairly well due to its compactness, high current density, and stable and long-period operation for reactive gases.

2.7 Summary

A new type of microwave ion source which has an axial magnetic field generated by a permanent magnet was developed for
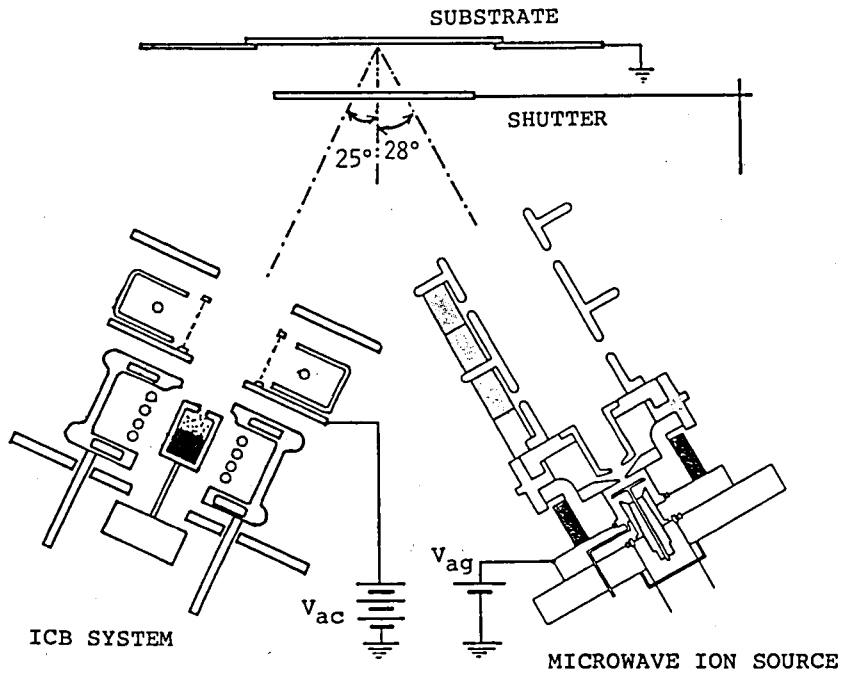
Fig. 2.22   Equipment for the simultaneous method
using an ICB system and a microwave ion source[19].
The microwave ion source is used for production of
reactive ion beams.

the primary alkaline plasma ion source of the intense heavy negative-ion source, NIABNIS. Since this microwave ion source has superior characteristics, the detailed features were described generally. By the combination of the permanent magnet and ferromagnetic materials, a closed magnetic circuit is formed through an ion extraction electrode. This axial magnetic field is utilized both for the high-density plasma production by the electron-cyclotron-resonance process and for the high efficient ion extraction by transporting the generated ions along the magnetic force lines. The continuous ion beams of 2-3 mA are delivered from the extraction aperture (2 mm in diameter) when various gases (Ar, N_2, CO_2), metal vapors (Cs, Rb), and reactive gas (O_2) are used. Extremely low impurities are present in the extracted ion beam. An ion beam with low emittance of 10^{-8} m·rad order and high brightness of 10^{11} A·m^{-2}·rad^{-2} order is obtained. The size of this ion source is 50 mm in diameter and 65 mm in height. The discharge power of the microwave with the frequency of 2.45 GHz is 7 to 30 W. Thus, a high-current microwave ion source with compact structure and low power consumption is realized.

This microwave ion source is fitted to the primary alkaline plasma ion source of the NIABNIS, because of its high current density, well-controlled source operation, compact structure and low power consumption. Moreover, it is used as an ion source in a megavolt implantation system and as a reactive ion source in a simultaneous method with an ICB system for film formation, in practice.

References (Chapter 2)

1) N.Sakudo, K.Tokiguchi, H.Koike, and I.Kanomata, Rev. Sci. Instrum. **48**, 762 (1977).

2) N.Sakudo, K.Tokiguchi, H.Koike, and I.Kanomata, Inst. Phys. Conf. Ser. No.54, (1980), p.36.

3) R.Geller, IEEE Trans. Nucl. Sci. **NS-23**, 904 (1976).

4) K.Bernhardi, G.Fuchs, M.A.Goldman, H.C.Herbert, W.Walcher, and K.Wiesemann, IEEE Trans. Nucl. Sci. **NS-23**, 999 (1976).

5) L.Valyi, Atom and Ion Sources (Wiley, New York, 1977), p.193.

6) J.Ishikawa, Y.Takeiri, and T.Takagi, Rev. Sci. Instrum. 55, 449 (1984).

7) J.Ishikawa, Y.Takeiri, and T.Takagi, Proceedings of the International Ion Engineering Congress, Kyoto (Institute of Electrical Engineers of Japan, Tokyo, 1983), p.379.

8) J.Ishikawa, Y.Takeiri, and T.Takagi, Proceedings of the Sixth Symposium on Ion Sources and Ion-Assisted Technology, Tokyo (The Research Group of Ion Engineering, Kyoto University, 1982), p.25.

9) A.von Engel, Ionized Gases (Oxford University, Oxford, 1965), p.31.

10) T.S.Green, IEEE Trans. Nucl. Sci. **NS-23**, 918 (1976).

11) Focusing of Charged Particles, edited by A.Septier (Academic, New York, 1967), p.150.

12) P.M.Lapostolle, IEEE Trans. Nucl. Sci. **NS-18**, 1101 (1971).

13) A.van Steenbergen, IEEE Trans. Nucl. Sci. **NS-12**, 746 (1965).

14) T.H.Stix, The Theory of Plasma Waves (McGraw-Hill, New York, 1962), p.27.

15) J.Musil, F.Žáček, and P.Schmiedberger, Plasma Phys. **16**, 735 (1974).

16) F.F.Chen, Introduction to Plasma Physics (Plenum, New York, 1974), p.103.

17) J.Ishikawa, S.Douma, W.Urbanus, S.Doorn, J.Bannenberg and F.Saris, Proceedings of the Tenth Symposium on Ion Sources and Ion-Assisted Technology, Tokyo (The Research Group of Ion Engineering, Kyoto University, 1986), p.105.

18) Commercial catalogue for 'Megavolt implantation systems', High Voltage Engineering Europa B.V..

19) K.Fujime, T.Ueda, H.Takaoka, J.Ishikawa, and T.Takagi, Proceedings of the International Workshop on Ionized Cluster Beam Technique, Tokyo (The Research Group of Ion Engineering, Kyoto University, 1986), p.195.

Chapter 3

NEUTRAL- AND IONIZED-ALKALINE METAL BOMBARDMENT-TYPE

HEAVY NEGATIVE-ION SOURCE

3.1 Introduction

Metal sputtering by alkaline metal ions is a potential method of producing heavy negative ions[1]. When negative ions are produced by sputtering, it is essential that the work function of the sputtering target surface should be kept low and, at the same time, sputtered metal atoms should be generated with a high yield. As heavy negative-ion sources, the universal negative ion source (UNIS)[2,3] and the Aarhus negative ion source (ANIS)[4,5] have been studied by many authors[6-12]. In UNIS, the advantage is that the sputtering efficiency is quite high because cesium ion particles are accelerated at a high energy before the sputtering target is bombarded with them. Thus, this ion source is suited for low sputtering yield targets. However, it has the disadvantage that the size of the ion source is large since the surface ionization cesium ion source components, the main electrodes such as the ion extraction electrode and lens system, the sputtering target, and the negative ion extraction system, are installed separately. The quantity of neutral cesium particles proceeding toward the sputtering target from the cesium ion source is quite small. This is because the surface

ionization ion source, in general, can hardly emit neutral cesium particles, and the cesium ion source and the sputtering target are separated by several electrodes. Spraying neutral cesium particles onto the sputtering target is necessary since the cesium particles on the sputtering target surface are insufficient for high sputtering yields or high-temperature sputtering targets. On the other hand, ANIS employs a means for negative ion production in which the target is placed in the plasma production chamber and cesium vapor is sprayed onto the target. Negative ions are directly extracted from the plasma production chamber. For this apparatus, the advantages are that the size of the ion source is small and that a sufficient supply of neutral cesium particles is present on the surface of the sputtering target since the sputtering target is placed in the cesium plasma production chamber. This ion source is suited for high sputtering yield targets. However, ANIS has the disadvantage that it cannot sufficiently accelerate cesium ion particles and this reduces the sputtering efficiency. Another disadvantage is that the number of negative ions which may be extracted is decreased because some of the generated negative ions are destroyed during passage through the plasma.

To overcome these disadvantages in UNIS and ANIS a neutral- and ionized-alkaline-metal bombardment-type heavy negative-ion source (NIABNIS) was developed[13-15]. In this ion source, since high current and high energy alkaline ions are extracted from a plasma ion source and a sputtering target is directly attached to the ion extraction electrode of the plasma ion source, sufficient neutral alkaline particles are present on the target surface and

the loss of the alkaline ion current during the beam transport will be reduced. The alkaline plasma ion source is an axial magnetic field extraction-type microwave ion source with a permanent magnet, which can provide simultaneously a high current alkaline ion beam with high energy and sufficient neutral alkaline particles. Thus, a low work function of the metal target surface and a high current alkaline ion bombardment can be achieved. The negative ion source, moreover, can be designed to be small in size. In this chapter, after the key parameters to increase the negative ion yields are discussed theoretically, the structure of the NIABNIS and the operational characteristics are described in detail.

3.2 Theoretical Background on Heavy Negative-Ion Production by Sputtering

3.2.1 Secondary negative-ion emission

Negative ion production efficiency is relatively high when an atom leaves a metal surface with a quite higher velocity than a thermal velocity. This phenomenon, that is called the secondary negative-ion emission, is used for sputter- or reflection-type negative ion sources. Many theoretical models for the secondary negative-ion emission have been reported, and they are classified into two groups: the thermodynamic model and the surface effect model.

In the thermodynamic model, although the secondary negative-ion emission process, where particles are emitted with a higher velocity than a thermal velocity, is basically non-thermodynamic

equilibrium, the system is assumed to be in thermodynamic equilibrium, and the surface ionization theory is applied to the estimation of the negative ion production efficiency. Two different models have been proposed. In the first model, it is assumed that a negative ion is emitted locally in thermodynamic equilibrium from the metal surface at an extremely high temperature. Thus, the ratio of negative ions to neutral particles in emitted particles is given by

$$\alpha_i = K \exp(E_a/kT), \qquad (3.1)$$

where T is the local thermodynamic equilibrium temperature, E_a the electron affinity of the negative ion, k the Boltzmann's constant and K the coefficient related to the electron density and the statistical weighting factors[16,17]. In the other model, it is assumed that the negative ion production efficiency is determined only by the difference between the work function of metal surface and the electron affinity of an atom. Thus, the negative ion production probability is the same equation as that for the surface ionization, and is given by

$$I_i = A \exp[(E_a+(qE/4\pi\epsilon_0)^{1/2}-\varphi)/kT], \qquad (3.2)$$

where T is the temperature of the metal surface, q the electron charge, E the external electric field, ϵ_0 the dielectric constant and φ the work function of the metal surface[9,18]. $(qE/4\pi\epsilon_0)^{1/2}$ is the Schottky term which arises from the fact that the image force is increased by the presence of the external electric field, E. A is the coefficient related to the emitted particle flux.

On the other hand, in the surface effect model the velocity of the emitted particle is considered to be a main factor for the

negative ion production. In this case there are two models according to the charge state of the emitted particle just on the metal surface, that is, neutral or negative. In the ion production-type model the initial charge state of the emitted particle is neutral, and there exists a probability that the emitted neutral particle turns into a negative ion during the path from the surface to the infinity through a quantum interaction. When a particle is emitted from a metal surface with a velocity much larger than a thermal velocity, a quantum interaction between the electron affinity level in the atom and the electron energy level in the metal surface results in the negative ion production in a certain probability. Various approximate analyses have been performed, and these results are a little different from each other according to the models or analyzing methods. The negative ion production probability is expressed in general as follows:

$$R^- = Bv_\perp^m/(\varphi - E_a)^n, \qquad\qquad (3.3)$$

where $v_\perp$ is the velocity component normal to the metal surface and B is the coefficient[19-22]. According to the models or analyzing methods, m and n are (i) $m=n=3$[20], (ii) $m=1/2$, $n=-1/2$[20], and (iii) $m=n=1$[21,22]. On the other hand, in the neutralization-type model the initial charge state of the emitted particle is negative, and there exists a probability that the emitted negative ion survives without being neutralized to the infinity. In this model it is assumed that most of particles become negative ions in the range of distance $0 < x < R_0$ (x: the distance from the metal surface and R_0: a critical distance defined later), and, then, the probability that an electron in

63

the negative ion shifts to the metal surface in the range of distance $x > R_0$ is calculated. As a result, the quantity of the negative ions which finally survive in the negative state can be estimated[23,24]. The potential barrier against an electron of the metal is lowered by the mirror image force near the metal surface. In the region where the energy level of the electron affinity in an atom is lower than the Fermi energy level in the metal, the electron in the metal can easily shift to the electron affinity level in the atom by tunneling. Thus, R_0 is the critical distance where the energy level of the electron affinity in the atom is equal to the Fermi energy level in the metal, i.e., where the regions of production and destruction of negative ions are distinguished. R_0 is approximated as

$$R_0 \cong e^2 / [4 \pi \epsilon_0 (\varphi - E_a)], \tag{3.4}$$

corresponding to a few times the atomic radius. The probability that the particles which are all emitted in negative state from the distance R_0 survive as negative ions at the infinity is given by Kishinevskii[24], using atomic units.

$$\beta^- = \exp[-(B^2 \Gamma^2 (1-\lambda)/2v_\perp R_0)(\varphi/U_0)^{1/2}$$
$$\cdot e^{-1/2\gamma} (R_0/2\lambda)^2 \lambda e^{-2\gamma R_0}],$$
$$R_0 = 1/[4(\varphi - E_a)], \quad \lambda = 1/[4(2\varphi)^{1/2}],$$
$$\gamma^2/2 = E_a, \tag{3.5}$$

where U_0 is the energy difference between the bottom of the conduction band of the metal and the vacuum level, Γ the gamma function and B the coefficient related to the amplitude of the wave function. From Eq. (3.5) it is found that the negative ion survival probability β^- tends to be increased as $v_\perp$ is increased and φ is decreased. Rasser et al. have introduced a fairly

simple equation giving the negative ion production probability which is applied to the case of the emitted ion with a low velocity. The equation is expressed as follows:

$$\beta^- \cong (2/\pi)\ \exp[-\pi(\varphi - E_a)/2av_\perp],$$ (3.6)

where a is the constant[22].

From these models the negative ion production efficiency is found to be increased as (i) the work function of the metal surface is decreased, (ii) the velocity of the emitted particle is increased and (iii) the electron affinity of the atom is increased. However, since the electron affinity is an inherent value of an atom and, in sputtering, particles are emitted with an average energy of the binding energy[25], these values cannot be intentionally changed. Thus, in the sputter negative-ion sources, in practice, the negative ion production efficiency could be enhanced by lowering the work function of the metal surface. Of course, by increasing the amount of the emitted particles through the sputtering process, the negative ion yield could be increased.

3.2.2 Sputtering

There are three mechanisms that the secondary particles are emitted at a higher velocity than a thermal velocity from the metal surface: reflection of an incident light particle such as hydrogen, emission of an adsorbed light atom such as lithium by bombardment of the other atom with a high energy, and emission of a sputtered metal atom by bombardment of the primary heavy atom with a high energy. In this sub-section, the sputtering process, which is important to the sputter heavy negative-ion source, is

briefly discussed.

For the negative ion production, the important factors in the sputtering process[25] are sputtering ratio, angular distribution of sputtered particles, dependency of sputtering ratio on incident angle of a primary ion, and energy distribution of sputtered particles. The sputtering ratio S is expressed in Thompson's model[26] by

$$S = (\pi^2 a_0^2 N^{2/3}/8e)(E_R/E_B)$$
$$\cdot (M_1(Z_1 Z_2)^{5/6}/(M_1+M_2))\sec\theta, \qquad (3.7)$$

where E_R is the Rydberg energy (13.6 eV), E_B the surface binding energy which is considered to be nearly the same as the sublimation energy, a_0 the Bohr radius (0.53 Å), N the atomic density of metal, and θ the incident angle. Subscripts 1 and 2 indicate the incident particle and the target (metal) particle, respectively. In Sigmund's model[27] the sputtering ratio S is expressed by

$$S = (3/4\pi^2)(\alpha(M_2/M_1)S_n(E))/C_0 U_0), \qquad (3.8)$$

where U_0 is the sublimation energy, C_0 the coefficient related to the metal target, $S_n(E)$ the stopping cross section for substitution, and $\alpha(M_2/M_1)$ the efficiency of energy transfer.

In practice the sputtering ratio has a stronger dependence on combination of the incident element and the target element than that predicted by the models. The sputtering ratio also has a strong dependence on the incident particle energy and shows a maximum value at a certain incident energy. The incident energy giving a maximum sputtering ratio is several tens of keV in the case where cesium ions sputter target metal. Although the sputtering ratio has a $\sec\theta$ dependence on the incident angle

66

Table 3.1   Sputtering yield for various metals[28].
The values in the parentheses are calculated by
the modified Sigmund theory.

	Xe^+ ION BOMBARDMENT					
	1 keV		10 keV		20 keV	
Be	0.60	(0.42)	1.7	(1.2)	2.1	(1.5)
B		(0.29)		(1.0)		
C	0.15	(0.20)	0.36	(0.83)	0.44	(1.0)
Al	1.2	(1.3)	3.4	(3.5)	4.3	(4.5)
Si	0.75	(0.90)	2.4	(2.7)	3.0	(3.3)
Ti	0.72	(1.2)	2.1	(4.0)	2.8	(4.8)
V	0.93	(1.2)	2.7	(3.8)	3.2	(4.5)
Cr	2.2	(1.7)	6.2	(4.9)	8.1	(6.1)
Mn		(2.6)		(6.2)		(9.0)
Fe	2.0	(1.7)	5.8	(5.0)	7.1	(6.1)
Co	1.6	(1.6)	5.0	(5.0)	6.1	(6.2)
Ni	1.7	(1.7)	5.1	(5.1)	6.3	(6.3)
Cu	3.6	(2.2)	10	(6.8)	12	(8.2)
Ge	1.5	(2.2)	4.2	(6.4)	5.2	(7.1)
Zr	0.87	(1.5)	2.5	(4.6)	3.1	(5.8)
Nb	1.3	(1.2)	4.9	(3.8)	6.1	(4.8)
Mo	1.3	(1.3)	4.0	(4.2)	5.0	(5.2)
Ru	1.9	(1.4)	5.7	(4.5)	7.0	(5.8)
Rh	2.1	(1.8)	6.1	(5.2)	8.0	(6.8)
Pd	3.1	(3.0)	8.9	(8.2)	11	(10)
Ag	6.1	(4.0)	18	(11)	22	(13)
Sn		(4.0)		(11)		(13)
Hf	1.6	(2.1)	5.2	(6.4)	7.0	(8.1)
Ta	1.3	(1.5)	4.1	(5.0)	5.1	(6.2)
W	1.9	(1.4)	5.7	(4.7)	7.0	(6.0)
Re	1.9	(1.6)	5.9	(5.0)	7.5	(6.3)
Os	2.0	(1.6)	6.2	(5.1)	8.1	(6.4)
Ir	2.3	(2.0)	7.2	(6.0)	9.8	(8.0)
Pt	2.9	(2.3)	9.0	(7.2)	11	(9.2)
Au	7.0	(4.0)	21	(12)	28	(15)
Th	1.6	(2.5)	5.0	(7.8)	6.2	(10)
U	1.3	(2.9)	4.6	(8.7)	6.0	(11)

from Eq. (3.7), the sputtering ratio shows a maximum value at the incident angle of 50-80° in practice[25]. The angular distribution of sputtered particles is nearly cosine distribution.

The energy distribution of sputtered particles is approximated as follows:

$$N(E) = CE/(E+E_B)^n, \qquad\qquad (3.9)$$

where n is the constant of 2 - 3[20]. The energy distribution shows a peak when $E=E_B$ or $E=E_B/2$. Thus, the energy of the sputtered particles cannot be changed intentionally.

Table 3.1 lists the sputtering ratios for various metal targets by 1, 10 and 20 keV Xe^+ ion bombardments[28].

3.2.3 Surface work function

The work function of the metal surface is a key factor in negative ion production, as discussed in sub-section 3.2.1. In the thermodynamic model, the negative ion production probability is proportional to $\exp[-(\varphi-E_a)/kT]$ from Eq. (3.2). On the other hand, in the model of neutralization by the surface effect, the negative ion production probability is proportional to $\exp[-(\varphi-E_a)/v_\perp]$ from Eq. (3.6). The electron affinity is an inherent value for elements, and the velocity of the emitted particle is almost corresponds to the surface binding energy. Thus, these theories indicate the importance of the low work function of the target surface for efficient negative ion production.

Although cesium has the lowest work function of 1.81 eV in the all elements, the work function of the cesium-covered surface is generally lower than that of the bulk cesium[29-33]. The
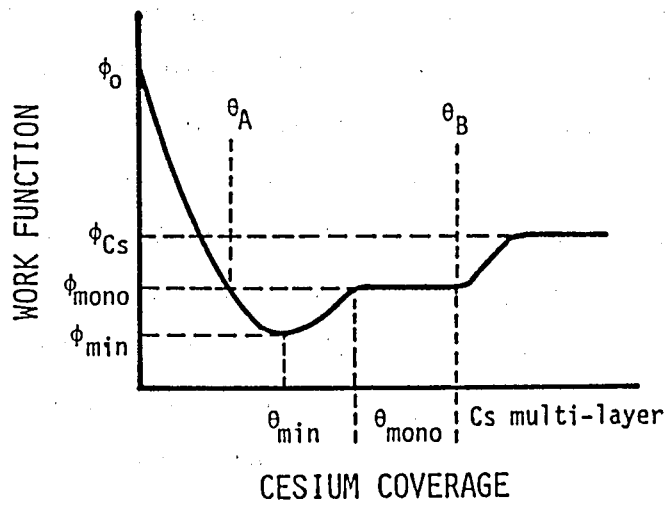
Fig. 3.1   Schematic diagram of work function
dependence on cesium coverage.

general behavior of the surface work function as a function of the cesium coverage is illustrated in Fig. 3.1. The work function of the base metal substrate is φ_0. The surface work function decreases with an increase in the cesium coverage and reaches a minimum value φ_{min} at the coverage θ_{min}. Then, it increases with an increase in the cesium coverage until a value φ_{mono} at the cesium monoatomic layer θ_{mono}. Since no further cesium atoms stick to the surface above around the room temperature due to the weak Cs-Cs binding energy, no further change in the surface work function is usually observed. When the target is cooled (for example, to 77 K), the cesium multilayer can be formed. In this case the work function is changed at a value φ_{Cs} on the cesium multilayer, i.e.; the bulk cesium work function. Tables 3.2 (a) and (b) show the measured values of φ_{min} and φ_{mono} for some polycrystalline metal surfaces and for some single crystal metal faces covered by cesium, respectively[32]. Table 3.3 shows the representative values of θ_{min} and θ_{mono} for some single crystal metal faces[32]. In this case the cesium coverage is defined as $\theta_a = N_a/N_s$, where N_a and N_s are the number of atoms per unit area of the absorbate and the first layer of the substrate, respectively.

Since a lower work function of the sputtering target makes the negative ion production efficiency higher, the region of cesium coverage for the high efficient negative ion production is between θ_A and θ_B as shown in Fig. 3.1. Excessive cooling of the sputtering target may lead to formation of thicker cesium layers on the target surface than θ_B. This lowers the sputtering yield of the target material. On the other hand,

Table 3.2   Minimum and monolayer work function
values for cesium coverage of (a) polycrystalline
substrates and (b) single crystal faces[32].

Substrate	φ_{min} (eV)	φ_{mono} (eV)
Cu	1.64	1.64
Mo	1.54	1.82
	1.61	1.77
Ni	1.37	1.80
Re	1.45	1.77
	1.51	1.56
Ta	1.69	1.70
W	1.52	1.80
	1.60	1.64
SUS304	1.52	1.60

(a)

Substrate	φ_{min} (eV)	φ_{mono} (eV)
Cu(100)	1.65	2.07
Cu(111)	1.60	2.00
Mo(110)	1.60	2.10
Ni(100)	1.60	2.00
Ta(110)	1.76	2.00
W(100)	1.6	1.78
W(110)	1.45	2.15
W(111)	1.57	1.80
W(112)	1.57	1.85
Re(10T1)	1.48	
Re(2T00)	1.55	
Re(2T11)	1.60	
Re(2T12)	1.53	

(b)

Table 3.3   Representative cesium coverages
corresponding to the minimum work function and
the cesium monolayer[32].

Substrate	θ_{min}	θ_{mono}
W(100)	0.25	0.43
W(110)	0.23	0.6
W(112)	0.5	0.75
Cu(111)	0.14	0.25

shortage of cesium atoms on the sputtering target surface corresponding to the cesium coverage below θ_A is caused by the two situations: a high temperature of the sputtering target and a target material with a high sputtering yield. A high temperature of the sputtering target causes destruction of the cesium monolayer of the target surface. The critical temperature where the cesium monolayer starts desorption is related with the binding energy between target material and cesium. It is reported that in the case of the carbon sputtering target the critical temperature is around 600 $^{\circ}$C[34]. A high sputtering yield of the sputtering target also causes shortage of the cesium atoms on the surface. The sputtering ratios listed in Table 3.1 are considered to be nearly the same as the sputtering ratios by Cs^+ ion bombardment because the mass difference between Xe and Cs is only one. The sputtering ratios for most of the metals at high incident energy are over a few atoms/ion. In these cases the cesium atoms adsorbed on the sputtering target surface tend to be stripped off with the sputtered metal particles. As a result, the surface cesium atom density is much lower than that of monolayer, and the surface work function becomes very high.

From the above-mentioned discussion, it is found that the control of the target temperature and the additional neutral cesium supply are necessary to keep the surface work function as low as possible.

3.3 Operating Principle and Source Construction

Low surface work function and high sputtering yield are

essential to an intense heavy negative-ion beam production as described in the previous section. In this section, the operating principle and source construction of a newly developed intense heavy negative-ion source, NIABNIS, are described.

3.3.1 Operating principle

Figure 3.2 shows the operating principle of the neutral- and ionized-alkaline-metal bombardment-type heavy negative-ion source (NIABNIS). The source consists of an alkaline plasma ion source, a suppressor, a target electrode, and a negative ion extraction electrode arranged in this order. Neutral alkaline particles are supplied to the plasma production chamber from an alkaline metal oven. A part of the alkaline particles are ionized in the plasma production chamber. The ionized alkaline particles are extracted from the ion extraction aperture and accelerated by the suppressor electrode, and then bombard the sputtering target. A part of the alkaline ions which pass through the aperture of the sputtering target, proceed and are distributed in the negative ion extraction region. At the same time, sufficient neutral alkaline particles that have not been ionized are also ejected from the ion extraction aperture toward the positive ion extraction electrode system.

By attaching the sputtering target directly to the alkaline ion extraction electrode system, the ionized particles are incident on the sputtering target as soon as they are extracted. Thus, the high energy alkaline ion beam together with the low energy neutral alkaline beam are incident on it with a minimum loss of the ionized- and neutral-alkaline-metal beams. The
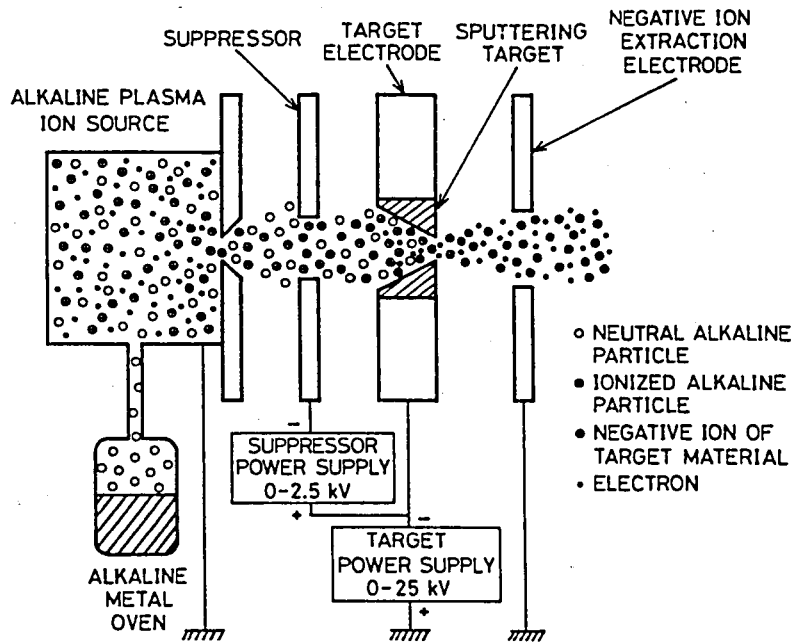
74

Fig. 3.2   Illustration of the operating principle
of the neutral- and ionized-alkaline-metal
bombardment-type heavy negative-ion source
(NIABNIS).

optimal amount of the alkaline particle coverage on the sputtering target surface is maintained. As shown in Fig. 3.2, the alkaline ion extraction electrode system is an accelerating-decelerating system. The sputtering target is attached to the decelerating electrode which is called the target electrode. The accelerating electrode, which is called the suppressor, is negatively biased against the target electrode. This potential prevents the secondary electrons from returning to the alkaline plasma ion source. The damage to the alkaline ion source by the backward secondary electrons and negative ions is avoided. The sputtering target, the inside of which is bombarded with neutral and ionized particles, has an open end. The negative ions are extracted from the open end and led to the right in Fig. 3.2 by the negative ion extraction electrode, and then accelerated and mass-separated.

3.3.2 Source construction

The alkaline plasma ion source in this negative ion source serves as a means for supplying both high energy ionized alkaline particles and low energy neutral alkaline particles. The axial magnetic field extraction-type microwave ion source, described in the previous chapter, was used as the alkaline plasma ion source and enabled one to control the amount of neutral and ionized particles. In these experiments cesium was used as the alkaline metal.

Figure 3.3 shows the construction of the NIABNIS with the axial magnetic field extraction-type microwave ion source with a permanent magnet. As shown in the previous chapter, the
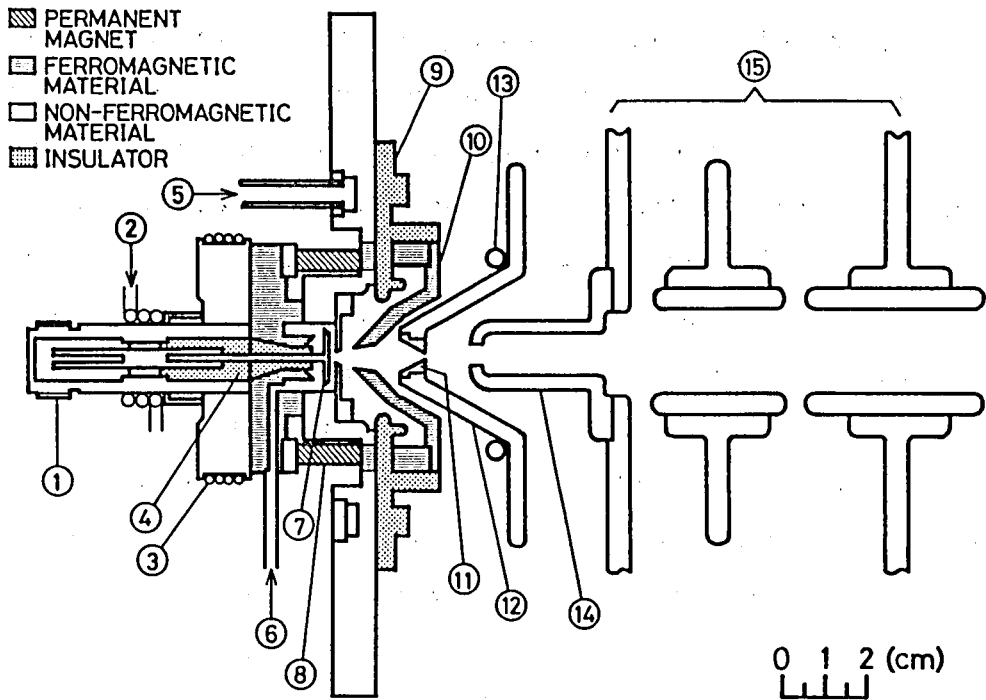
Fig. 3.3 Construction of the NIABNIS with the axial magnetic field extraction-type microwave ion source with a permanent magnet. (1) Sealed coaxial connector, (2) coolant, (3) sheath-heater, (4) boron nitride, (5) coolant, (6) cesium vapor, (7) antenna, (8) permanent magnet, (9) ceramic insulator, (10) suppressor, (11) sputtering target, (12) target electrode, (13) cooling tube, (14) negative ion extraction electrode, and (15) einzel lens.

microwave ion source is compact and consumes only a very low power. Cesium vapor from an oven is fed to the plasma production chamber, and efficiently discharged. The cesium flux ratio of ionized to neutral particles is controlled to some extent by adjusting the cesium oven temperature and the input microwave power. A few mA of cesium ion beam can be obtained. The target electrode is made of copper. A wound copper cooling tube in which the coolant is introduced is silver-soldered on the target electrode. Various coolants such as air, liquid carbon dioxide, and liquid nitrogen are used. The temperature of the target electrode is controllable from liquid nitrogen temperature to a high temperature. The sputtering target can be maintained at an appropriate temperature for highly efficient negative ion production.

The sputtering target, which is attached to the target electrode, is shown in Fig. 3.4. The inside shape of the sputtering target is conical where the incident angle of the cesium ion beam on the sputtering target surface is about 60°. The produced negative ions are extracted from the end aperture of the target. Although most of the sputtering targets of solid materials are easy to shape with a lathe, the sputtering targets of hard and brittle materials such as silicon and boron are fabricated by a supersonic vibrational shaper with diamond paste.

The suppressor is negatively biased by up to -2.5 kV against the target electrode. The C^- ion current and the target current as a function of the suppressor voltage are shown in Fig. 3.5. The target current rapidly decreased when the suppressor voltage was between 0 and 250 V. The C^- current was constant when the
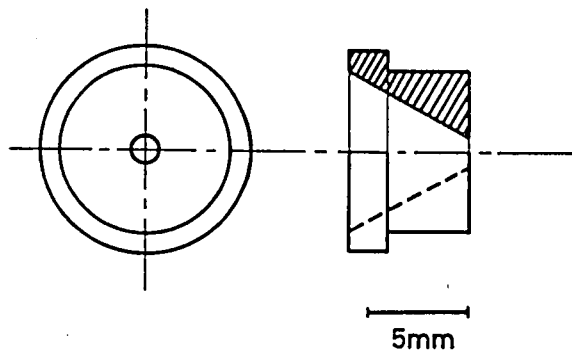
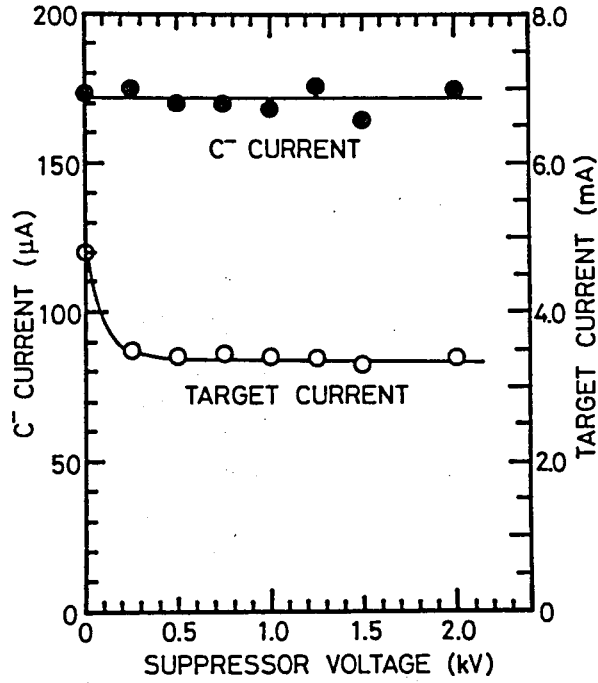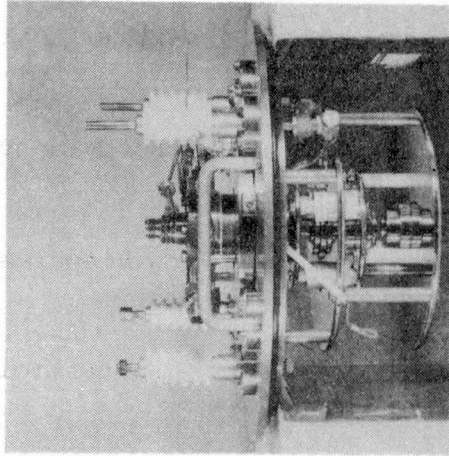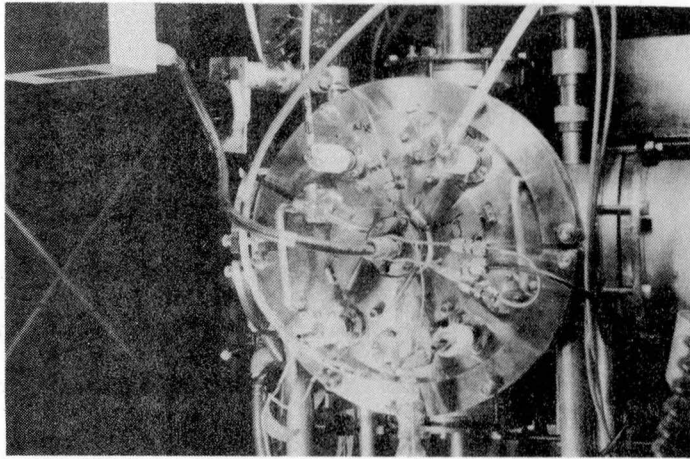Fig. 3.4   Drawing of the sputtering target.

Fig. 3.5   C⁻ ion current and the target current as
a function of the suppressor voltage.   ● the C⁻
current, and ○ the target current.   The cesium
ion beam energy is 19.0 keV.

(a)

(b)

Fig. 3.6   (a) Photograph of the side view of the
NIABNIS and (b) photograph of the NIABNIS in
operation.

suppressor voltage was varied. These results show that the suppressor suppresses the secondary electrons to the cesium ion source but scarcely affects the negative ion extraction efficiency.

Figures 3.6 (a) and (b) show photographs of the NIABNIS.

3.4 Neutral and Ionized Particle Trajectories

Both neutral and ionized cesium particles emitted from the extraction aperture contribute to negative ion production by bombarding the sputtering target. The ionized cesium particles need trajectories which lead to a high sputtering yield when bombarding. The neutral cesium particles must be adsorbed on the sputtering target in order to prevent an increase of the surface work function. Figure 3.7 shows the results of the simulation of the ionized cesium particle trajectories near the ion extraction region as shown in Fig. 3.3. The trajectories are simulated by use of the computer program which is shown in Appendix B. Through the extraction aperture of 2 mm in diameter, ions are extracted from the plasma with a plasma density of 3×10^{12} cm^{-3} and an electron temperature of 3 eV. The distance between the extraction aperture and the extraction electrode is 3 mm. The potentials of the plasma production chamber, the suppressor, and the target electrode are 0 V, -20.5 kV, and -20 kV, respectively. In this simulation the potential of the negative ion extraction electrode was not considered. As the ion emitting surface has a concave form, the ion beam trajectories near the ion extraction aperture are convergent. On the other hand, the ion beam

Fig. 3.7   Results of the simulation of the ionized
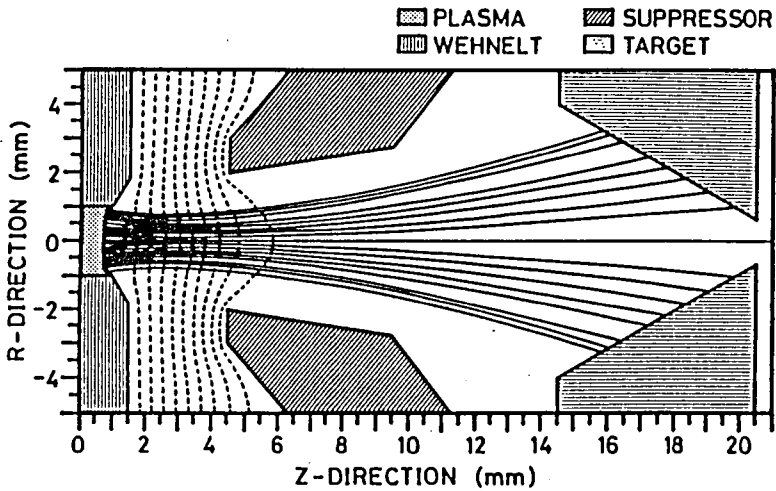cesium particle trajectories near the ion
extraction region.   Ions are extracted from the
plasma with a plasma density of 3×10^{12} cm^{-3} and an
electron temperature of 3 eV.   The potentials of
the plasma, the suppressor, and the target
electrode are 0 V, -20.5 kV, and -20 kV,
respectively.   The dotted lines indicate the
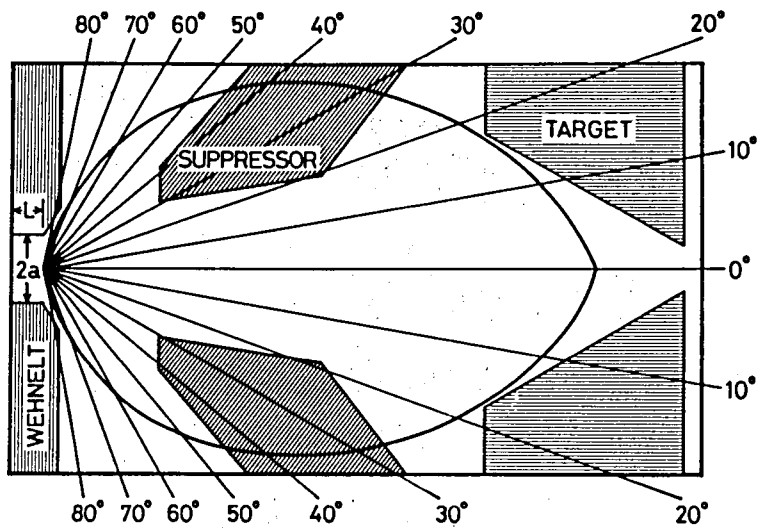equipotential lines of 2.05 kV unit.

Fig. 3.8   Polar diagram in the case where the
neutral cesium particles are emitted from the
aperture with an aspect ratio of 2 (=2a/L),
assuming that the cesium vapor pressure in the ion
extraction region is zero[35].

trajectories are slightly divergent near the sputtering target, because the high ion beam current of 1.35 mA causes an ion space-charge repulsion force in the beam. This adequately divergent beam can bombard a limited area of the sputtering target. The incident angle of the cesium ion beam on the sputtering target is around 60°, which results in a high sputtering yield. A part of the ions in the beam whose trajectories are present near the center axis, pass through the aperture of the sputtering target and enter the negative ion extraction region. Therefore, the space charge of the negative ions can be compensated by that of the positive cesium ions.

The quantity and shape of the neutral cesium flux emitted from the ion extraction aperture are determined by the neutral cesium vapor pressure in the plasma production chamber and the conductance of the aperture. Figure 3.8 shows the polar diagram in the case where the neutral cesium particles are emitted from the aperture with an aspect ratio of 2 (=2a/L), assuming that the cesium vapor pressure in the ion extraction region is zero[35]. The solid angle with which the sputtering target is seen from the ion extraction aperture is 0.34 sr. The quantity of the neutral cesium particles emitted from the ion extraction aperture within this solid angle is 22 % of the total amount of emitted neutral cesium particles. The quantity of the neutral cesium particles that reach the sputtering target surface is proportional to the cesium vapor pressure in the plasma production chamber. Therefore, this can be controlled by varying the cesium oven temperature.

3.5 Negative Ion Extraction Characteristics

The work function of the sputtering target surface is an important factor in negative ion production. Maintaining the work function as low as possible is essential to a high efficiency of negative ion production. In the case where cesium particles are present on the metal surface, a cesium surface with one half to one monolayer is adequate for the negative ion production. This is because the work function is lowest in this condition[29-31] and the cesium surface layer hardly prevents metal particle emission by sputtering. The sputtered surface is not always in this moderate state. The quantity of adsorbed cesium particles on the sputtering target surface is insufficient when a high sputtering yield material is used for the sputtering target or when the temperature of the sputtering target is exceedingly raised during sputtering.

On the other hand, the negative ion yield is increased with an increase in the sputtering yield which is proportional to the incident ion current. Thus, it is required that the incident cesium ion current to the sputtering target should be increased as much as possible, in order to obtain high current negative ion beams. In this section, the negative ion extraction characteristics are described from the points of view of the effect of cesium particle adsorption on the sputtering target surface and the dependency of the negative ion yields on the incident cesium currents.
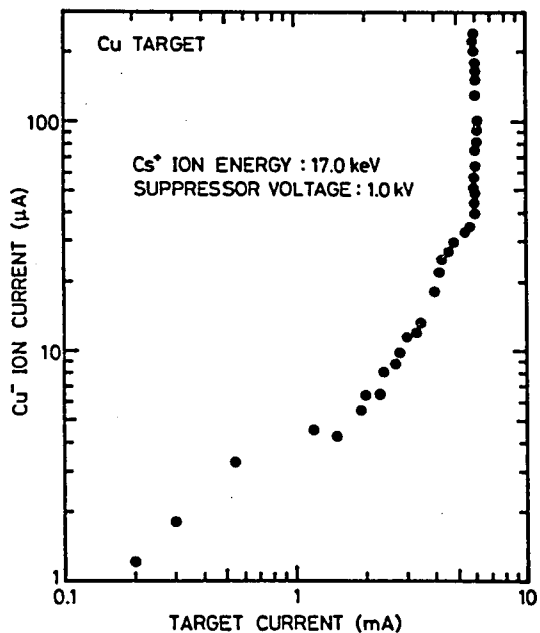
Fig. 3.9   Mass-separated Cu⁻ ion current as a
function of the target current in the case of a
copper sputtering target.   At the target current
of about 6 mA, only the cesium oven temperature
was increased without varying the input microwave
power.

3.5.1 Bombardment of neutral cesium particles

When a material with a high sputtering ratio is used as a sputtering target, the only ionized cesium particle bombardment of the target leads to sputtering of a large amount of cesium on the target surface together with the target material. As a result, the cesium coverage on the target surface is insufficient, and the work function of the surface is so high that the negative ion production efficiency is lowered. Thus, extra neutral cesium particles should be supplied to the target surface in order to lower the surface work function. In the NIABNIS the microwave plasma ion source is used as a cesium positive ion source. By controlling the cesium oven temperature the desired quantity of neutral cesium particles together with ionized cesium particles are emitted from the ion extraction aperture.

The Cu^- ion current as a function of the target current in the case of a copper sputtering target is shown in Fig. 3.9. The target current was increased up to 6 mA by controlling both the cesium oven temperature and the input microwave power, and then only the cesium oven temperature was increased at the target current of about 6 mA without varying the input microwave power. As shown in Fig. 3.9, the additional neutral cesium particle supply at the target current of 6 mA resulted in an increase in the Cu^- ion current by nearly an order of magnitude. On the other hand, in the region where the target current is below 6 mA, it is considered that the Cu^- ion current was increased mainly by an increase in the sputtering yields. Figure 3.10 shows the Cu^- ion current as a function of the cesium oven temperature at the
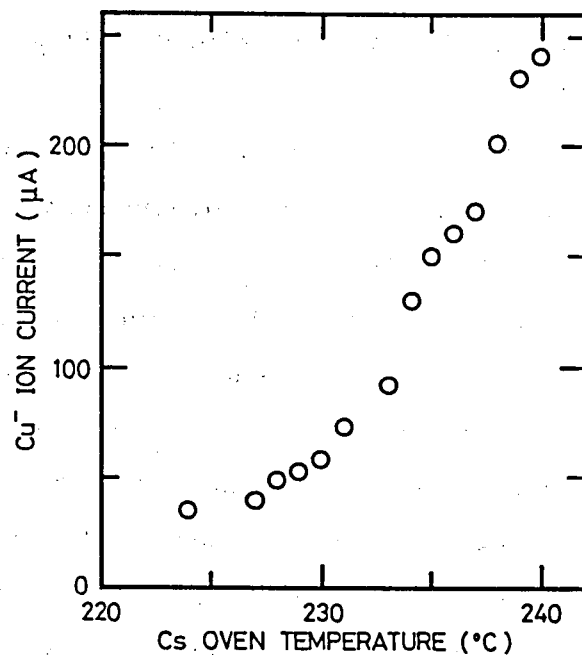
Fig. 3.10   Cu⁻ ion current as a function of the
cesium oven temperature for the neutral cesium
spray control.   The energy and current of the
positive cesium ion to the sputtering target were
17 keV and 3 mA, respectively.

target current of 5.7 to 6.2 mA in Fig. 3.9. Since copper has a high sputtering ratio, the additional neutral cesium particle supply made the negative ion production efficiency increase dramatically. Although an increment of the oven temperature was as small as 16 $^{\circ}$C, the negative ion production efficiency was increased by 7 times. In this experiment, 320 μA of the Cu^- ion current was obtained.

A sputtering ratio of aluminum is smaller than that of copper. However, its negative ion production characteristics were similar to the copper's. The Al^- ion current as a function of the cesium oven temperature is shown in Fig. 3.11. The experimental procedure was the same as that in the case of the copper. The target current was kept at 3.9 to 4.1 mA and the input microwave power was almost constant. The Al^- ion current was increased by 4 times for an increment of the oven temperature of 15 $^{\circ}$C, and reached 6 μA. In the case of a nickel sputtering target the Ni^- ion current was also increased with an increase in the cesium oven temperature at the constant target current, and reached 59 μA.

3.5.2 Control of target temperature

The control of the target surface temperature is also an important factor in production of an intense negative-ion beam, because the amount of the cesium coverage of the target surface is influenced by the surface temperature. A sputtering target is heated by an incident cesium ion energy. The increasing temperature is decided by both the temperature of the target electrode and the thermal conductivity of the target material.
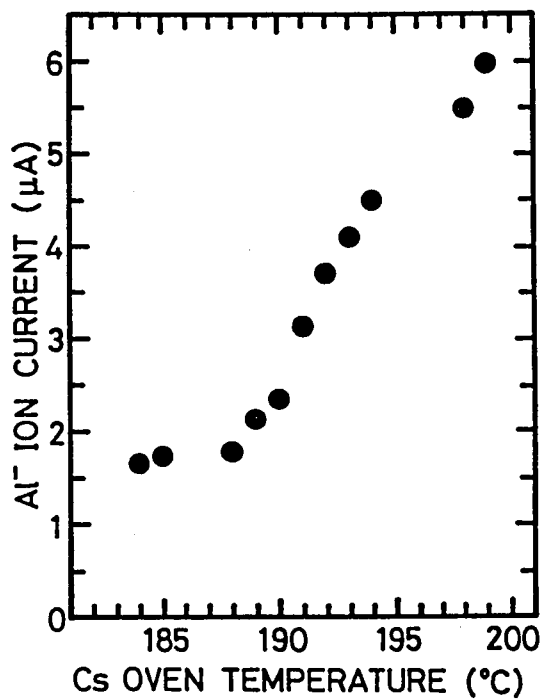
Fig. 3.11   Al⁻ ion current as a function of the
cesium oven temperature.   The target current was
kept at 3.9 to 4.1 mA and the input microwave
power was almost constant.

Thus, to keep the temperature of the target surface in a moderate range, the target electrode should be cooled according to a thermal conductivity of a target material.

The C^- ion currents as a function of the target current are shown in Fig. 3.12. The cesium ion current to the sputtering target was about one half of the target current, and the efficiency of the negative ion production, that is, the ratio of the negative ion current to the incident cesium ion current, is also indicated in the figure. The C^- ion currents are plotted for the methods of cooling the target electrode: (1) by liquid nitrogen, (2) by liquid carbon dioxide, and (3) not cooled. The C^- ion currents for these methods were directly proportional to the target current in a wide range of it. When the target was not cooled, the negative ion production efficiency was about 10 %. On the other hand, the efficiencies were about 5 % and about 4 % for the target electrode cooled by liquid carbon dioxide and liquid nitrogen, respectively. Since the thermal conductivity of carbon is fairly high, 2.5 W/cm·K, the surface temperature of the carbon target was not increased excessively without the cooling. In the case where the target electrode was cooled, the target surface temperature was so low that the negative ion production efficiency was decreased. It is considered that the excessive cooling of the target resulted in a thick cesium layer on the surface which lowered the sputtering yield of the target material. In this experiment the C^- ion current of 320 μA was obtained without the cooling.

The $^{11}B^-$ ion currents as a function of the target current are shown in Fig. 3.13. The dotted lines indicate the negative
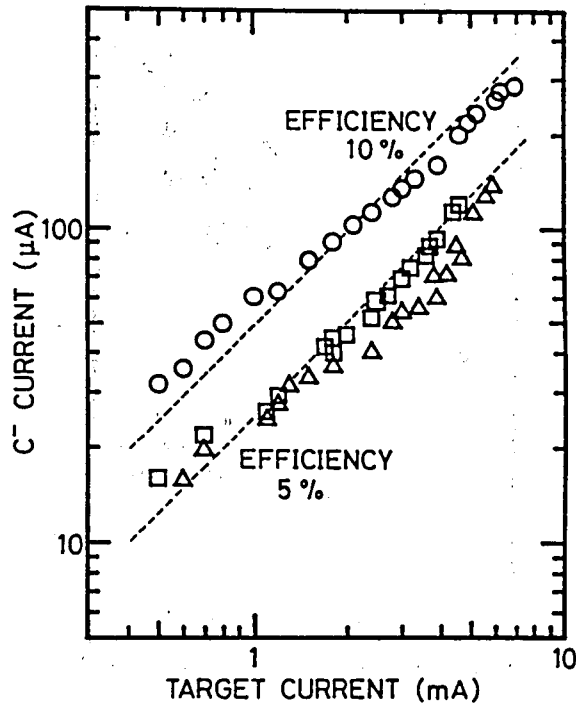
Fig. 3.12　C⁻ ion currents as a function of the
target current under the conditions where the
cesium ion beam energy was 17.0 keV and the
suppressor voltage 1.0 kV. The C⁻ ion currents
are plotted for three methods of cooling the
target electrode: △ liquid nitrogen, □ liquid
carbon dioxide, and ○ not cooled. The dotted
lines indicate the negative ion production
efficiency.

Fig. 3.13 $^{11}B^-$ ion currents as a function of the target current. The $^{11}B^-$ ion currents are plotted for three methods of cooling the target electrode: △ liquid nitrogen, □ liquid carbon dioxide, and ○ not cooled. The dotted lines indicate the negative ion production efficiency.

ion production efficiency. The $^{11}B^-$ ion currents are plotted for the same three methods of cooling the target electrode as those in the case of the carbon. S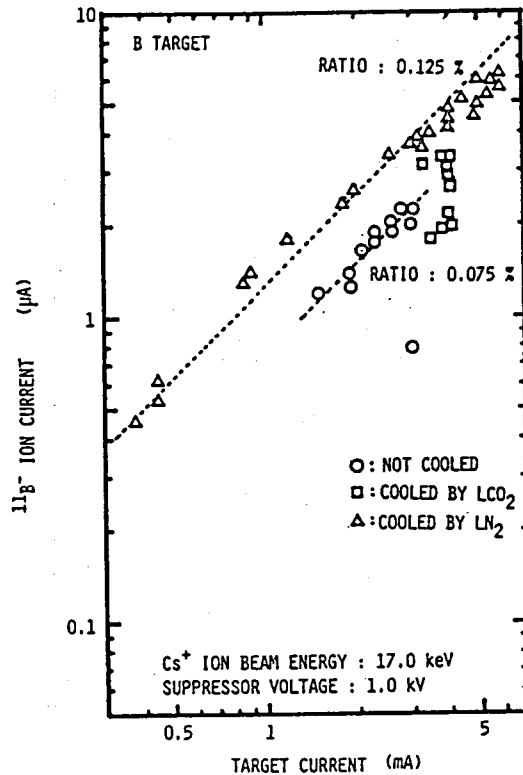ince boron has a very low thermal conductivity of 0.32 W/cm·K, the target temperature gradually rises without the cooling. When the target surface is heated over a temperature where the adsorbed monolayer of cesium particles starts to evaporate, the surface work function is raised, and then the negative ion production efficiency is decreased. As shown in Fig. 3.13, the $^{11}B^-$ ion yield was small when the target electrode was not cooled. On the other hand, the efficiency was fairly increased by cooling the target electrode by liquid nitrogen, because of suppression of an increase in the target temperature. As a result, 6 μA of the $^{11}B^-$ ion current was obtained. However, since the boron target used was made from sintered boron with about 50 % packing density which has an extremely low thermal conductivity, the target surface temperature was still high for the appropriate cesium coverage even when the target electrode was cooled by liquid nitrogen. To improve the thermal conductivity of the boron target, sputtering targets were made by high pressure pressing a mixture of 40 % of aluminum powder of 44 μm in diameter and 60 % of boron powder of 100 μm in diameter and vacuum firing at about 1100 °C for 30 minutes. Figure 3.14 shows the $^{11}B^-$ ion current as a function of the target current for this pressed and sintered boron target mixed by aluminum. The improvement of the thermal conductivity of the target was observed, and 15 μA of the $^{11}B^-$ ion current was obtained when the target electrode was cooled by liquid carbon dioxide. It is noted that the efficiency of the $^{11}B^-$ ion
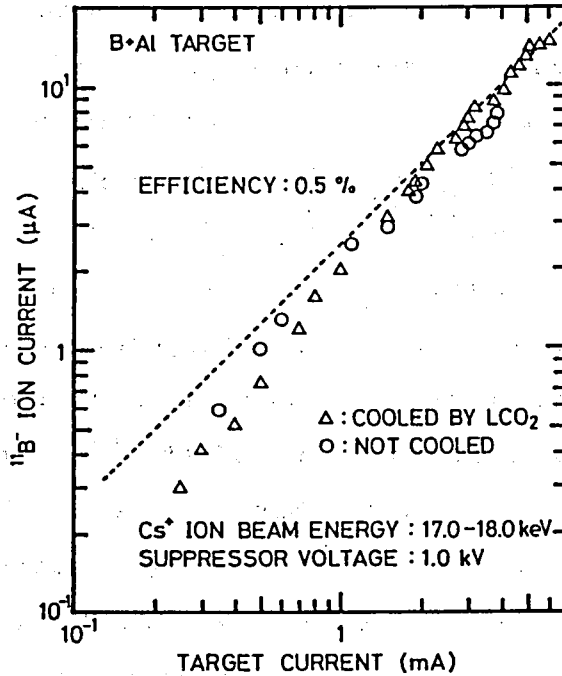
Fig. 3.14 $^{11}B^-$ ion currents as a function of the
target current in the case of the pressed and
sintered boron sputtering target mixed by
aluminum. The $^{11}B^-$ ion currents are plotted for
two methods of cooling the target electrode:
$\triangle$ liquid carbon dioxide and $\bigcirc$ not cooled. The
dotted line indicates the negative ion production
efficiency.

production was fairly increased even when the target electrode
was not cooled.

3.5.3 Intense negative-ion beam production

In the previous sections, the experimental results about the
intense negative-ion beam production of various elements have
been presented from the point of view of the effects of both the
neutral cesium particle bombardment and the target temperature
control of the NIABNIS. As a consequence, it is found that a
negative ion yield is proportional to the target current, that
is, the cesium ion current, on condition that the optimal cesium
coverage on the target surface is maintained. Therefore, to
produce an intenser negative-ion beam, the cesium ion current to
the target should be more increased. When ions are extracted
from a single aperture at a certain ion extraction voltage, the
maximum extractable ion current of a certain element is decided
generally by the aspect ratio of the ion extraction system, that
is, the ratio of the diameter of the ion extraction aperture (2a)
to the ion extraction gap (d). The around 6 mA of the target
current, one half of which is estimated to be the cesium ion
current to the target, is considered to be an upper limit at the
aspect ratio of 2/3 which was the experimental condition (2a = 2
mm and d = 3 mm) in the previous sections. Here, experimental
results of intenser negative-ion beam production of carbon by
increasing the aspect ratio of the cesium ion extraction system
are presented.

Figure 3.15 shows the C^- ion current as a function of the
target current when the aspect ratio of the cesium ion extraction
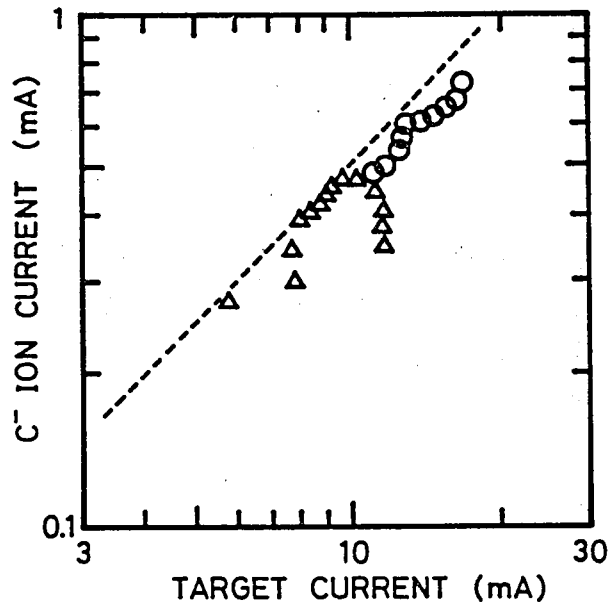
Fig. 3.15 C⁻ ion current as a function of the target current. The target electrode was not cooled (△), and cooled by air (○). The aspect ratio of the cesium extractor and the energy of the positive cesium ion beam were 8/7 and 19 keV, respectively.

Fig. 3.16   Maximum C⁻ ion current and the target
    current according to the maximum C⁻ ion current
    (maximum target current) as a function of the
    aspect ratio of the cesium ion extraction system.

system was 8/7 (2a = 4 mm and d = 3.5 mm). The C^- ion current was increased with an increase in the target current, and reached 0.74 mA at the target current of 17 mA. The cooling of the target electrode by air was required at a target current of more than 10 mA in order to suppress the excessive rise of the target surface temperature. The maximum C^- ion current and the target current according to the maximum C^- ion current (maximum target current) as a function of the aspect ratio of the cesium ion extraction system are shown in Fig. 3.16. The maximum target current was proportional to the second power of the aspect ratio, that shows an excellent performance of the microwave cesium ion source. The maximum C^- ion current was also proportional to the second power of the aspect ratio, that is, proportional to the maximum target current. Hence, a further more C^- ion current can be obtained by more increasing the cesium ion current. In the case of the ion extraction from a single aperture, it is very difficult that the aspect ratio is furthermore increased, because of the distortion of the plasma boundary emitting the ions. However, if ions are extracted from a slit or multiple apertures, the several times of cesium ion current could be obtained, and then a furthermore intense negative-ion beam could be delivered.

3.5.4 Negative ion production of refractory metal

Refractory metals are attractive for material synthesis because they have high melting points and show chemical stability. Their compounds are utilized as coating materials. Generally, the positive ion beams of refractory metals are obtained by use of their chlorides as discharge gases. However,

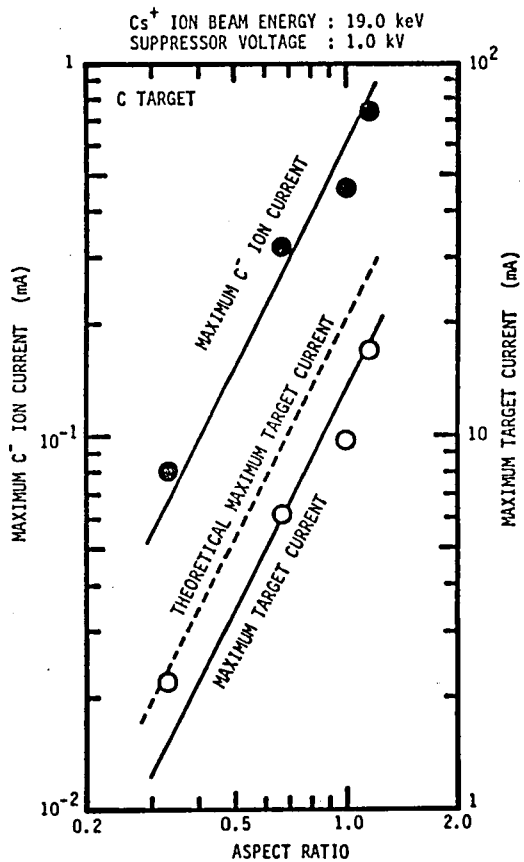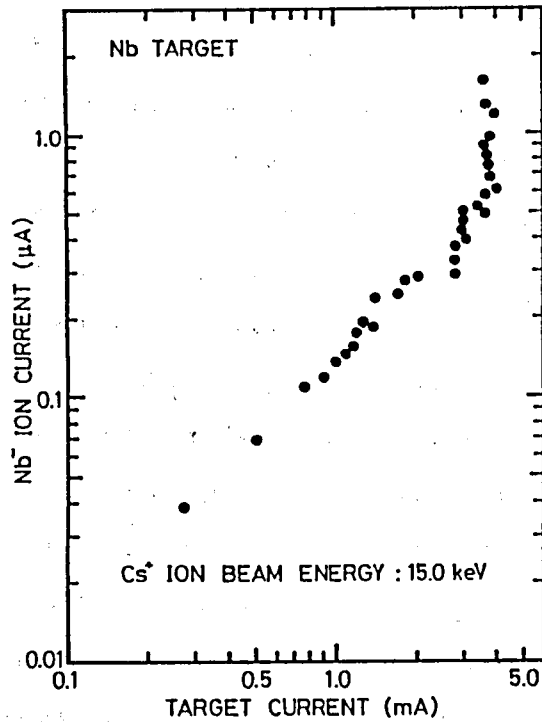Fig. 3.17   Nb⁻ ion current as a function of the
target current. The target electrode was slightly
cooled by air. Note that the effect of the
neutral cesium particle bombardment is found at
the target current of about 4 mA.

the chamber of the ion source and the beam handling chamber are contaminated by the chloride gas, and the lifetime of the ion source is short. Therefore, it is difficult to produce a large amount of positive ion beams of the refractory metals. The NIABNIS is a sputter negative ion source and, thus, it has a possibility to obtain negative ion yields of the refractory metals more than positive ion yields of them. Figure 3.17 shows the Nb⁻ ion current as a function of the target current. Since niobium has a high sputtering ratio, the effect of the neutral cesium particle bombardment was observed at the target current of about 4 mA. In this experiment, 1.6 µA of the Nb⁻ ion current was obtained under the conditions where the target current was 4 mA and the target electrode was slightly cooled by air. When a molybdenum target and a tantalum target were used as a sputtering target, 1.0 µA of the Mo⁻ ion current and 0.4 µA of the Ta⁻ ion current were obtained, respectively. The negative ion yields of refractory metals are expected to be more increased if the target purity is improved, because high negative ion yields of the elements with a high electron affinity such as oxygen, hydrogen and carbon were observed in the mass spectra.

3.5.5 Negative ion production of gaseous material

In order to obtain negative hydrogen ions, hydrogen gas was introduced into the cesium plasma production chamber and was discharged with cesium. A titanium sputtering target was bombarded with the generated ions and neutral particles. It was difficult to obtain titanium as negative ions. Figure 3.18 shows the negative hydrogen ion current as a function of the hydrogen
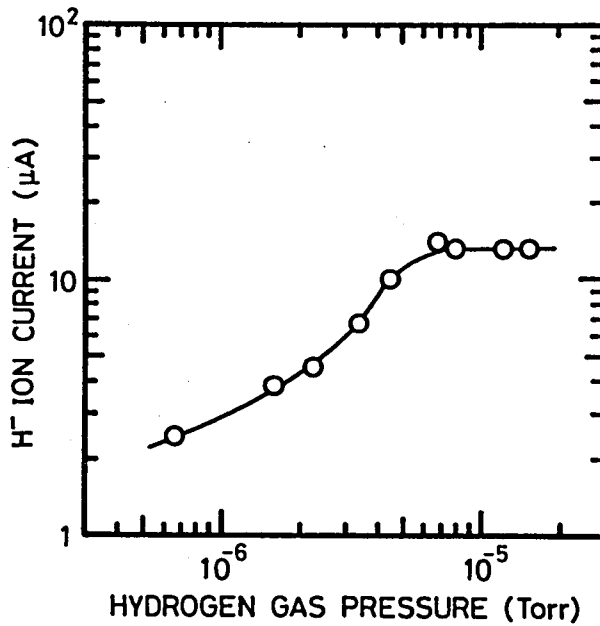
Fig. 3.18   H⁻ ion current as a function of the
hydrogen gas pressure under the conditions where
the cesium ion beam energy is 13.0 keV, the
suppressor voltage 500 V, and the target currents
2.2 – 2.7 mA.

gas pressure. The negative hydrogen ion current was increased
with an increase in the hydrogen gas pressure and reached 14 μA.
This experimental result shows the possibility of highly
efficient negative ion production of gas or metal vapor.

3.5.6 Mass spectrum

The mass spectra in the cases of carbon, silicon, copper,
nickel, boron, and aluminum sputtering targets are shown in Figs.
3.19, 3.20, 3.21, 3.22, 3.23 and 3.24, respectively. The
vertical axis indicates the negative ion current detected by a
Faraday cup after the mass separation. In the cases of carbon,
silicon, copper and nickel sputtering targets the atomic negative
ion yields were more than the molecular negative ion yields,
while the dimer molecular negative ion yields were more than the
atomic negative ion yields in the cases of boron and aluminum
sputtering targets. The ratio of the atomic to molecular
negative ion yields also seemed to vary with the amount of the
neutral cesium spray and the target temperature.

3.6 Discussion

The negative ion production efficiency is strongly dependent
on the surface work function, as described in section 3.2. The
appropriate condition of the cesium-covered surface, i.e., cesium
coverage between θ_A and θ_B in Fig. 3.1, should be achieved for
intense heavy negative-ion production. The control of target
temperature is effective to keep the cesium coverage in the
appropriate condition. As shown in Fig. 3.13, in the case of the

Fig. 3.19 An example of the mass spectrum in the
case of a carbon sputtering target. The vertical
axis indicates the negative ion current detected
by a Faraday cup after the mass separation.

Fig. 3.20 An example of the mass spectrum in the
case of a silicon sputtering target. The vertical
axis indicates the negative ion current detected
by a Faraday cup after the mass separation.

Fig. 3.21 An example of the mass spectrum in the case of a copper sputtering target. The vertical axis indicates the negative ion current detected by a Faraday cup after the mass separation.

Fig. 3.22 An example of the mass spectrum in the case of a nickel sputtering target. The vertical axis indicates the negative ion current detected by a Faraday cup after the mass separation.
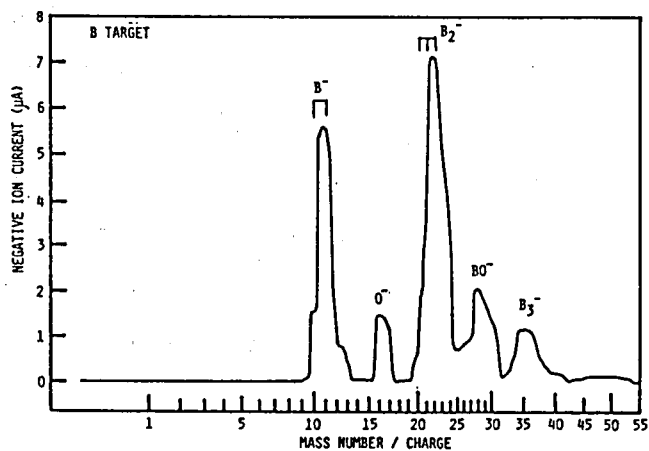
Fig. 3.23   An example of the mass spectrum in the
case of a sintered boron sputtering target.   The
vertical axis indicates the negative ion current
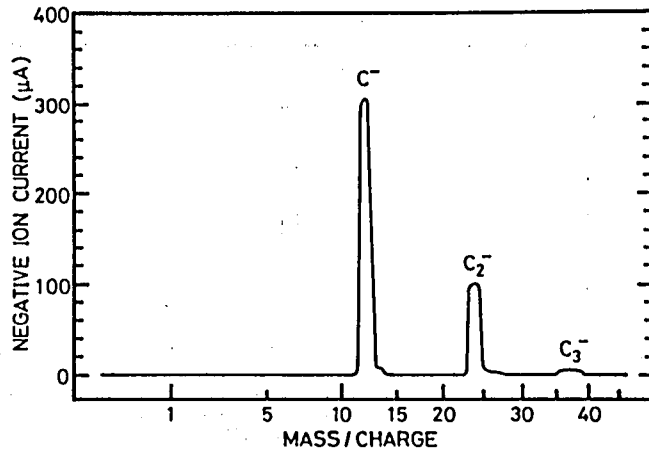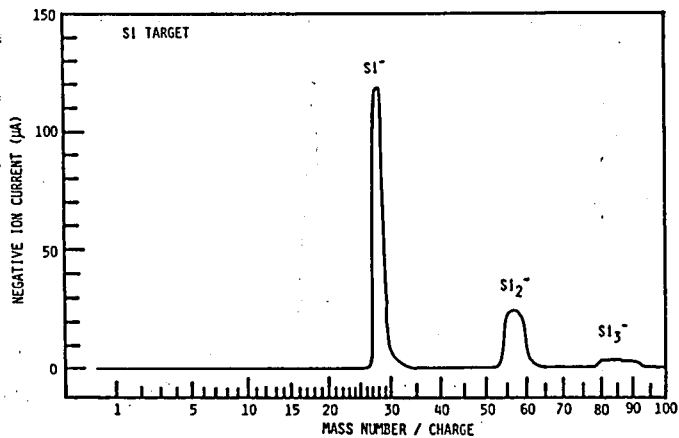detected by a Faraday cup after the mass
separation.
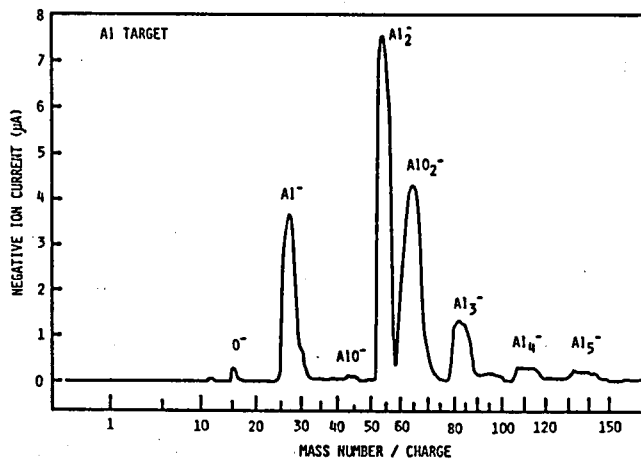
Fig. 3.24   An example of the mass spectrum in the
case of an aluminum sputtering target.   The
vertical axis indicates the negative ion current
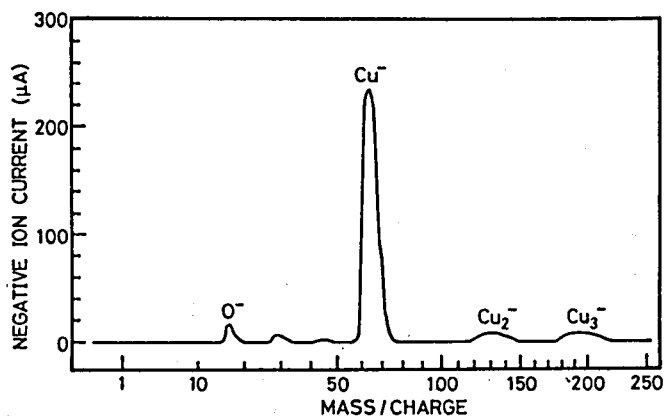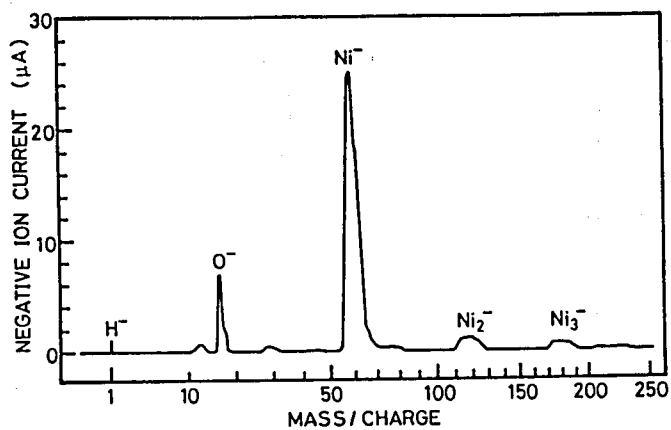detected by a Faraday cup after the mass
separation.

107

boron sputtering target with a low thermal conductivity, the negative ion production efficiency was much reduced without cooling of the target electrode. This is because the adsorbed cesium particles are desorbed at a high temperature, which results in a high surface work function. When cesium particles are present on the surface cesium monolayer, the binding energy on the top surface is due to the bond between Cs and Cs. Since this binding force is very weak, the adsorbed cesium particles on the top surface evaporate even at a low temperature of around room temperature[36]. Therefore, only a monolayer of cesium particles exists on the surface in the temperature range from around the room temperature to several hundreds $^{\circ}$C. Since this range is fairly wide, the appropriate operating condition is easily achieved by cooling the target electrode according to the thermal conductivity of the target material. In the case of materials with an extremely low thermal conductivity such as sintered boron, however, the thermal conductivity of the sputtering target have to be raised by mixing material with high thermal conductivity such as aluminum. On the other hand, excessive cooling of the sputtering target lowers the negative ion yields, as shown in Fig. 3.12. In this case cesium multilayer is formed on the surface of sputtering target, leading to reduction of the sputtering yield. The implantation range of the cesium ion with an energy of 10-20 keV for cesium metal is estimated to be about 30-40 $\overset{\circ}{A}$[36], which corresponds to 6-8 atomic layers. Only 8 cesium atomic layers on the surface prevent the sputtering of the target material. Thus, excessive cooling of the sputtering target lowered the negative ion production

efficiency.

The additional supply of neutral cesium particles is also effective to keep the surface work function as low as possible. The adsorbed cesium atoms on the surface of sputtering target are sputtered off together with the target material. Hence, in the case of a sputtering target with a high sputtering ratio, the cesium coverage is insufficient and, as a result, the efficiency of negative ion production is reduced. To prevent this situation, low energy cesium particles which do not follow the sputtering should be positively supplied onto the sputtering target surface. As shown in Figs. 3.10 and 3.11, the additional supply of neutral cesium from the cesium ion extraction aperture is extremely effective to maintain the cesium monolayer on the target surface for the target material with high sputtering ratio such as copper, nickel and aluminum. Ionized cesium particles (that is, a cesium ion beam) have a strong directivity to the sputtering target, while neutral cesium particles do not. Most of the ionized cesium particles arrive at the target surface. The neutral cesium particles, however, are emitted into a wide solid angle, and the effective neutral cesium particles which arrive at the sputtering target are about 22 % of the total neutral cesium particles emitted from the extraction aperture, as shown in Fig. 3.8. In the case of high sputtering yield materials, even this quantity of effective neutral cesium particles can contribute to keep the cesium monolayer on the target surface.

When low sputtering yield materials such as carbon are used for a sputtering target, a sufficient quantity of cesium

particles is at all times adsorbed on the sputtering target surface during sputtering by the cesium ion beam. As a result, the negative ion production efficiency is always high, and is hardly increased even when the ratio of neutral to ionized cesium particles is increased. The sputtering ratio of silicon (3.0 atoms/ion by 20 keV Xe^+ ion bombardment) is smaller than that of aluminum (4.3 atoms/ion), as indicated in Table 3.1. In the case of a silicon sputtering target, it was not observed clearly that the increase in the Si^- ion current was dependent on the neutral cesium spray. The Si^- ion current was increased with an increase in the target current, and reached 170 μA. Carbon and boron have smaller sputtering ratios than silicon, and their negative ion production characteristics were mainly dependent on the target current, that is, the ionized cesium particle bombardment. Thus, it is thought that the neutral cesium particle bombardment is effective remarkably on elements which have higher sputtering ratio than silicon.

Part of the positive cesium ions enter the negative ion extraction region. The positive space charge of Cs^+ influences the negative ion extraction characteristics. Negative space-charge compensation with the positive space charge of Cs^+ results in relaxation of space-charge limitation in the negative ion extraction[37]. The extractable maximum ion current is 1.86 times the space-charge limited ion current without space-charge compensation if both negative and positive ion currents are in the space-charge limited region. This effect is discussed as follows, taking the experiment of high current negative carbon extraction as an example. The space-charge limited C^- current

without space-charge compensation is calculated to be 2.65 mA from the perveance of the extraction system under the conditions where the extraction voltage is 19 kV and the aspect ratio of the negative ion extraction system 2.0/7.0. On the other hand, the extracted equivalent C^- current is estimated to be about 3.95 mA, when taking into account both the transmission factor of an ion beam through the einzel lens and the mass separator, and turning the total negative ion current into the equivalent C^- current. Therefore, it can be seen that the space-charge limitation is considerably relaxed by the space-charge compensation.

Table 3.4 shows a comparison of the obtained negative ion currents from the NIABNIS with those from conventional negative ion sources[1,3,5,9-12,38-40].*) The operating principle of the NIABNIS is midway between UNIS and ANIS in order to obtain negative ion currents of various elements as equally as possible. Table 3.4 demonstrates the realization of this concept. Moreover, increases of the negative ion currents were achieved. The negative ion current is proportional to the target current, i.e., the cesium current to the target, whenever the appropriate cesium layer is maintained on the target surface. Since the aspect ratio of the cesium ion extraction system was 2/3 except for the case of the carbon sputtering target, the negative ion

----

*)Foot note: Recently the VNIS (versatile negative-ion source) has been developed where the sputtering target and the surface cesium ionizer are in the same chamber filled with cesium vapor[39,40]. The obtained negative ion currents from the VNIS are also shown in Table 3.4.

111

Table 3.4 Comparison of the obtained negative ion
currents from the NIABNIS with those from
conventional negative ion sources[1,3,5,9-12,38-40].

Negative ion source	Mueller and Hortig	UNIS	ANIS	SPIGS	VNIS	NIABNIS
Negative Ion Current (μA)	C 2.2 C_2 3.4 Cr 0.1 Cu 6.0 Ag 14 Au 12	B 2.3 C 50 Al 0.2 Si 27 P 0.6 Ge 1.1 As 1.0 In 0.03 Sb 0.32 Te 1.8 Ti 0.005 Ni 6.6 Cu 7 Nb 0.027	Li 1.0 B 0.04 BO 2.5 C 20 C_2 15 Al 2.3 Ti 0.9 Ni 55 Cu 51 Nb 1.0 Mo 0.14 Ag 36 Ta 3 Au 80	Li 0.3 C 3 V 0.1 Ni 4 Cu 22 Nb 0.2 Ta 0.2	Be 0.1 B 35 C 300 F 250 Al 6 Si 250 P 25 S 200 Fe 4 Cu 150 Ni 150 Pt 150 Au 200	C 735 C_2 ~200 B 15 B_2 20 Cu 320 Al 6.0 Al_2 7.7 Sb 0.6 Sb_2 2.1 Si 170 As 2.4 Ni 59 Nb 1.6 Mo 1.0 Ta 7.6 W 1.3
Positive Ion Energy Current	Kr^+ or Ar^+ 10-30 keV	Cs^+ 20-30 keV 1-1.5 mA	Cs^++(Xe or Ar) 1-2 keV ~10 mA	Cs^+ 2.25 keV 17-26 mA	Cs^+ 5-10 keV 5-15 mA	Cs^+ 10-25 keV 1-10 mA

current can be increased as the aspect ratio is increased. More
increase in the negative ion current is expected when the cesium
current to the target is more increased by applying slit- or
multi-aperture-type ion extraction system. This ion source can
be used for high negative-ion current applications such as
negative ion beam modification and negative ion beam deposition.

A compact body of the negative ion source is essential for
use as an ion source for material science. In this ion source
the compact body, which resulted in a high current output, was
realized.

3.7 Summary

A neutral- and ionized-alkaline-metal bombardment-type heavy
negative-ion source (NIABNIS) was developed for the application
of the negative ion beam to material science. The NIABNIS is a
high current and compact heavy negative-ion source where
simultaneous bombardment of both neutral- and ionized-alkaline-
metal particles on a sputter cone is utilized for overcoming the
disadvantages of the universal negative-ion source (UNIS) and the
Aarhus negative-ion source (ANIS). To supply a sufficient amount
of neutral and ionized cesium particles onto the sputtering
target surface, the axial magnetic field extraction-type
microwave ion source, which is a plasma ion source, is used for
the primary cesium ion source, and the distance between the
extraction aperture of the cesium ion beam and the sputtering
target is minimized. The target temperature of the NIABNIS is
also controllable. The operational characteristics of the

NIABNIS was investigated with regard to the effects of the neutral cesium particle supply and the target temperature control. From the experimental results on the effect of the neutral cesium particle bombardment, it is found that the positive supply of the neutral cesium particles is extremely effective to enhancement of the negative ion current for elements with high sputtering ratios such as copper, nickel and aluminum. From the experimental results on the effect of the target temperature control, it is also found that the cooling of the target electrode is required to increase the negative ion current for elements with low thermal conductivity such as boron. Even for elements with high thermal conductivity, the cooling is required when the incident cesium ion current is fairly increased. On the other hand, excessive cooling of the target results in lowering negative ion production efficiency. The optimization of the target surface conditions was discussed in detail, and it is related to the formation of the cesium monolayer on the target surface which results in a minimum surface work function. In the NIABNIS, the optimization of the target surface conditions is easily realized for various elements by the neutral cesium particle supply and the target temperature control. In the experiments of the intenser negative ion production, it is found that the negative ion current is proportional to the incident cesium current, if the cesium coverage is maintained in an appropriate condition. As a result, nearly a mA of the C^- ion current was obtained by furthermore increasing an incident cesium ion current. It is also indicated that highly efficient negative ion production of refractory metal

and gaseous material is possible. The obtained negative ion yields from the NIABNIS are greater than those obtained from the conventional negative ion sources such as the UNIS and the ANIS. This negative ion source is suitable for ion beam modification and ion beam deposition where high current ion beams are needed.

References (Chapter 3)

1) M.Mueller and G.Hortig, IEEE Trans. Nucl. Sci. **NS-16** (3), 38 (1969).

2) R.Middleton and C.T.Adams, Nucl. Instrum. Methods **118**, 329 (1974).

3) R.Middleton, Nucl. Instrum. Methods **144**, 373 (1977).

4) H.H.Andersen and P.Tykesson, IEEE Trans. Nucl. Sci. **NS-22** (3), 1632 (1975).

5) P.Tykesson, H.H.Andersen, and J.Heinemeier, IEEE Trans. Nucl. Sci. **NS-23** (2), 1104 (1976).

6) K.R.Chapman, Nucl. Instrum. Methods **124**, 299 (1975).

7) R.E.M.Hedges, J.O.Wand and N.R.White, Nucl. Instrum. Methods **173**, 409 (1980).

8) N.R.White, Nucl. Instrum. Methods **206**, 15 (1983).

9) G.D.Alton and G.C.Blazey, Nucl. Instrum. Methods **166**, 105 (1979).

10) H.V.Smith Jr., Nucl. Instrum. Methods **164**, 1 (1979).

11) H.V.Smith Jr. and H.T.Richards, Nucl. Instrum. Methods **125**, 497 (1975).

12) H.V.Smith Jr., IEEE Trans. Nucl. Sci. **NS-23** (2), 1118 (1976).

13) J.Ishikawa, Y.Takeiri, H.Tsuji, and T.Takagi, Proceedings of the International Ion Engineering Congress, Kyoto (Institute of Electrical Engineers of Japan, Tokyo, 1983), p.131.

14) J.Ishikawa, Y.Takeiri, H.Tsuji, T.Taya, and T.Takagi, Nucl. Instrum. Methods **232[B4]**, 186 (1984).

15) Y.Takeiri, J.Ishikawa, and T.Takagi, Proceedings of the Eighth Symposium on Ion Sources and Ion-Assisted Technology,

Tokyo (The Research Group of Ion Engineering, Kyoto University, 1984), p.31.

16) K.Wittmaak, Nucl. Instrum. Methods **168**, 343 (1980).

17) K.Wittmaak, Inelastic ion-surface collisions, ed. N.H.Talk et al. (Academic Press, New York, 1977), p.153.

18) G.D.Alton, IEEE Trans. Nucl. Sci. **NS-26** (1), 1542 (1979).

19) P.Joyes and B.Djafari-Rouhani, Handbook of surfaces and interacts, Vol.2, ed. L.Dobrzynski (Garland stpm Press, 1978), p.359.

20) Z.Šroubek, Surf. Sci. **44**, 47 (1974).

21) M.Cini, Surf. Sci. **54**, 71 (1976).

22) B.Rasser, J.N.M.van Wunnik, and J.Los, Surf. Sci. **118**, 697 (1982).

23) M.E.Kishinevskii, Sov. Phys. Tech. Phys. **20**, 799 (1975).

24) M.E.Kishinevskii, Sov. Phys. Tech. Phys. **23**, 456 (1978).

25) P.D.Townsend, J.C.Kelly, and N.E.W.Hartley, Ion implantation, sputtering and their applications (Academic Press, New York, 1976), p.111.

26) M.W.Thompson and P.S.Nelson, Philos. Mag. **18**, 377 (1968).

27) P.Sigmund, Phys. Rev. **184**, 383 (1969).

28) N.Matsunami, Y.Yamamura, Y.Itikawa, N.Itoh, Y.Kazumata, S.Miyagawa, K.Morita, and S.Shimizu, Energy dependence of sputtering yields of monatomic solids (Institute of Plasma Physics, Nagoya University, 1980) IPPJ-AM-14.

29) J.R.Hiskes, A.Karo, and M.Gardner, J. Appl. Phys. **47**, 3888 (1976).

30) M.L.Yu, Phys. Rev. Lett. **40**, 574 (1978).

31) G.D.Alton, Proceedings of the International Ion Engineering

Congress, Kyoto (Institute of Electrical Engineers of Japan, Tokyo, 1983), p.85.

32) W.G.Graham, Proc. 2nd Intern. Symp. Production and Neutralization of Negative Ions and Beams, Brookhaven, 1980, BNL-51304, ed. T.Sluyters, p.126.

33) M.L.Yu, Proc. Symp. Production and Neutralization of Negative Hydrogen Ions and Beams, Brookhaven, 1977, BNL-50272, ed. K.Prelec, p.48.

34) H.Tsuji, T.Taya, J.Ishikawa, and T.Takagi, Proceedings of the International Ion Engineering Congress, Kyoto (Institute of Electrical Engineers of Japan, Tokyo, 1983), p.141.

35) B.B.Dayton, 1956 Natl. Symp. on Vacuum Technology and Transport (Pergamon, New York, 1957), p.5.

36) R.G.Wilson and G.R.Brewer, Ion beams with applications to ion implantation (Wiley, New York, 1973).

37) J.Ishikawa, F.Sano, and T.Takagi, J. Appl. Phys. **53**, 6018 (1982).

38) H.V.Smith Jr, Nucl. Instrum. Methods **163**, 269 (1979).

39) R.Middleton, Nucl. Instrum. Methods **214**, 139 (1983).

40) R.Middleton, Nucl. Instrum. Methods **A220**, 105 (1984).

Chapter 4

MASS–SEPARATED NEGATIVE–ION–BEAM DEPOSITION SYSTEM

4.1 Introduction

A mass-separated negative-ion-beam deposition system, which was newly developed[1,2], differs from conventional positive-ion-beam deposition systems[3-10]. Negative ion beams were used for two reasons. First, sufficiently intense negative ion beams for negative-ion-beam deposition could be produced in a high vacuum environment by the NIABNIS, as described in the previous chapter. The NIABNIS delivers 0.74 mA of C^- ion beam, whose value is comparable to or higher than that produced by conventional positive ion sources. Since this source is of a sputter type, negative ions are produced in a quite high vacuum of the order of 10^{-6} Torr. Therefore, a gas flow from the ion source region to an ion beam transportation region or a target chamber can be neglected. Second, a negative-ion-beam deceleration system can be designed without considering the acceleration of oppositely charged particles, i.e., positive ions, in the deceleration field, because positive ion production by collisions or bombardment of the negative ion beam can be neglected. With a positive-ion-beam deposition system, the high-energy electrons, which are accelerated toward a substrate by the positive-ion-beam deceleration field, are difficult to eliminate, because many

electrons such as secondary electrons are present in the ion beam or around the deceleration electrode. Freeman et al. used the special electrode for the electron suppression just before the ion-beam deceleration electrodes[3], and Yagi et al. used the special magnetic field which was crossed on the electric field[7].

Formation of low energy ion beams was tried a few tens years ago by means of low energy ion extraction (several tens eV to several keV) and a simple lens system, and the ion beams without mass separation were directly decelerated on a target[11,12]. In the ion-beam deposition system, however, high-energy ion extraction (several tens keV) is required for mass separation, and, thus, a special electrode system for ion beam deceleration is also required so that an intense low-energy ion beam should be obtained for film formation by ion beam deposition. A mass-separated negative-ion-beam deposition system with the neutral- and ionized-alkaline-metal bombardment-type heavy negative-ion source (NIABNIS) and a new type of ion-beam deceleration electrode system was developed. In this chapter the construction of the deposition system and its characteristic features are described in detail.

4.2 Construction of Negative-Ion-Beam Deposition System

Figure 4.1 shows the schematic diagram of the mass-separated negative-ion-beam deposition system. It consists of a negative ion source (NIABNIS), a mass separator, and an ion-beam deceleration system. The mass separator is a sector magnet with a deflection angle of 90°, a radius of curvature of 500 mm, and a
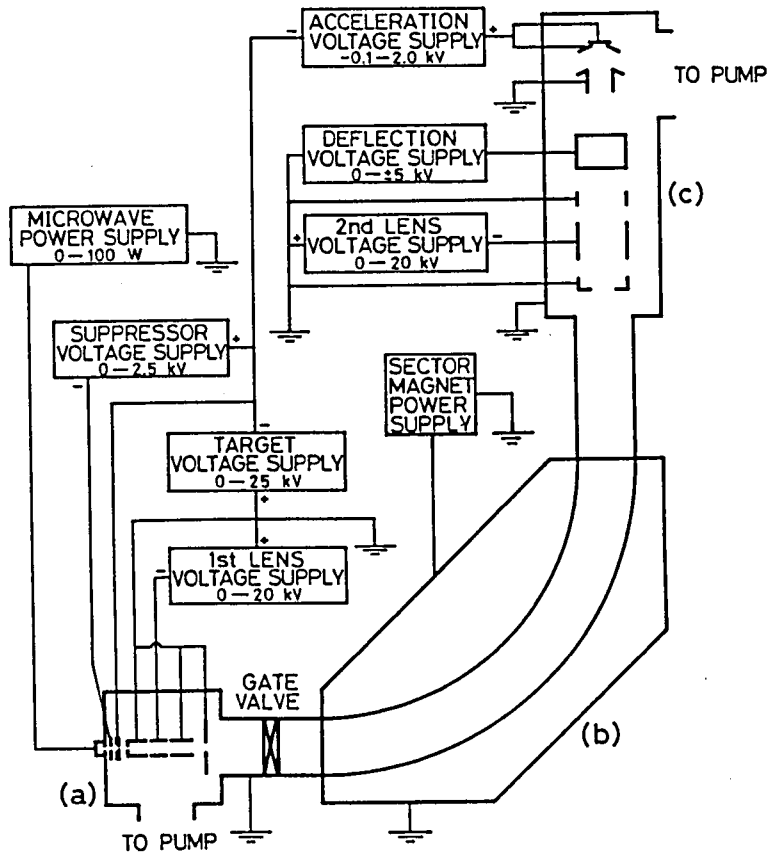
Fig. 4.1   Schematic diagram of the mass-separated
negative-ion-beam deposition system.   (a)
Negative ion source (NIABNIS), (b) mass separator,
and (c) negative-ion-beam deceleration system.

gap length between pole pieces of 80 mm. The negative ion source and the mass separator are operated at the ground potential. The substrate holder of the ion-beam deceleration system is at a negative high potential.

The chamber of the NIABNIS and the ion-beam deceleration chamber, i.e., the deposition chamber, are evacuated independently by a 6-inch oil-diffusion pump with a liquid-nitrogen trap. A gate valve is placed between the chamber of the NIABNIS and the mass separator. Another liquid-nitrogen trap is set near the deceleration electrode system to obtain a clean vacuum. Since the NIABNIS is a sputter negative ion source, there is no gas supply nor flow in operation. Thus, the gas pressures of the NIABNIS chamber and the deposition chamber in operation are quite low, 1×10^{-6} Torr and 7×10^{-7} Torr, respectively.

4.3 Ion-Beam Deceleration System

Various types of ion-beam deceleration systems have been reported[3-10]. Freeman and co-workers were the first to investigate the deceleration of mass-separated positive ion beams in detail, and focused high-intensity ion beams by decelerating them in the energy range of 100-1000 eV[3]. Since then, several types of mass-separated ion-beam deceleration systems have been developed, based on Freeman's system. However, it was difficult to obtain a large amount of ion beams with an energy below 100 eV. A new type of ion-beam deceleration system was designed, where high-intensity ion beams sufficient for thin-film formation

can be decelerated in the energy range of 10-100 eV[1,2].

In general, a divergent lens effect with a focal length of 3-4 times the deceleration gap exists in the ion-beam deceleration electrode system at the boundary where a beam enters the decelerating electric field from a drift space. To cancel this effect and obtain a parallel ion beam, some focusing is required. One method to solve this problem perfectly is to focus the ion beam by a convergent lens just before it enters the decelerating electric field. On the other hand, a beam-divergent effect due to a space-charge repulsion force is enhanced in the region where the ion-beam energy is especially low. To compensate for this effect an auxiliary electrode at $67.5°$ from the normal should be placed on the substrate. This electrode, which was originally proposed by Pierce[13], works to form the same electric field in the beam as the electric field under one-dimensional space-charge limitation. In this structure, the divergence of the decelerated ion beam caused by the two different mechanisms can be canceled completely and independently in any energy range. In the conventional ion-beam deceleration systems, the focal length of the decelerator varies with a decrement in the ion beam energy through the deceleration[10,14]. Thus, the yields of the decelerated ion beam are not maintained in high efficiency when the decelerated ion beam energies are changed. In this system, the focal length of the decelerated ion beam can be kept constant only by slight adjustment of the einzel lens voltage. Therefore, it is possible to deposit the ion beams efficiently in a wide energy range.

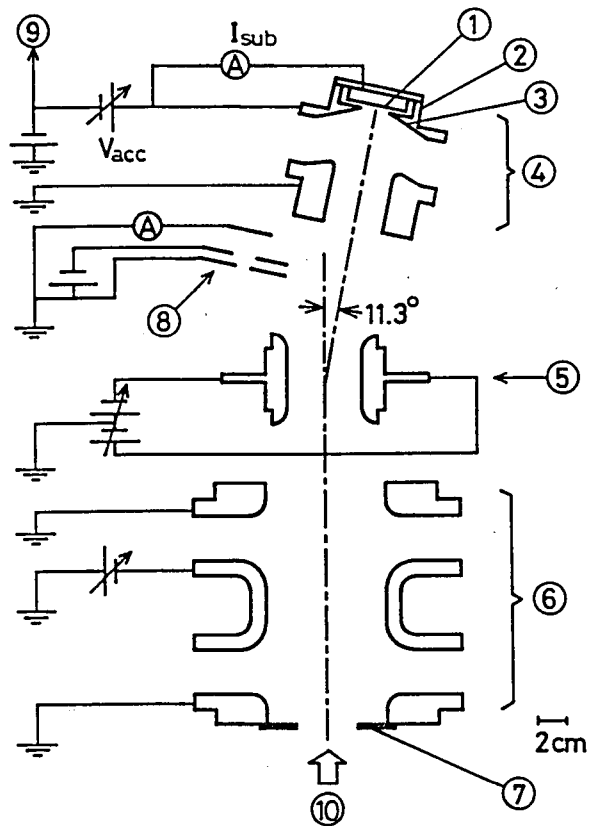Figure 4.2 shows the negative-ion-beam deceleration and

Fig. 4.2   Structure of negative-ion-beam
deceleration and deposition system. (1)
Substrate, (2) substrate holder, (3) auxiliary
electrode, (4) deceleration electrodes, (5)
deflection electrodes, (6) second einzel lens,
(7) diaphragm, (8) movable shutter with a Faraday
cup, (9) to the target electrode in the NIABNIS,
and (10) mass-separated negative ion beam.

124

deposition system with the above-mentioned functions. It consists of an einzel lens, deflection electrodes, a movable shutter with a Faraday cup, negative-ion-beam deceleration electrodes, and a substrate holder. A mass-separated negative ion beam is kept within 40 mm in diameter by a diaphragm and is converged by the einzel lens. After passage through the einzel lens the negative ion beam is deflected by 11.3° at the deflection voltage of about 7.0 kV to divide the negative ion beam from a neutral particle beam. The deflected ion beam is detected by the Faraday cup attached to the movable shutter when the shutter is closed. The selected ions enter the deceleration region when the shutter is open, and are deposited on the substrate. The deceleration electrodes generate the decelerating electric field in front of the auxiliary electrode and the substrate. Positive voltage is applied to the substrate and the auxiliary electrode against the sputtering target of the negative ion source. This potential difference between the sputtering target and the substrate potentials determines the final energy of the negative ion beam, which is hereafter referred to as the acceleration voltage of the negative ion beam.

The negative-ion-beam deceleration system does not need a special electrode for suppressing the oppositely charged particles, i.e., positive ions, which would be accelerated in the deceleration field, because positive ions are scarcely produced by collisions or bombardment with the negative ion beam. On the other hand, in the positive-ion-beam deposition system, an electrode must be put before the ion-beam deceleration electrodes for electron suppression. Thus, the structure of the negative-

Fig. 4.3   Structure of the substrate holder
attached to the auxiliary electrode.   (1)
Molybdenum plate, (2) tantalum heater, (3)
insulator (boron nitride), (4) insulator
(quartz glass), (5) permanent magnet, (6)
substrate, and (7) auxiliary electrode.
The temperature of the substrate can be
raised to 1000 °C.
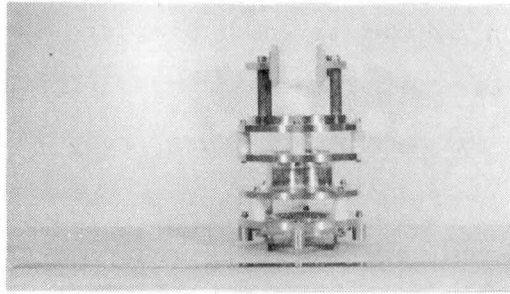
(a)
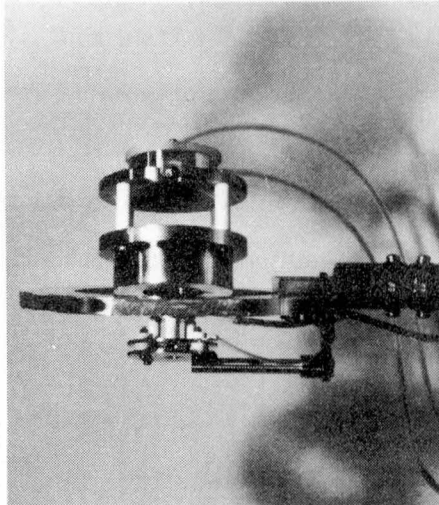
(b)
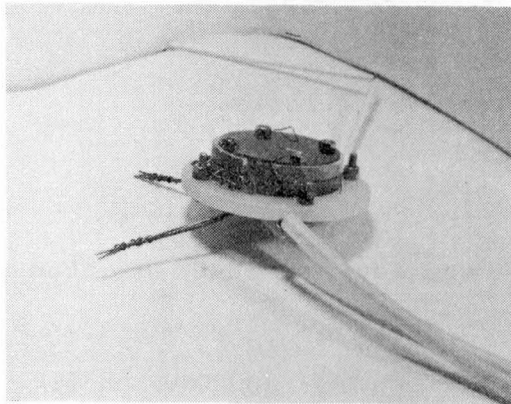
(c)

Fig. 4.4   Photographs of (a) the einzel lens
and the deflection electrodes, (b) the
deceleration electrode system, and (c) the
substrate holder.

ion-beam deceleration system is much simpler, so that the final yields of the decelerated ion beam are sufficient for film formation even in an extremely low energy range.

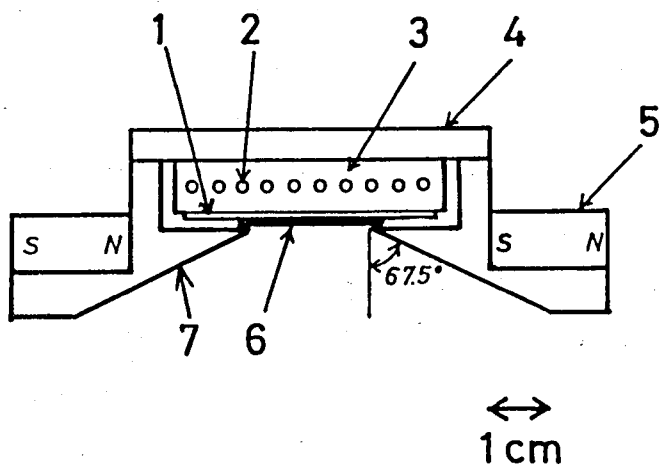The substrate current is measured at a high potential. Figure 4.3 shows the substrate holder attached to the auxiliary electrode. The temperature of the substrate holder can be raised to 1000 $^{\circ}$C by an insulated inner heater and the temperature is monitored by a thermocouple. To suppress the secondary electrons emitted from the substrate by the incident low-energy ions, two small permanent magnets are placed behind the auxiliary electrode. The secondary electrons are immediately returned to the substrate by the magnetic field parallel to the substrate surface.

Figures 4.4 (a), (b) and (c) show the photographs of the einzel lens and the deflection electrodes, the deceleration electrode system, and the substrate holder, respectively.

4.4 Decelerated Ion-Beam Trajectories

The ion-beam trajectories were simulated using a digital computer to examine the ion-beam deceleration system. In the simulation program which is shown in Appendix B, cylindrically symmetric coordinates were used, and thus no deflection of an ion beam was assumed. The ion beam whose trajectories were assumed to be initially parallel was converged by the einzel lens. Then, it was decelerated and returned to be parallel in front of the substrate by the divergent lens effect. Figure 4.5 (a) shows the results of the computer simulation when the 16-keV C$^-$ ion beam
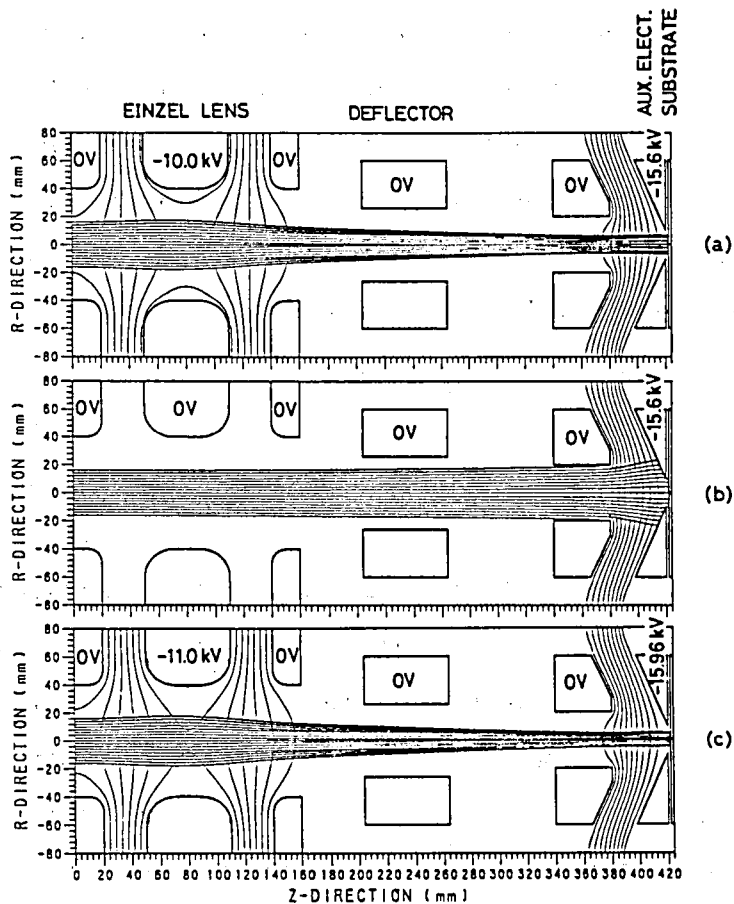
Fig. 4.5 Decelerated ion-beam trajectories by computer simulation for a 16-keV, 1-mA C⁻ ion beam. (a) A parallel ion beam with a final energy of 400 eV by einzel lens focusing; (b) a divergent ion beam with 400 eV with no focusing and; (c) a parallel ion beam with 40 eV with focusing. Thin solid lines indicate the equipotential lines of 1.56 kV unit in (a) and (b), and 1.596 kV unit in (c).

was decelerated to 400 eV and the ion beam current was 1.0 mA. The decelerated ion beam reached the substrate with a diameter of about 12 mm. In Fig. 4.5 (b) are shown the simulation results when the lens voltage was not applied and the other conditions were the same as those in Fig. 4.5 (a). A slightly broadened ion beam due to a space-charge repulsion force entered the region of the decelerating electric field from a drift space. The ion beam was diverged by the divergent lens effect due to the deceleration electrode system. In this case, most of the ions came to the auxiliary electrode. Figure 4.5 (c) shows the simulation results when the 16-keV, 1-mA C^- ion beam was decelerated to 40 eV. The diameters of the ion beams reaching the substrate were 9-12 mm after adjustment of the lens voltage when the decelerated ion-beam energies were lower than 400 eV.

The ion-beam diameter on the substrate, 2b, can be estimated at 2a/(r/f+1) by a simple calculation in which the space-charge effect during ion beam transportation is neglected, where 2a is the initial beam diameter, r the distance between the einzel lens and the divergent lens, and f the focal length of the divergent lens. f is about 3-4 times the gap between the deceleration electrodes, g. In this system, where a = 20 mm, r = 300 mm, and g = 20 mm, 2b is calculated as 6.7-8.4 mm. The slightly larger diameter of the ion beam on the substrate in the simulation than that in the simple estimation is due to consideration of the space-charge effect in the drift space in the simulation.
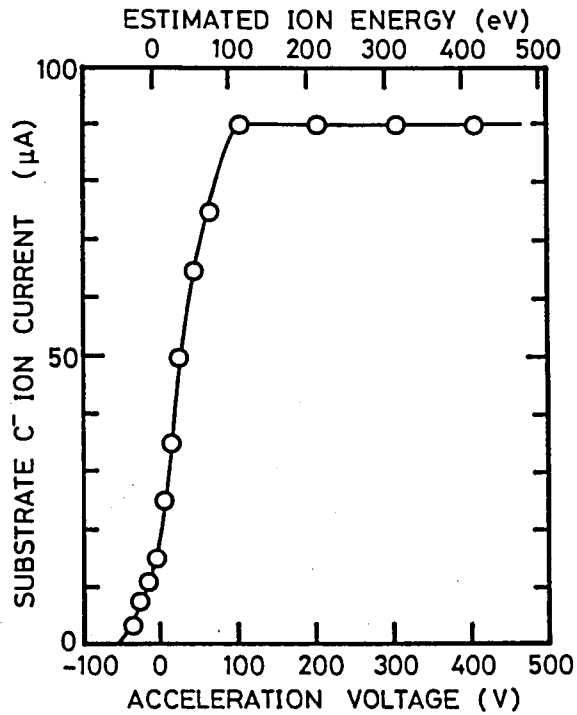
Fig. 4.6 Substrate C^- ion current as a function of
the acceleration voltage. The estimated ion
energy is shown on the upper abscissa. The C^- ion
beam energy before deceleration was 16 keV.

4.5 Operational Characteristics and Discussion

Operational characteristics of the negative-ion-beam deposition system were examined by using a C^- ion beam. The aspect ratio of the cesium ion extraction system was 2/3. An aluminum plate was used as a substrate. Figure 4.6 shows the substrate C^- ion current as a function of the acceleration voltage. Negative ions have an initial kinetic energy of about 15 eV which originates in the sputtering process. Figure 4.7 shows the energy distribution curve of the C^- ions by bombardment of the cesium ion beam[15]. The distribution had a peak at the initial kinetic energy of 14 eV and the energy spread, i.e., the full width at half-maximum (FWHM), was 10 eV. The value of the initial kinetic energy approximates the binding energy of the sputtering target atoms. In Fig. 4.6 the sum of the energy given by the acceleration voltage and the initial kinetic energy is also described as the estimated ion energy. The substrate current had a constant value of around 90 μA over the acceleration voltage of 100 V and rapidly decreased below 100 V. The substrate current, however, was as large as 50 μA at the acceleration voltage of 25 V. It is noted that the negative ions reached the substrate even when the acceleration voltage was less than 0 V because of the presence of the initial kinetic energy of the negative ions.

Figure 4.8 shows the derivative of the substrate C^- ion current to the acceleration voltage dI/dV. This figure indicates the energy distribution of the negative ions that reached the substrate through the deceleration system. Thus, this
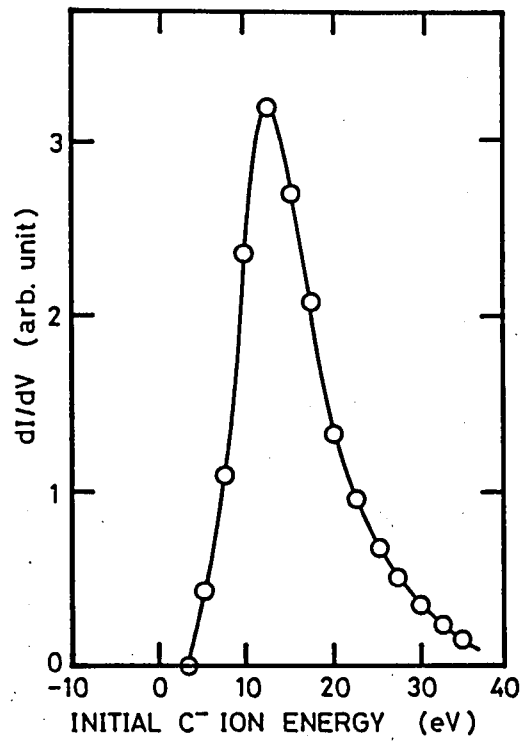
Fig. 4.7 Energy distribution curve for the C^- ions by bombardment of the cesium ion beam.
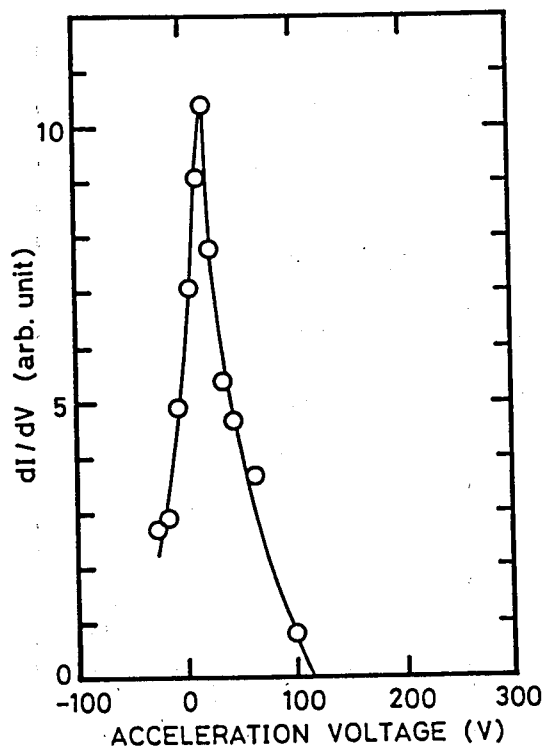
Fig. 4.8   Derivative of the substrate C^- ion
current to the. acceleration voltage dI/dV.

distribution is a factor in estimating the performance of the deceleration system. There existed a peak at the acceleration voltage of 20 V, and the FWHM was about 40 eV. In the ideal deceleration system, these values would be the same as those from the energy distribution shown in Fig. 4.7, that is, the peak energy in this coordinate is about -14 eV and FWHM is about 10 eV. The differences between this system and the ideal system were relatively small. Therefore, the high density and high current negative ion beam was successfully decelerated.

Figure 4.9 shows the substrate C^- ion currents as a function of the sputtering target current of the NIABNIS. The parameter is the acceleration voltage. The substrate currents were proportionally increased with an increase in the target current, since the negative ion yields, i.e., sputtering yields, are directly proportional to the target current in the NIABNIS. Considerable C^- ion currents were obtained even at the acceleration voltage of 0 V, i.e., the final ion beam energy of about 14 eV. When the aspect ratio was 2/3 and the target current was 4 mA, the C^- ion yield was about 200 µA in the NIABNIS. So, the substrate C^- ion currents are expected to be much increased at the higher target current.

The C^- ion beams were deposited on Si substrates to confirm that the films were formed by using the negative-ion-beam deposition system. Figure 4.10 shows a Rutherford backscattering (RBS) spectrum. The C^- ion beam was deposited on an n-Si (100) substrate when the substrate current was about 26 µA, the deposition time was about 80 min and the acceleration voltage was 100 V. The thickness of the deposited carbon film was estimated
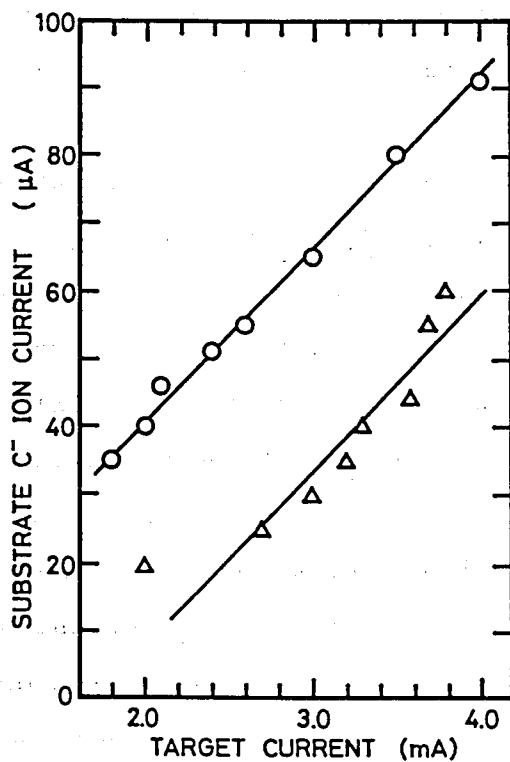
Fig. 4.9　Substrate C⁻ ion currents as a function
of the sputtering target current of the NIABNIS.
O : acceleration voltage 100 V and △ : 0 V.
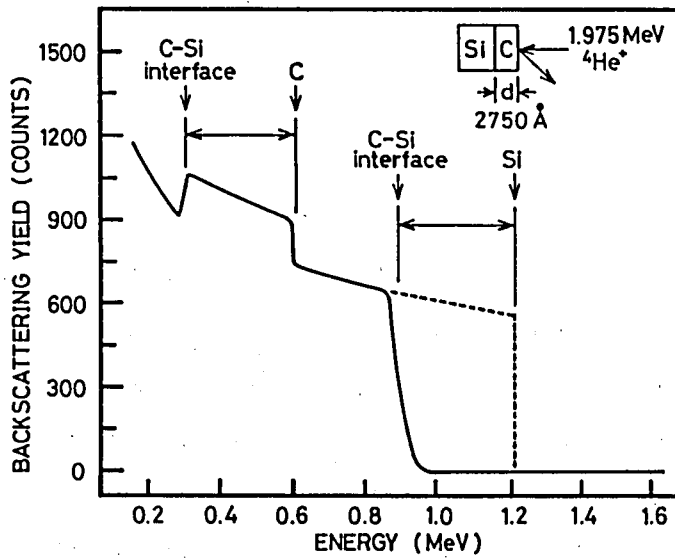
Fig. 4.10 Rutherford backscattering spectrum when a C⁻ deposition film on an n-Si (100) substrate (acceleration voltage of 100 V) was irradiated by the 1.975-MeV He⁺ ion beam.

at 2750 Å from the width of the carbon signal or the shift of the silicon edge, assuming that the atomic density of the deposited carbon film is 1.77×10^{23} atoms/cm^3. The area of the deposited carbon film was less than 1 cm^2. Table 4.1 lists the substrate current, the deposition time, the total deposited charge, and the deposited carbon film thickness for the C$^-$ deposition at the acceleration voltages of 10, 100, and 1000 V. The carbon films with several thousands Å in thickness were obtained in a few hours for every acceleration voltage. The areas of the carbon films were less than 1 cm^2 in every case. The deposited film size can be scaled up by varying the second lens voltage.

From Table 4.1 the deposition rate, which is defined here as a ratio of the film thickness to the total deposited charge, is estimated, assuming that the deposited film areas are the same at every acceleration voltage. Figure 4.11 shows the deposition rate as a function of the acceleration voltage. It is found that the deposition rate is gradually decreased as the acceleration voltage is increased. Since carbon has a low sputtering ratio, its critical energy, where the self-sputtering ratio is unity, seems to be fairly high. The self-sputtering ratio with various negative ion beams will be estimated by use of this deposition system if the density of the deposited film is measured.

The carbon sputtering target was replaced after the deposition of 20-30 films with several thousands Å in thickness. The lifetime of the sputtering target depends on the sputtering ratio of a target material. For silicon and copper, which have higher sputtering ratios than carbon, the lifetimes of the targets will be shorter than the carbon target.

138

Table 4.1   Substrate current, deposition time,

total amount of charge, and deposited carbon film

thickness for the C^- deposition at various

acceleration voltages.

Acceleration voltage (V)	Substrate current (μA)	Deposition time (min)	Total charge (Coul)	Film thickness (Å)
10	20	210	0.252	5500
100	26	80	0.1248	2750
1000	40	105	0.252	3700
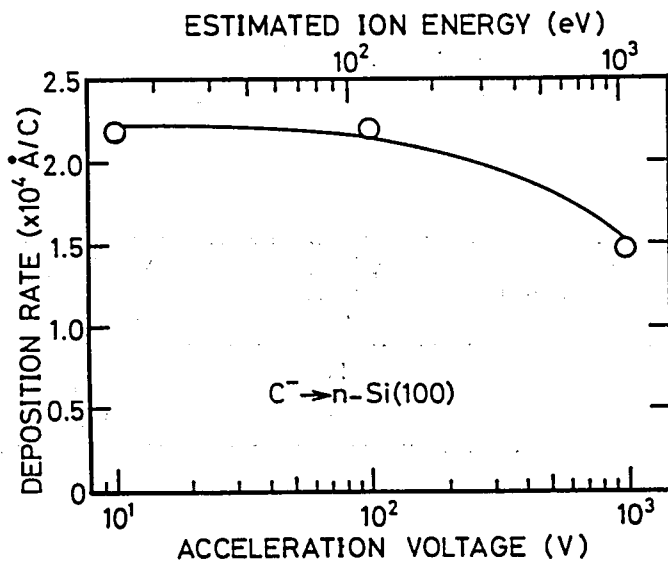
Fig. 4.11   Deposition rate as a function of the
acceleration voltage.

4.6 Summary

A mass-separated negative-ion-beam deposition system was developed to investigate the interactions between low-energy negative ions and solid surfaces and evaluated its usefulness as an advanced technique for film formation. The deposition system consists of an intense negative-ion source (NIABNIS) and a negative-ion-beam deceleration electrode system. Since the NIABNIS is a sputter ion source, there are no gas flow to the deposition chamber in operation. The negative-ion-beam deceleration electrode system has a new structure to suppress the divergent effects of the beam, where a convergent lens is placed close to the deceleration electrode system to suppress the divergent lens effect due to the deceleration gap, and where an auxiliary electrode with an angle of 67.5° from normal is placed on the substrate to compensate the divergent effect due to the space-charge repulsion force. This structure is also simpler than any of the positive-ion-beam deceleration systems because production of oppositely charged particles, i.e., positive ions, that might be accelerated in the deceleration field, can be neglected. A decelerated negative C^- ion current of several tens of μA in the range of a final energy of 10-100 eV and about 100 μA in the range of over 100 eV were obtained. In a deposition test, a carbon film with several thousands Å in thickness was obtained in a few hours at a final energy of about 24 eV. Carbon films are prepared by use of this negative-ion-beam deposition system, and their film properties are described in detail in chapter 5.

References (Chapter 4)

1) J.Ishikawa, Y.Takeiri, and T.Takagi, Rev. Sci. Instrum. **57**, 1512 (1986).

2) Y.Takeiri, K.Ogawa, J.Ishikawa, and T.Takagi, Proceedings of the Ninth Symposium on Ion Sources and Ion-Assisted Technology, Tokyo (The Research Group of Ion Engineering, Kyoto University, 1985), p.211.

3) J.H.Freeman, W.Temple, D.Beanland, and G.A.Gard, Nucl. Instrum. Methods **135**, 1 (1976).

4) J.Amano, P.Bryce, and R.P.W.Lawson, J. Vac. Sci. Technol. **13**, 591 (1976).

5) T.Tsukizoe, T.Nakai, and N.Ohmae, J. Appl. Phys. **48**, 4770 (1977).

6) K.Yagi, S.Tamura, and T.Tokuyama, Jpn. J. Appl. Phys. **16**, 245 (1977).

7) K.Yagi, K.Miyake, and T.Tokuyama, Institute of Physics Conference Series No.38 (1978), p.136.

8) G.D.Alton, J.B.Roberto, C.W.White, and R.A.Zuhr, Nucl. Instrum. Methods **177**, 273 (1980).

9) S.C.Cheng, I.Yamada, and T.Takagi, Proceedings of the Fifth Symposium on Ion Sources and Ion-Assisted Technology, Tokyo (The Research Group of Ion Engineering, Kyoto University, 1981), p.171.

10) T.Miyazawa, S.Misawa, S.Yoshida, and S.Gonda, J. Appl. Phys. **55**, 188 (1984).

11) B.A.Probyn, Brit. J. Appl. Phys. (J. Phys. D), Ser.2, Vol.1, 457 (1968).

12) R.B.Fair, J. Appl. Phys. **42**, 3176 (1971).

13) J.R.Pierce, Theory and Design of Electron Beams, 2nd ed. (van Nostrand, New York, 1954), p.178.

14) K.Miyake, K.Yagi, and T.Tokuyama, Nucl. Instrum. Methods **198**, 535 (1982).

15) H.Tsuji, K.Miyata, T.Taya, J.Ishikawa, and T.Takagi, Proceedings of the Ninth Symposium on Ion Sources and Ion-Assisted Technology, Tokyo (The Research Group of Ion Engineering, Kyoto University, 1985), p.195.

Chapter 5

TRANSPARENT CARBON FILM PREPARED BY MASS-SEPARATED

NEGATIVE-CARBON-ION-BEAM DEPOSITION

5.1 Introduction

Carbon film has been formed by various ion- and plasma-assisted techniques[1-3], such as rf or dc plasma decomposition of a hydrocarbon gas[4-9], sputter deposition[10,11], dual-beam sputter deposition[12,13], ionized hydrocarbon deposition[12,14,15], and ion-beam deposition[16,17]. Carbon film that contains hydrogen atoms in them, i.e., hydrogenated carbon film, is produced mainly by hydrocarbon cracking, and shows "diamond-like" properties such as hardness, high electrical resistivity, optical transparency and chemical inertness[4-9,12,14,15]. The "diamond-like" property in this film may be attributed to the contained hydrogen atoms helping to stabilize the tetrahedral bonds of the carbon atoms. The electrical resistivity and optical transparency have been reported to be deteriorating, but the hardness increased when the hydrogen atom concentration in the film was decreased[14,18]. The carbon film has also been reported to be graphitized by thermal annealing which led to desorption of the hydrogen atoms[15,19-21].

On the other hand, carbon film which is deposited mainly by sputtering a graphite target with argon ions has no hydrogen

atoms. Generally, this film has lower electrical resistivity and less optical transparency than the hydrogenated carbon film[10,11]. In the sputter method, the film includes the sputtering ion species, i.e., argon atoms, and atoms such as oxygen and hydrogen which may be absorbed in the graphite target. A decrease in the electrical resistivity of the film through thermal annealing due to the desorption of these atoms has been observed[10]. In the ion-beam deposition method where both argon and carbon ions extracted from an ion source are incident on a substrate, the deposited carbon film shows "diamond-like" properties[16,17]. Since argon and carbon ions were produced by argon discharge in a graphite chamber, atoms such as argon, oxygen, and hydrogen would also be incorporated in the film. Therefore, a small amount of these atoms may play an important role in the stabilization of tetrahedral bonds of the carbon atoms.

Pure carbon film with a "diamond-like" property should be produced, and the preparation conditions investigated, to ascertain whether the tetrahedral bonds of the carbon atoms are stabilized by themselves, and to clarify the key parameters for the formation of the "diamond-like" carbon film. The mass-separated ion-beam deposition technique is a potential technique, because only pure ion species are deposited and a kinetic energy of incident ions is controllable. It is also possible to investigate the mechanisms of the film formation in the ion- and plasma-assisted techniques. Miyazawa et al. deposited the film by using a mass-separated C^+ ion beam, and showed that the film had the "diamond-like" property[22]. Their deposition energies,

however, were high and were only at the two points of 300 and 600 eV, because yields of an ion beam with an energy below 100 eV were not sufficient for deposition. Thus, the dependency of film property on the ion-beam energy was not fully investigated.

The mass-separated negative-ion-beam deposition system has several advantages as described in the previous chapter. Intense negative ion beams for some important elements, which have currents comparable to or more than those of positive ion sources, are obtained by the NIABNIS. No gas flows into the deposition chamber. The structure of the negative-ion-beam deceleration system is simpler than that of the positive-ion-beam deceleration system. Carbon film was produced by use of the negative-ion-beam deposition system, and several properties of the film deposited by a mass-separated C^- or C_2^- ion beam in the energy range of 25 to 1000 eV were investigated[23,24]. These results are presented here in detail.

5.2 Experimental Details

The carbon film was prepared by C^- or C_2^- ion beam deposition using the mass-separated negative-ion-beam deposition system. The acceleration voltage of the deposited negative ion beam was varied from 10 to 1000 V for a C^- ion beam and from 40 to 400 V for a C_2^- ion beam. The deposited area was about 1 cm^2, the current density of the deposited ion beam was 30 - 100 $\mu A/cm^2$, and the deposition time was 1 - 2 hours. The background pressure in the deposition chamber was around 7×10^{-7} Torr during deposition. Substrates used were n-type silicon wafers with a

(100) plane and the resistivity of the wafers was 8 - 15 $\Omega \cdot cm$. For optical measurements in the visible wavelength, nesa-glasses were also used as substrates. To investigate the dependency of the film property on the substrate temperature, C^- ion beams were deposited at room temperature, 400, and 800 $^{\circ}C$ at the acceleration voltage of 100 V. The film thickness was determined by interferometric means.

Table 5.1 lists the preparation conditions of the carbon film such as the deposited ion species, substrate, acceleration voltage, substrate temperature, and deposited film thickness. In Table 5.1, the film samples are numbered for reference. Optical measurements of transmittance and reflectance were undertaken with a spectrophotometer at a wavelength of 2800 - 8800 $\overset{\circ}{A}$. However, we used only the data obtained between 3500 and 8800 $\overset{\circ}{A}$ due to the optical absorption of the nesa-glass substrate below 3500 $\overset{\circ}{A}$. In the infrared (IR) spectral region, transmission spectra were also measured with an IR spectrometer at a wavelength of 2.5 - 25 μm. The refractive indices were obtained by ellipsometry with a He-Ne laser of 6328 $\overset{\circ}{A}$. The electrical resistivity was measured by depositing aluminum electrodes on both sides of the carbon film and silicon substrate, i.e., Al/(C-film)/(Si-substrate)/Al configuration. The resistivity was determined from the inclination of the V-I characteristics at an applied voltage of 5 V (electrical field of more than 10^5 V/cm). The Rutherford backscattering spectra were used together with the film thickness measurement so that the atomic density was estimated. The crystal structures were observed by the reflection of high-energy electron-diffraction (RHEED) patterns

147

Table 5.1   List of preparation conditions of the

carbon film deposited by the C^- and C_2^- ion beams.

RT means room temperature.

Sample number	Deposited ion species	Substrate	Acceleration voltage (V)	Substrate temperature ($^\circ$C)	Film thickness (Å)
1	C^-	n-Si(100)	10	RT	4500
2	C^-	n-Si(100)	40	RT	4000
3	C^-	n-Si(100)	70	RT	3000
4	C^-	n-Si(100)	100	RT	3500
5	C^-	n-Si(100)	150	RT	3000
6	C^-	n-Si(100)	200	RT	3500
7	C^-	n-Si(100)	400	RT	3000
8	C^-	n-Si(100)	1000	RT	4500
9	C^-	n-Si(100)	100	400	4000
10	C^-	n-Si(100)	100	800	4500
11	C^-	nesa-glass	10	RT	4500
12	C^-	nesa-glass	30	RT	2500
13	C^-	nesa-glass	50	RT	3500
14	C^-	nesa-glass	100	RT	4000
15	C^-	nesa-glass	300	RT	1500
16	C_2^-	n-Si(100)	40	RT	3000
17	C_2^-	n-Si(100)	60	RT	2000
18	C_2^-	n-Si(100)	100	RT	3500
19	C_2^-	n-Si(100)	200	RT	3500
20	C_2^-	n-Si(100)	400	RT	3500
21	C_2^-	nesa-glass	40	RT	1800
22	C_2^-	nesa-glass	100	RT	1500
23	C_2^-	nesa-glass	300	RT	1200

and the scanning electron microscopy (SEM) images.

5.3 Experimental Results

5.3.1 Optical properties

In the photon energy range of 1.4 - 3.5 eV, the measured transmittance and reflectance values were used to estimate the optical absorption coefficient α. Figure 5.1 shows $(\alpha h \nu)^{1/2}$ versus $h\nu$ of the carbon film deposited by the C^- and C_2^- ion beams at the acceleration voltage of 100 V (sample numbers 14 and 22). The optical gap E_{opt} is deduced using a well-known relationship, $(\alpha h \nu)^{1/2} \propto (h\nu - E_{opt})$, which is valid for the amorphous film[25]. Figure 5.2 shows the optical gaps of the carbon film deposited by the C^- and C_2^- ion beams as a function of the acceleration voltage. For the C^- ion beam deposition, an optical gap of about 0.96 eV was observed in the film deposited at the acceleration voltage of 100 V. On the other hand, a film with an optical gap of about 1.44 eV was obtained for the C_2^- ion beam deposition at the same acceleration voltage.

Figure 5.3 shows the IR transmission spectra of the carbon film deposited on n-Si (100) plane at substrate temperatures of room temperature, 400, and 800 $^{\circ}C$ (sample numbers 4, 9, and 10). The acceleration voltage was 100 V. The spectrum of an n-Si substrate is also shown in the figure as a reference. The films deposited at room temperature and 400 $^{\circ}C$ showed no appreciable absorption in the IR spectral region. However, strong absorption like that of a graphite film was observed in the film deposited at 800 $^{\circ}C$. The IR transmission spectra of the film deposited at
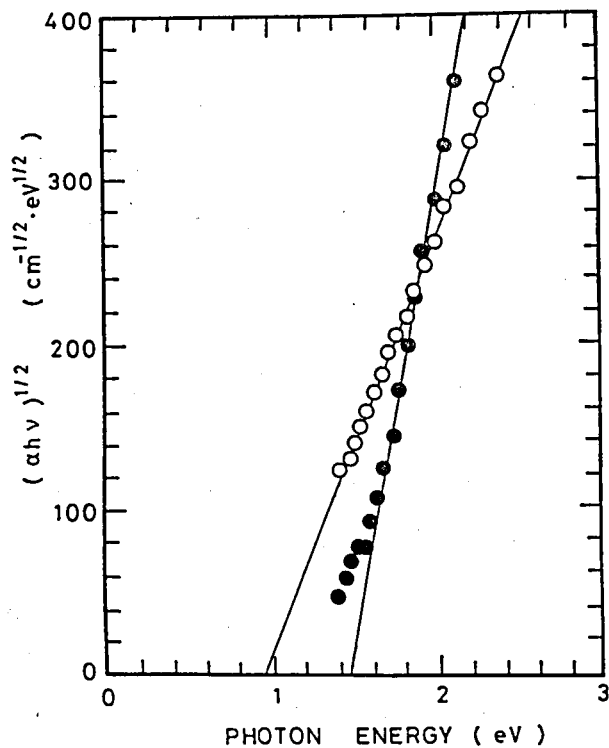
Fig. 5.1   Typical examples of $(\alpha h\nu)^{1/2}$ vs $h\nu$

plots for the carbon film deposited by the C^- (O)

and C_2^- (●) ion beams at the acceleration voltage

of 100 V.
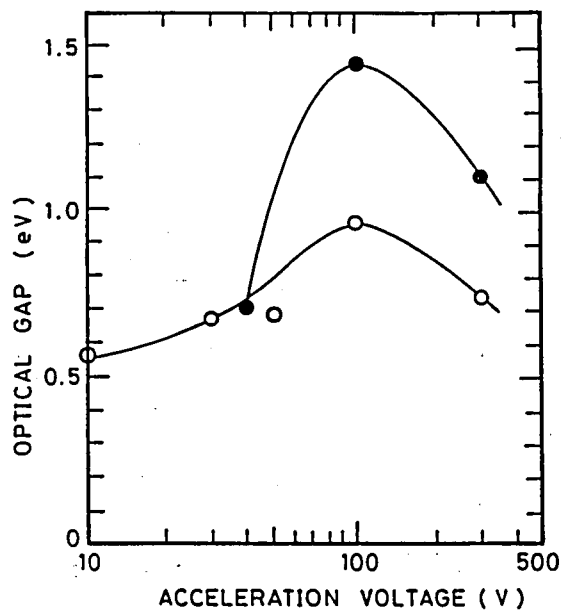
Fig. 5.2　Optical gaps of the carbon film deposited by the C^- (O) and C_2^- (●) ion beams as a function of the acceleration voltage.
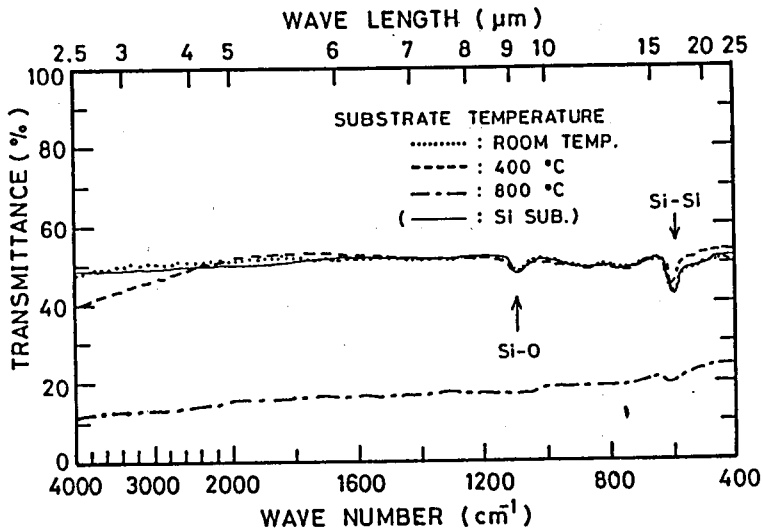
Fig. 5.3 Infrared transmission spectra of the carbon film deposited on n-Si (100) substrate at room temperature, 400, and 800 °C. The acceleration voltage was 100 V.

room temperature showed the same transparency in the range of the acceleration voltage of 10 - 1000 V, and almost no difference was observed between the film deposited by the C^- and C_2^- ion beams. The refractive indices n at the wavelength of 6328 Å were around 3.1, and were insensitive to the acceleration voltage. Since the refractive index of a diamond is 2.4, this value was fairly high.

5.3.2 Electrical properties

Figure 5.4 shows the electrical resistivity of the carbon film as a function of the acceleration voltage in the case of the C^- and C_2^- ion beam deposition at room temperature. The resistivity depends on the acceleration voltage, and shows the maximum value, 1.5×10^8 $\Omega \cdot cm$, at the acceleration voltage of 150 V for the C^- film. On the other hand, the resistivity of the carbon film deposited by the C_2^- ion beam was two orders of magnitude higher than that deposited by the C^- ion beam. Extremely high resistivity of 1.8×10^{10} $\Omega \cdot cm$ was obtained at the acceleration voltage of 100 V. The resistivity has a strong dependence on the substrate temperature, as shown in Fig. 5.5. At the substrate temperature of 800 $^\circ C$, the resistivity was four orders of magnitude lower than that at room temperature.

5.3.3 Crystal structure

Figures 5.6 (a) and (b) show the SEM images of the carbon film deposited by the C^- and C_2^- ion beams, respectively (sample numbers 4 and 19). In both the films deposited by the C^- and C_2^- ion beams, the film surface was flat and smooth, and no pin-holes or peel-offs were observed.

153
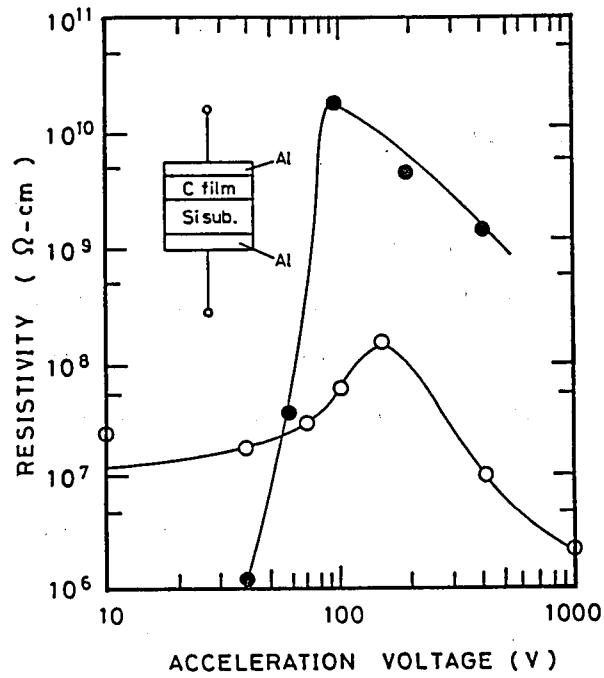
Fig. 5.4   Electrical resistivity of the carbon film
deposited by the C^- (○) and C_2^- (●) ion beams as
a function of the acceleration voltage.
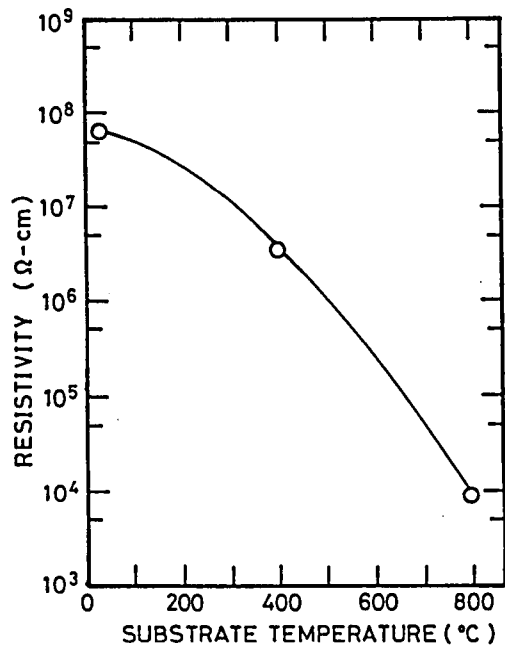
Fig. 5.5 Electrical resistivity of the carbon film deposited by the C^- ion beam as a function of the substrate temperature. The acceleration voltage was 100 V.

2 μm

(a)

2 μm

(b)
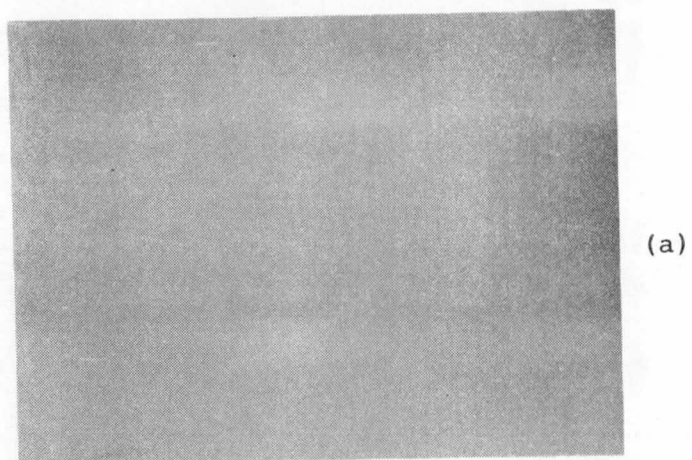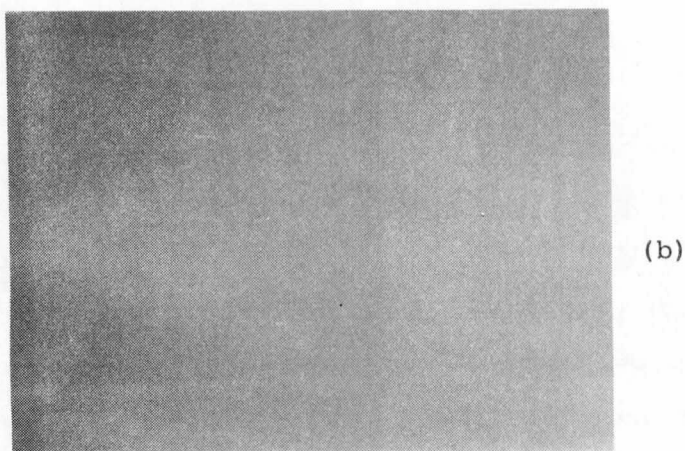
Fig. 5.6   SEM images of the surface of the carbon
film deposited by (a) the C^- and (b) the C_2^- ion
beams.

Figures 5.7 (a) and (b) show the RHEED patterns of the carbon film deposited at room temperature by the C^- and C_2^- ion beams, respectively (sample numbers 4 and 19). The RHEED patterns of both the films deposited by the C^- and C_2^- ion beams indicate that the film structures are amorphous. The patterns were almost the same with variation of the acceleration voltage. Figure 5.7 (c) shows the RHEED pattern of the carbon film deposited at 800 ^{O}C by the C^- ion beam (sample number 10). In this film, weak rings were observed. The lattice constants that are determined from the ring spacings corresponded to the interplaner spacings in a graphite crystal.

5.3.4 Atomic density

In the Rutherford backscattering spectrum, the backscattering yields for a film are proportional to the product of the atomic density of the film and film thickness. Thus, the atomic density of the carbon film was calculated by using the backscattering yields and the film thickness measured by the interferometric means. Figure 5.8 shows the atomic density of the film deposited by the C^- ion beam as a function of the acceleration voltage. The densities of diamond and graphite are also indicated in this figure for reference. The density of the film was higher than that of graphite but lower than that of diamond, and had relatively high values in the range of the acceleration voltage of 100 – 200 V.

5.3.5 Other property

When the carbon film deposited at room temperature was
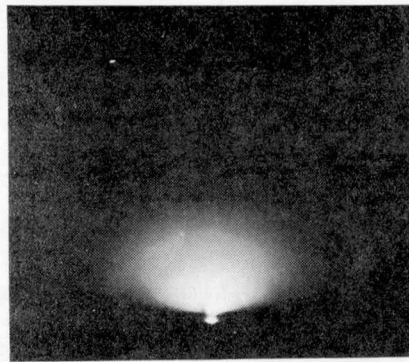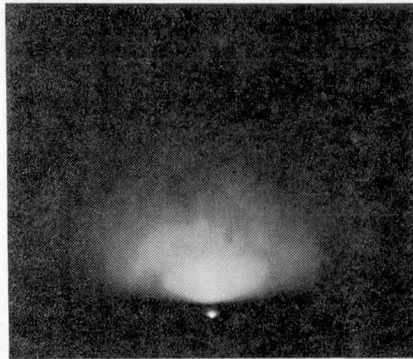
Fig. 5.7   RHEED patterns of the carbon film
deposited by (a) the C^- and (b) the C_2^- ion beams
at room temperature.   (c) RHEED pattern of the
carbon film deposited by the C^- ion beam at 800
$^{\circ}C$.
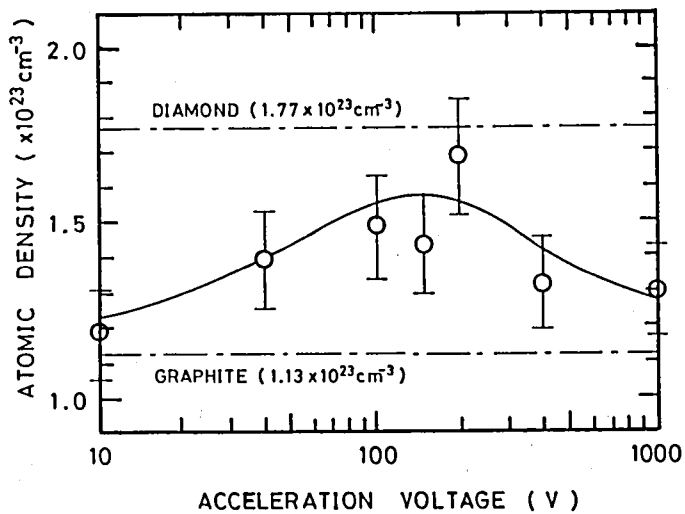
Fig. 5.8   Atomic density of the carbon film

deposited by the C⁻ ion beam as a function of the

acceleration voltage.   The atomic densities of

diamond and graphite are indicated in the figure

for reference.

exposed to CF_4 plasma, a small amount of fluorine atoms was absorbed on the surface of the film. This shows that the carbon film was chemically inert. By micro-Vickers measurement, the carbon film was harder than a Si substrate.

5.4 Discussion

The optical gap, electrical resistivity, and atomic density of the carbon film deposited by the C^- ion beam at room temperature have a similar dependence on the acceleration voltage, as shown in Figs. 5.2, 5.4, and 5.8. In the range of the acceleration voltage of 100 - 200 V, the optical gap, electrical resistivity, and atomic density of the film showed the maximum values. Generation of tetrahedral bonds of carbon atoms with the highest density, i.e., diamond structure, can be assumed to be promoted by depositing the ion beam with the energy corresponding to this acceleration voltage range. The depositing ion beam with the energy of more than 100 eV sputters film and preferentially removes atoms with weaker bonds, leading to a buildup of those atoms having the strongest bonds[17]. Thus, some atoms with weaker bonds such as graphite-like bonds remained in the carbon film deposited at the acceleration voltage less than 100 V. As a result, the atomic density, optical gap, and electrical resistivity indicate lower values. On the other hand, when the energy of the ion beam is higher than 200 V, the deposited film suffers damage from the impinging ion beam. Defects are, then, generated in the film, and the atomic density, optical gap, and electrical resistivity are reduced.

160

The carbon film deposited by the C_2^- ion beam indicated a different property from that deposited by the C^- ion beam. The film deposited by the C_2^- ion beam has a superior property on the optical gap and electrical resistivity. Although the cause of the differences between the films deposited by the C^- and C_2^- ion beams is not yet understood, the charge state and bonding structure of C_2^- ions might have significant influences on the formation of the carbon film. Thermal spikes and high pressure which are caused by the impinging ions promote the crystal growth of the film, and the film, however, is damaged unless its energy localization is fully relaxed[26]. Since a C_2^- ion is larger than a C^- ion, the thermal spikes caused by the impinging C_2^- ions could be wide and shallow. Thus, for the C_2^- deposition their energy localization might be fully relaxed quickly, so that the damages would not be included in the film.

Compared with the carbon film deposited by a mass-separated C^+ ion beam[22], the carbon film deposited by the C^- ion beam has an electrical resistivity higher by one order of magnitude at nearly the same deposition energy of 300 eV. The C^+ deposition film has also been reported to be transparent in the infrared region. However, it is difficult to discuss in detail the differences of the film property between the C^+ ion beam deposition and the C^- or C_2^- ion beam deposition, at present, because the deposition energy range of the C^+ ion beam was too narrow and at only the two points of 300 and 600 eV.

The substrate temperature has a significant influence on the film property. The film deposited at the substrate temperature of 800 $^\circ$C showed a graphite property, i.e., weak graphite-like

rings in the RHEED pattern, low electrical resistivity, and IR absorption, as shown in Figs. 5.7 (c), 5.5, and 5.3, respectively. Carbon film prepared by condensing carbon vapor in a vacuum was progressively graphitized by heat treatment between 25 and 2700 $^{\circ}C^{27)}$. The diamond is in a metastable state of equilibrium at atmospheric pressure and room temperature. Therefore, at the substrate temperature over several hundreds $^{\circ}C$, the thermal energy of the substrate might dominate the carbon film growth rather than the thermal spikes and high pressure driven by the impinging ions.

The carbon film deposited by the C^- or C_2^- ion beam has much higher electrical resistivity and much more optical transparency than that prepared by the sputter method[10,11], but has a little lower electrical resistivity and slightly less optical transparency than that deposited by plasma decomposition of the hydrocarbon gas[5,14,28]. However, the film deposited by plasma decomposition of hydrocarbon gas includes hydrogen atoms, which stabilized the tetrahedral bonds of carbon atoms[19]. Thus, the film property deteriorates when the hydrogen atoms are desorbed[15,19-21]. On the other hand, the carbon film deposited by the C^- or C_2^- ion beam includes no hydrogen atoms and has higher atomic density than the film deposited with hydrogen. The tetrahedral bonds of carbon atoms are considered to be stabilized by only carbon atoms in the carbon film deposited by the C^- or C_2^- ion beam. Judging from the results of the chemical inertness of the surface, the film has a small amount of substitutions such as dangling bonds, defects and the other atoms binding the carbon atoms.

5.5 Summary

A mass-separated negative-ion-beam deposition system was constructed, which decelerates several tens of μA of negative carbon ion beams to a final acceleration voltage of 10 - 1000 V. Since, in this system, the negative ion source, NIABNIS, produces a large amount of negative ions and the negative-ion-beam deceleration system is superior, carbon film of several thousands of Å in thickness is deposited in a few hours. The property of the carbon film deposited by a C^- ion beam depended on the acceleration voltage, i.e., the depositing ion energy. At the acceleration voltage of 100 - 200 V, the optical gap, electrical resistivity, and atomic density showed the maximum values of 0.96 eV, 1.5×10^8 $\Omega \cdot cm$, and 1.7×10^{23} cm^{-3}, respectively. The film deposited at room temperature was amorphous and completely transparent in the IR spectral region. The carbon film showed a graphite-like property when the substrate temperature was raised. At the substrate temperature of 800 $^\circ C$, the film showed graphite-like rings in the RHEED pattern, IR absorption, and a low-electrical resistivity. The carbon film deposited by a C_2^- ion beam had a property different from that deposited by a C^- ion beam. The film deposited by the C_2^- ion beam had a higher electrical resistivity of 1.8×10^{10} $\Omega \cdot cm$ and a higher optical gap of 1.44 eV. The film surface was smooth and no peel-off was observed. Because the carbon film exposed to CF_4 plasma absorbed almost no fluorine atoms, the carbon film was considered to contain only a few dangling bonds, defects, and other atoms binding the carbon atoms.

In this deposition system, one can investigate the film property in a wide range of deposition energies. Therefore, the mechanism of the ion- and plasma-assisted film formation should be investigated, especially from the standpoint of the kinetic energy and ionic charge state of the ions.

References (Chapter 5)

1) T.Takagi, Thin Solid Films **92**, 1 (1982).

2) C.Weissmantel, J. Vac. Sci. Technol. **18**, 179 (1981).

3) L.P.Andersson, Thin Solid Films **86**, 193 (1981).

4) D.S.Whitmell and R.Williamson, Thin Solid Films **35**, 255 (1976).

5) L.Holland and S.M.Ojha, Thin Solid Films **58**, 107 (1979).

6) S.Berg and L.P.Andersson, Thin Solid Films **58**, 117 (1979).

7) B.Meyerson and F.W.Smith, J. Non-Cryst. Solids **35/36**, 435 (1980).

8) K.Enke, Thin Solid Films **80**, 227 (1981).

9) H.Vora and T.J.Moravec, J. Appl. Phys. **52**, 6151 (1981).

10) C.Wyon, R.Gillet, and L.Lombard, Thin Solid Films **122**, 203 (1984).

11) N.Savvides, J. Appl. Phys. **55**, 4232 (1984).

12) C.Weissmantel, G.Reisse, H.J.Erler, F.Henny, K.Bewilogua, U.Ebersbach, and C.Schuerer, Thin Solid Films **63**, 315 (1979).

13) B.A.Banks and S.K.Rutledge, J. Vac. Sci. Technol. **21**, 807 (1982).

14) T.Mori and Y.Namba, J. Vac. Sci. Technol. **A1**, 23 (1983).

15) P.Oelhafen, J.L.Freeouf, J.M.E.Harper, and J.J.Cuomo, Thin Solid Films **120**, 231 (1984).

16) S.Aisenberg and R.Chabot, J. Appl. Phys. **42**, 2953 (1971).

17) E.G.Spencer, P.H.Schmidt, D.C.Joy, and F.J.Sansalone, Appl. Phys. Lett. **29**, 118 (1976).

18) T.J.Moravec and J.C.Lee, J. Vac. Sci. Technol. **20**, 338 (1982).

19) F.W.Smith, J. Appl. Phys. **55**, 764 (1984).

20) M.P.Nadler, T.M.Donovan, and A.K.Green, Thin Solid Films **116**, 241 (1984).

21) R.O.Dillon, J.A.Woollam, and V.Katkanant, Phys. Rev. B **29**, 3482 (1984).

22) T.Miyazawa, S.Misawa, S.Yoshida, and S.Gonda, J. Appl. Phys. **55**, 188 (1984).

23) J.Ishikawa, Y.Takeiri, K.Ogawa, and T.Takagi, J. Appl. Phys. **61**, 2509 (1987).

24) J.Ishikawa, K.Ogawa, Y.Takeiri, and T.Takagi, Proceedings of the Ninth Symposium on Ion Sources and Ion-Assisted Technology, Tokyo, (The Research Group of Ion Engineering, Kyoto University, 1985), p.255.

25) G.A.N.Connel, Amorphous Semiconductors, Topics Appl. Phys. **36**, 73 (1979).

26) C.Weissmantel, K.Bewilogua, D.Dietrich, H.J.Erler, H.J.Hinneberg, S.Klose, W.Nowick, and G.Reisse, Thin Solid Films **72**, 19 (1980).

27) J.N.Rouzaud, A.Oberlin, and C.B.Bassez, Thin Solid Films **105**, 75 (1983).

28) J.Zelez, RCA Rev. **43**, 665 (1982).

Chapter 6

CONCLUSIONS

The motivation of this research is to apply negative ion beams to material science and to develop a new technique for film formation using negative ion beams. In this thesis, an intense heavy negative-ion source was developed for the purpose of obtaining negative ion beams in sufficient amounts to be applied to material science, and, then, thin film was formed by mass-separated negative-ion-beam deposition and its properties were investigated.

In chapter 2, the construction and the operational characteristics of the axial magnetic field extraction-type microwave ion source with a permanent magnet were described. This microwave ion source was developed as a primary plasma ion source of the intense heavy negative-ion source. The axial magnetic field through an ion extraction electrode, which is a part of a closed magnetic circuit formed by the combination of the permanent magnet and ferromagnetic materials, is found to be extremely effective both to high-density plasma production by the ECR process and to high-efficient ion extraction by transporting the generated ions along the magnetic force lines. The continuous ion beams of 2-3 mA for various gases (Ar, N_2, CO_2), metal vapors (Cs, Rb) and reactive gas (O_2) were delivered from the extraction aperture of 2 mm in diameter. An ion beam with

low emittance (10^{-8} m·rad) and high brightness (10^{11} A·m^{-2}·rad^{-2}) was obtained. Lifetime of this ion source was extremely long even for oxygen gas. It is concluded that this high-current microwave ion source with compact structure and low power consumption can be utilized for wide range of applications such as accelerators, sputtering, etching and ion beam deposition.

In chapter 3, the construction and the operational characteristics of the neutral- and ionized-alkaline-metal bombardment-type heavy negative-ion source, NIABNIS, were described. The NIABNIS is a high current and compact sputter negative-ion source where both neutral- and ionized-alkaline-metal particles are simultaneously bombarded on a sputter cone with the temperature of the sputtering target being controllable. To supply a sufficient amount of neutral- and ionized-cesium particles onto the sputtering target surface, the axial magnetic field extraction-type microwave ion source is used for the primary alkaline ion source, and the distance between the extraction aperture of the alkaline ion beam and the sputtering target is minimized. The mechanism of negative ion beam production and the optimum condition of target surface were discussed. Efficient negative ion production is found to be ascribed to the formation of the cesium half- to mono-layer on the target surface, which results in a minimum surface work function. In the NIABNIS, the target surface condition is easily optimized for various elements by both the neutral-cesium-particle supply and the target temperature control. It is also found that the negative ion current is proportional to the incident cesium ion current if the cesium coverage is maintained

in an appropriate condition. 0.74 mA of C^- ion current, 320 μA of Cu^- ion current and 170 μA of Si^- ion current were obtained, which were enough to apply the negative ion beam to material science. As a result, the film formation by the negative-ion-beam deposition became practical.

In chapter 4, the mass-separated negative-ion-beam deposition system was described. The deposition system consists of the NIABNIS and the negative-ion-beam deceleration electrode system. In the deceleration electrode system, a convergent lens is placed close to the deceleration electrode system to cancel the divergent lens effect due to the deceleration gap, and an auxiliary electrode with an angle of 67.5° from the normal is placed on the substrate to compensate the beam divergence due to the space-charge repulsion force. The structure of the negative-ion-beam deceleration system is simpler than any of the positive-ion-beam deceleration systems because production of oppositely charged particles, i.e., positive ions, that might be accelerated in the deceleration field, can be neglected. Moreover, no gas flows into the deposition chamber in operation since the NIABNIS is a sputter ion source. A several tens of μA of C^- ion beam was successfully decelerated to 10-100 eV and a carbon film with several thousand Å in thickness was obtained in a few hours even at a final energy of about 24 eV.

In chapter 5, the property of carbon film deposited by the C^- and C_2^- ion beams was investigated. In the C^- deposition film, the optical gap, electrical resistivity and atomic density showed the maximum values of 0.96 eV, 1.5×10^8 $\Omega \cdot$cm and 1.7×10^{23} cm^{-3}, respectively, at the depositing ion energy of 115 to 215

eV. The film deposited at room temperature was amorphous and completely transparent in the IR spectral region. When the substrate temperature was raised, the carbon film showed a graphite-like property. The film deposited by the C_2^- ion beam had a higher electrical resistivity of 1.8×10^{10} $\Omega \cdot cm$ and a higher optical gap of 1.44 eV. The film surface was smooth and no peel-off was observed in every case. The transparent carbon film was successfully obtained by the mass-separated negative-carbon-ion-beam deposition. It is also found that the depositing ion state, i.e., atom or molecule, has a great influence on the interaction between solid surface and depositing low-energy ion beam.

In this research, the ion source development led to the creation of new application fields for the negative ion beam. The microwave ion source, the intense negative-ion source, NIABNIS, and the negative-ion-beam deposition system were newly developed and, as a result, the negative ion beam was successfully applied to film formation. In conclusion, the technique of mass-separated negative-ion-beam deposition is unique with high potential for film formation and is useful for the investigation of the interaction between solid surfaces and the ion beam.

APPENDIX A

The calculation method and the assumptions made in the calculation procedure of the magnetic force lines are summarized as follows:

(a) Giving a magnetic potential of an arbitrary equal value with an opposite sign to each other to ferromagnetic materials on each side of magnetic poles of a permanent magnet, assuming that the magnetic resistance of the ferromagnetic materials is negligible.

(b) By solving a Laplace equation of magnetostatic field using the magnetic potential given to the ferromagnetic materials, obtaining the magnetic field. Thus, notice that the obtained magnetic field intensity is a relative value.

(c) Determining the start points of the magnetic force lines from the surface density of magnetic charge which is proportional to the magnetic field intensity on the surface of the ferromagnetic materials.

(d) Tracing the magnetic force line by continuing a step by a short unit length to the same direction as the magnetic field at the start point of the step.

The magnetic potential of the permanent magnet is appropriately given. The flow chart of the program is shown in Fig. A.1. The program is valid only for an axisymmetric configuration.

```
        ┌─────────────────┐
        │ Type and array  │
        │   declaration   │
        └────────┬────────┘
                 ▼
         ┌───────────────┐
         │ Input/output  │
         │   of data     │
         └───────┬───────┘
                 ▼
      ┌────────────────────┐
      │ Input of arrangement│
      │   of ferromagnetic │
      │  or nonferromagnetic│
      │     materials and  │
      │    set of initial  │
      │        condition   │
      └──────────┬─────────┘
                 ▼
        ┌─────────────────┐
        │ Solving Laplace │
        │    equation     │
        └────────┬────────┘
                 ▼
      ┌───────────────────┐
      │     Output of     │
      │ magnetic potential│
      └─────────┬─────────┘
                ▼
        ┌─────────────────┐
        │ Calculation of  │
        │ magnetic field  │
        └────────┬────────┘
                 ▼
       ┌──────────────────┐
       │ Tracing magnetic │
       │   force lines    │
       └────────┬─────────┘
                ▼
        ┌─────────────────┐
        │   Output of     │
        │  the results    │
        └────────┬────────┘
                 ▼
        ┌─────────────────┐
        │     End of      │
        │  calculation    │
        └─────────────────┘
```
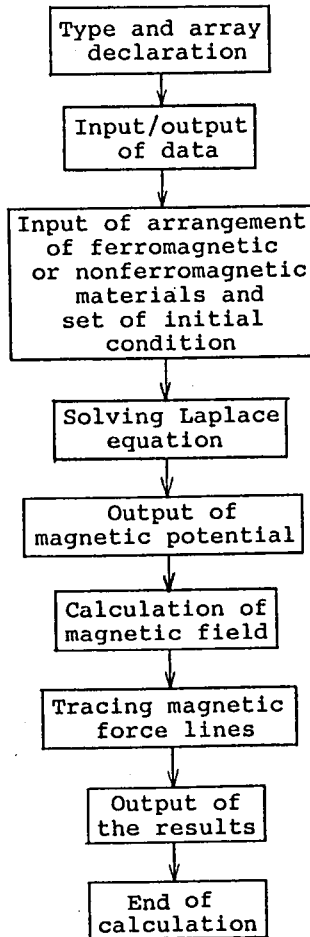
Fig. A.1   Flow chart of the calculation program of

the magnetic force lines.

APPENDIX B

The basic concept of the simulation code of the charged-particle beam trajectories is that the equations dominating the stationary ion beam are iteratively solved under the condition of the space-charge limited flow. The charged-particle beam trajectories are, in general, expressed by Poisson's equation, equation of motion and equation of continuity. The computational method is outlined as follows:

(a) Initially, solving Laplace equation under a given condition without considering the space charge, and obtaining the electric potential and, then, the electric field.

(b) Computing the beam trajectory by integrating the equation of motion.

(c) Estimating the space charge from the beam trajectory and the continuity of current.

(d) Substituting the estimated space charge to Poisson's equation and then solving the equation of motion and the equation of continuity again.

(e) Iterating this procedure until the beam trajectory converges.

In the case of the simulation of extracted ion beam trajectories in a plasma ion source, ion extraction surface, i.e., plasma boundary, is decided by the ion extraction voltage, the plasma parameters (plasma density and plasma electron temperature), the electrode potential, and the electrode configuration and arrangement. The ion-extraction-surface position is determined at such a position as self-consistently
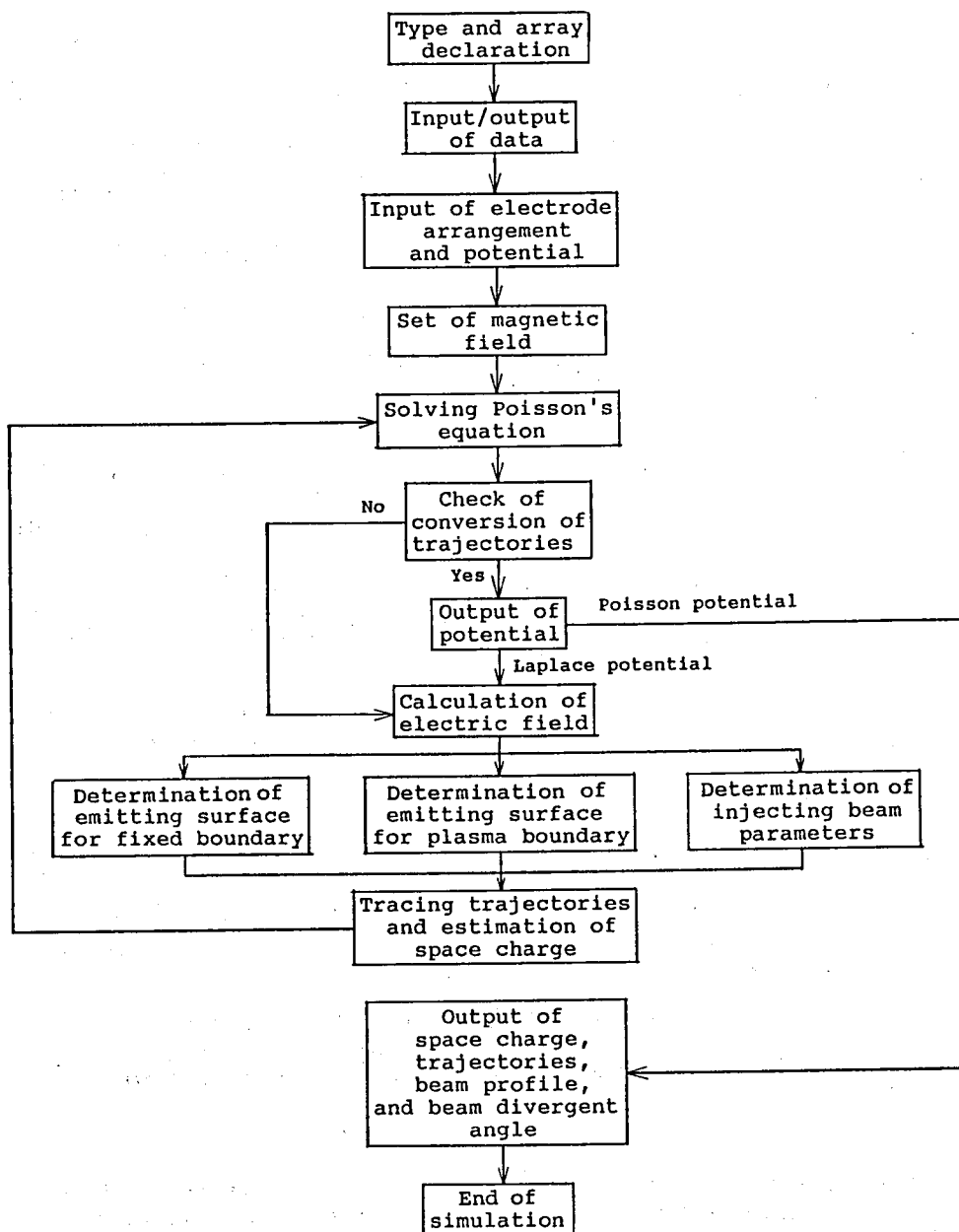
Fig. B.1 Flow chart of the simulation program of the charged-particle beam trajectories.

174

satisfies the condition of the space-charge-limited-current flow decided from the potential difference between a source plasma and an ion extraction electrode. Ions are assumed to be extracted from a fictive extraction surface, which is located away from the actual extraction surface at such a distance as the space-charge limited current between these two surfaces is equal to the saturation ion current of the source plasma. In the simulation code of the ion-extraction-surface determination, it is assumed that the extracted ion current density from the fictive extraction surface is uniform everywhere, i.e., the plasma density of the plasma boundary is uniform on every surface position of the boundary, and that thermal motion of ions is ignored and the plasma boundary is equipotential surface. Thus, the ions are assumed to be extracted in the normal from the plasma boundary.

In the case of the simulation of the ion or electron trajectories extracted from a fixed boundary, the current density at the boundary surface is determined from the space-charge-limited current. As a matter of course, a current density less than the space-charge-limited current density is able to be given arbitrarily. In this simulation code, beam trajectories in a lens system can be also simulated by injecting the beam diverging out of or converging into an arbitrary fictive point into a given electrode arrangement.

The flow chart of the program is shown in Fig. B.1. The program is valid only for an axisymmetric configuration.

LIST OF PUBLICATIONS

(a) Papers

[1] Junzo Ishikawa, <u>Yasuhiko Takeiri</u>, and Toshinori Takagi, "Axial magnetic field extraction-type microwave ion source with a permanent magnet", Review of Scientific Instruments Vol.55, No.4, April 1984, pp.449-456.

[2] Junzo Ishikawa, <u>Yasuhiko Takeiri</u>, and Toshinori Takagi, "Mass-separated negative-ion-beam deposition system", Review of Scientific Instruments Vol.57, No.8, August 1986 (part 1), pp.1512-1518.

[3] Junzo Ishikawa, <u>Yasuhiko Takeiri</u>, Kiyoshi Ogawa, and Toshinori Takagi, "Transparent carbon film prepared by mass-separated negative-carbon-ion-beam deposition", Journal of Applied Physics Vol.61, No.7, April 1987, pp.2509-2515.

(b) Proceedings

[1] Junzo Ishikawa, <u>Yasuhiko Takeiri</u>, and Toshinori Takagi,
"Compact microwave discharge ion source by use of permanent
magnet", Proceedings of the Sixth Symposium on Ion Sources and
Ion-Assisted Technology, Tokyo, June 7-9, 1982, (The Research
Group of Ion Engineering, Kyoto University, 1982), pp.25-28.

[2] Junzo Ishikawa, <u>Yasuhiko Takeiri</u>, and Toshinori Takagi,
"Axial magnetic field extraction type microwave ion source",
Proceedings of the International Ion Engineering Congress -
ISIAT'83 & IPAT'83 -, Kyoto, September 12-16, 1983, (The
Institute of Electrical Engineers of Japan, Tokyo, 1983),
pp.379-384.

[3] Junzo Ishikawa, <u>Yasuhiko Takeiri</u>, Hiroshi Tsuji, and
Toshinori Takagi, "High current heavy negative ion source with
microwave-discharged particle bombardment", Proceedings of the
International Ion Engineering Congress - ISIAT'83 & IPAT'83 -,
Kyoto, September 12-16, 1983, (The Institute of Electrical
Engineers of Japan, Tokyo, 1983), pp.131-136.

[4] <u>Yasuhiko Takeiri</u>, Junzo Ishikawa, and Toshinori Takagi,
"Neutral and ionized alkaline metal bombardment type heavy
negative ion source", Proceedings of the Eighth Symposium on
Ion Sources and Ion-Assisted Technology, Tokyo, June 4-6,
1984, (The Research Group of Ion Engineering, Kyoto

University, 1984), pp.31-36.

[5] <u>Yasuhiko Takeiri</u>, Kiyoshi Ogawa, Junzo Ishikawa, and

Toshinori Takagi, "Negative-ion-beam deposition system",

Proceedings of the Ninth Symposium on Ion Sources and Ion-

Assisted Technology, Tokyo, June 3-5, 1985, (The Research

Group of Ion Engineering, Kyoto University, 1985), pp.211-216.

[6] Junzo Ishikawa, Kiyoshi Ogawa, <u>Yasuhiko Takeiri</u>, and

Toshinori Takagi, "Preparation of transparent carbon films by

negative-carbon-ion-beam deposition", Proceedings of the

Ninth Symposium on Ion Sources and Ion-Assisted Technology,

Tokyo, June 3-5, 1985, (The Research Group of Ion Engineering,

Kyoto University, 1985), pp.255-260.

LIST OF TECHNICAL REPORTS

[1] Hiroshi Tsuji, <u>Yasuhiko Takeiri</u>, Junzo Ishikawa, and Toshinori Takagi, "Energy distribution of negative ions produced by cesium bombardment", The Spring Meeting of JSAP, Tokyo, April 1-4 1982, Paper No. 2p-A-9, p.347.

[2] <u>Yasuhiko Takeiri</u>, Junzo Ishikawa, and Toshinori Takagi, "Compact microwave ion source by use of permanent magnet", The Fall Meeting of JSAP, Fukuoka, September 28-30 1982, Paper No. 28p-M-16, p.244.

[3] Junzo Ishikawa, <u>Yasuhiko Takeiri</u>, and Toshinori Takagi, "Characteristics of ion beams extracted from compact microwave ion source by use of permanent magnet", 1982 Joint Convention of Institute Associating with Electrical Engineers in Western Region, Kyoto, December 4-5 1982, Paper No. G9-11, p.G271.

[4] <u>Yasuhiko Takeiri</u>, Junzo Ishikawa, and Toshinori Takagi, "Axial magnetic field extraction type microwave ion source with a permanent magnet", The Spring Meeting of JSAP, Chiba, April 4-7 1983, Paper No. 4p-U-17, p.272.

[5] <u>Yasuhiko Takeiri</u>, Junzo Ishikawa, and Toshinori Takagi, "High-current heavy negative-ion source with extraction of 132 μA-C$^-$ ion beam", The Fall Meeting of JSAP, Sendai, September 25-28 1983, Paper No. 26a-T-3, p.228.

[6] <u>Yasuhiko Takeiri</u>, Takahiro Hayashi, Junzo Ishikawa, and Toshinori Takagi, "High-current heavy negative-ion source (II) -- extraction characteristics of negative ion beams", The Spring Meeting of JSAP, Kawasaki, March 29-April 2 1984, Paper No. 29a-W-2, p.253.

[7] <u>Yasuhiko Takeiri</u>, Junzo Ishikawa, and Toshinori Takagi, "High-current heavy negative-ion source (III) -- effect of neutral cesium bombardment", The Fall Meeting of JSAP, Okayama, October 12-15 1984, Paper No. 12a-U-6, p.267.

[8] <u>Yasuhiko Takeiri</u>, Junzo Ishikawa, and Toshinori Takagi, "High-current heavy negative-ion source (IV) -- extraction of high-current negative ion beams", The Fall Meeting of JSAP, Okayama, October 12-15 1984, Paper No. 12a-U-7, p.267.

[9] <u>Yasuhiko Takeiri</u>, Kiyoshi Ogawa, Junzo Ishikawa, and Toshinori Takagi, "High-current heavy negative-ion source (V) -- negative ion production of refractory metal", The Spring Meeting of JSAP, Tokyo, March 29-April 1 1985, Paper No. 1a-H-3, p.320.

[10] <u>Yasuhiko Takeiri</u>, Kiyoshi Ogawa, Junzo Ishikawa, and Toshinori Takagi, "Negative-ion-beam deposition system", The Spring Meeting of JSAP, Tokyo, March 29-April 1 1985, Paper No. 31p-H-5, p.315.

*JSAP (The Japan Society of Applied Physics)